

UNIVERSITÀ DEGLI STUDI DI PADOVA

DIPARTIMENTO DI FISICA E ASTRONOMIA *Galileo Galilei*

CORSO DI LAUREA MAGISTRALE IN FISICA



TESI DI LAUREA MAGISTRALE

**Investigation of shape coexistence
in ^{60}Zn by using the
 γ -ray spectrometer GALILEO
at the Legnaro National Laboratories**

RELATORE:

DOTT. DANIELE MENGONI

LAUREANDA:

GIORGIA PASQUALATO

ANNO ACCADEMICO 2016/2017

To my Family

Index

<i>Abstract</i>	i
Introduction	1
1 Shell and shapes in nuclei	3
1.1 Nuclear models	4
1.1.1 The Bohr-Mottelson Hamiltonian and the collective behavior of nuclei	5
1.1.2 Shell model	7
1.1.3 Mean field	10
1.2 Shapes in nuclei: deformation and shape coexistence	11
1.2.1 The region of N=Z nuclei above ^{56}Ni	14
1.2.2 The case of ^{60}Zn	15
2 The experimental setup at LNL	17
2.1 The nucleus ^{60}Zn and the reaction to populate its excited states	17
2.1.1 Fusion-evaporation reactions	18
2.1.2 The acceleration system: Tandem XTU	19
2.2 γ -ray detection devices	20
2.2.1 The GALILEO γ -ray spectrometer	22
2.3 Ancillary detectors	23
2.3.1 The charged-particle detector EUCLIDES	24
2.3.2 The Neutron Wall detector	26
3 Pre-sorting of the experimental data	29
3.1 Energy calibration	29
3.2 Efficiency calibration	31
3.3 Average and kinematic Doppler correction	32
3.4 Time alignment	35
3.5 Particle selections	37
3.5.1 Neutron- γ discrimination with the Neutron Wall	37
3.5.2 Light-charged particle discrimination in EUCLIDES	37
3.6 The EUCLIDES absorber	40
4 Analysis of the experimental data	43
4.1 γ -ray energy spectra and matrix	45
4.1.1 1α , $1p$ and $1n$ gates	45
4.1.2 γ - γ coincidence matrix	46
4.2 Search for new transitions in ^{60}Zn	49
4.2.1 Background subtraction	51

4.3	Neighboring nuclei of interest	55
4.3.1	The nucleus ^{61}Zn	55
4.3.2	The nucleus ^{60}Cu	55
5	Theoretical calculations and interpretation	59
5.1	The nucleus ^{60}Zn	59
5.1.1	Shell model calculations	59
5.1.2	Beyond mean-field calculations: Energy Density Functional results	63
5.1.3	Comparison with the present experimental data	65
5.2	^{61}Zn : particle-core coupled states	65
6	Conclusions and Outlook.	69
	Appendices	71
A	γ-ray interaction with matter	73
B	Shell-model calculation results	76
B.1	^{60}Zn	76
B.1.1	fp model space	76
B.2	^{61}Zn	79
B.2.1	fp model space	79
B.2.2	fpg model space	79
	Bibliography.	81

Abstract

This thesis describes the results of a fusion-evaporation experiment performed at the Legnaro National Laboratories, using the γ -ray spectrometer GALILEO, that was recently installed at the laboratory, combined with the ancillary detectors EUCLIDES and Neutron Wall, for the light-charged particle and neutron detection, respectively.

The experiment aims at the measurement of non-yrast states in the neutron-deficient, $N=Z$, ^{60}Zn nucleus. The nucleus is located at the lower corner in the region of transitional nuclei, that goes from the spherical ^{56}Ni to the prolate ^{80}Zr . The change in the nuclear shape is a consequence of the shell evolution, that is driven by the nuclear residual interaction between protons and neutrons.

γ -ray spectroscopy is a great experimental tool to investigate the structure of such nuclei that provides essential information to model the nuclear force. By comparing the experimental results with the predictions of the theoretical models, the shape of a nucleus can be derived.

From the analysis of our data set, we confirm the existence of the ground state band in ^{60}Zn , up to the 8^+ state. Large scale shell model (LSSM) and energy density functional (EDF) calculations, are carried out for ^{60}Zn , and are in agreement with the experimental results for the ground state band. Furthermore, we observe a weak transition in a α -gated $\gamma\gamma$ matrix, that could correspond to the decay of a 2_2^+ state, predicted by LSSM calculation at 3.2 MeV, to the 2_1^+ state. However, this state is predicted at a lower energy by the EDF calculations.

Eventually, because of the low statistics and the discrepant theoretical predictions, no firm conclusion can be drawn about the intrinsic shape of the ^{60}Zn nucleus, at this level.

In questa tesi vengono descritti ed interpretati i risultati di uno dei primi esperimenti con lo spettrometro γ GALILEO, installato di recente ai Laboratori Nazionali di Legnaro in Italia.

L'esperimento ha come obiettivo la misura dei primi livelli eccitati non yrast del nucleo $N=Z$ ^{60}Zn , nel contesto di un più generale studio dell'evoluzione della forma dei nuclei nella regione compresa tra il nucleo di forma sferica ^{56}Ni e il nucleo prolato ^{80}Zr . Infatti, in questa regione della carta dei nuclidi, è noto che i nuclei cambiano rapidamente le loro proprietà collettive, come la forma, al variare del numero di nucleoni. Questo effetto è una conseguenza del contributo delle interazioni residue tra nucleoni,

che per nuclei con un ugual numero di protoni e neutroni, diventa più significativo. La struttura di tali nuclei può essere studiata tramite esperimenti di spettroscopia γ , grazie ai quali otteniamo importanti informazioni sulla forza nucleare e sulle correlazioni tra protoni e neutroni nel nucleo. Confrontando i risultati sperimentali con le previsioni dei modelli teorici, è possibile dedurre la forma di un nucleo.

Dall'analisi dei dati sperimentali, la presenza della banda fondamentale fino allo stato 8^+ è stata confermata. Calcoli di shell model (LSSM) e calcoli con il funzionale densità di energia (EDF), effettuati per lo ^{60}Zn , sono in accordo con i dati relativi alla banda fondamentale. Inoltre, una possibile transizione dallo stato 2_2^+ , previsto dai calcoli LSSM a 3.2 MeV, allo stato 2_1^+ , è stata osservata nella matrice $\gamma\text{-}\gamma$ in coincidenza con una particella α . Tuttavia, lo stato 2_2^+ è previsto ad un'energia più bassa dai calcoli di EDF.

In conclusione, non è stato possibile determinare con certezza la forma del nucleo, sia per la limitata statistica che per le discrepanti predizioni dei calcoli teorici.

Introduction

Understanding the properties of the atomic nucleus and try to link them in a unique pattern, is the primary intent of nuclear physics. Large efforts have been deployed since the last century to develop a universal theory that could explains and predicts all the nuclear properties. In parallel, experiments have been conceived to demonstrate or to reject the existing theoretical predictions.

It is not straightforward to describe the interactions between the nucleons arranged in a nuclear system. This because a nucleon is not a fundamental particle but it is composed by three sub-particles, the quarks. QCD explains that quarks have a color charge and interact among each others through the strong interaction. When the quarks are combined inside a nucleon, the color charge is neutralized, thus the interaction between nucleons become a sort of Van der Waals force, difficult to formalize from a mathematical point of view. In low-energy nuclear physics, the existence of quarks can be ignored thanks to the energy scale involved in the nuclear processes. Indeed, low-energy QCD regulates the physics of systems of light quarks at energy and momentum scales smaller than the 1 GeV mass gap observed in the hadron spectrum. The long- and medium-distance regions are dominated by the π exchange. The basic idea is to construct the NN potential in the two regions by explicit calculation of π exchange processes, whereas the detailed behavior of the interaction in the short distance region remains unresolved at the low-energy scales.

A nucleus is identified by the number of its constituents, protons and neutrons, and by the sum of these, that is the mass number. Nuclei can be either stable or radioactive. Stable nuclei observed in nature are about 300, while unstable nuclei are over 7000 [1]. This latter number grows year by year, thanks to the development of new accelerator and detection techniques which permit to observe nuclei with an increasingly shorter mean-life time.

In the last decades many exciting phenomena have been observed in medium-mass nuclei, $A > 56$, with an equal number of protons and neutrons ($N = Z$). In this region of mass the intrinsic shape of nuclei changes rapidly with the number of nucleons leading also to obtain different shapes at comparable excitation energies. This phenomenon is known as *shape coexistence* and it was firstly established in the Pb region, and later around other shell closures, as reviewed recently [2].

For $N = Z$ nuclei, the effects of residual interaction between valence nucleons, which could be correlated with the nuclear shape, are amplified since protons and neutrons occupy the same orbital and the nuclear $T=0$ pairing can also play a role.

Studies of the nuclear shape and its evolution across the nuclide chart are a fundamental test of the nuclear models, especially in regions where different theoretical

approaches, i.e. ab-initio, shell model and mean field techniques, can be used to calculate the same experimental observables.

The shape of a nucleus is not a direct observable but it can be derived by a variety of observables or a combination of them, obtained from different techniques, such as, for example, safe Coulomb excitation and lifetime measurements. Among the intriguing measurements that can establish the shape(s) of a nucleus, the investigation for the existence of structures build upon excited 0^+ states plays a crucial role, being a direct manifestation of a quanto-mechanical behavior of the nucleus.

The neutron deficient N=Z nucleus, ^{60}Zn , lies just beyond the doubly-closed ^{56}Ni , in a region where the shape coexistence, together with increasing deformation, is predicted.

This work reports an experimental investigation of the excited states in ^{60}Zn , by using high-resolution γ -ray spectroscopy techniques, with the goal of probing the existence of a low-lying non-yrast band, that can be a sign of a different-shape structure, and finally of a shape coexistence.

An experiment at the National Laboratory of Legnaro (LNL), Italy, was performed, using a heavy-ion fusion-evaporation reaction to populate excited states of the unstable ^{60}Zn isotope. The de-excitation γ rays were detected by the Compton-suppressed γ -ray array, GALILEO, recently installed at LNL.

The present thesis work can be summarized as follow:

In Chapter 1, an introduction on the basic notions of the nuclear models is given. The experimental setup is described in Chapter 2. The preliminary sorting of data is explained in Chapter 3. In Chapter 4, the data analysis and the sort of data in matrices and various spectra is reported. In the final Chapter 5, large-scale shell model and beyond mean-field calculations for the nucleus of interest are presented. Chapter 6 summarizes the work, draws the conclusions and addresses some future plans to continue along the same research line.

Chapter 1

Shell and shapes in nuclei

Existing nuclei are plotted in a two-dimensional graph where one axis represents the number of neutrons N and the other represents the number of protons Z, as shown in Figure 1.1. In this so called chart of nuclides each point represents a particular isotope. The region of the chart that contains the stable isotopes is known as stability valley. From nuclide chart we notice that, for example, the last stable atomic nucleus with an equal number of protons and neutrons is ^{40}Ca , i.e. $Z=N=20$. In fact, the stability valley follows the $Z=N$ line only for lighter nuclei. Nuclei of larger atomic number require a larger amount of neutrons to guarantee stability, as a consequence of the increasing importance of the Coulomb repulsion of protons.

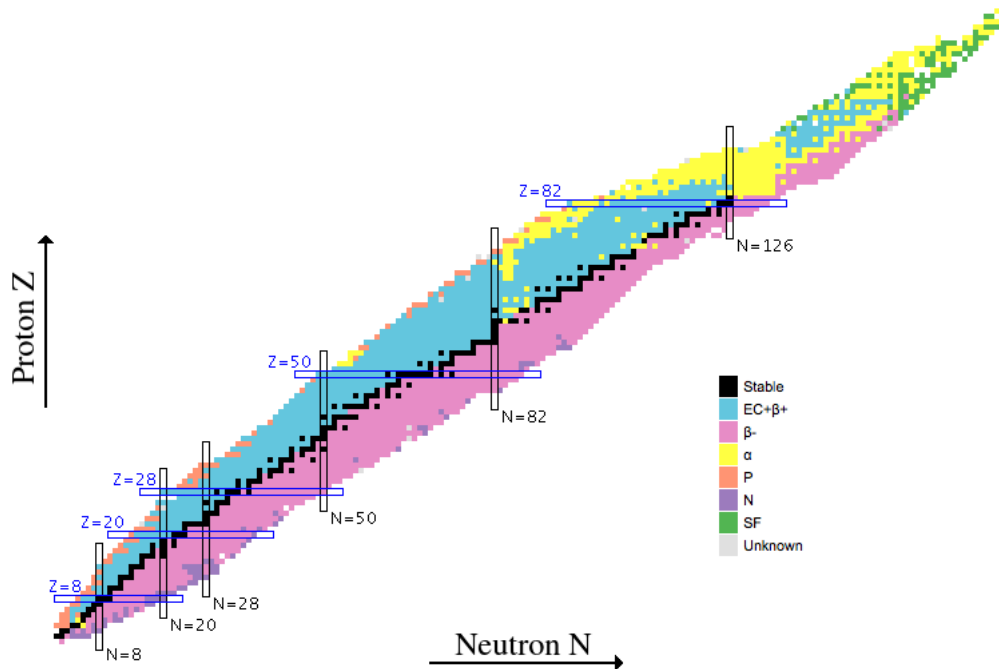


Figure 1.1: Chart of nuclides. The area marked with different colors corresponds to the different radioactive decay modes (β^+ , β^- , α decay, fission).

Nuclei in the stability valley preserve their nature over time because their half life is comparable to, or larger than, the Earth's age. Unstable nuclei have a shorter half

life and turn into stable isotopes by β decay or electron capture, α decay or fission (for heavier nuclei). In the chart of nuclides the radioactive isotopes are placed on both sides of the stability valley. Different colors correspond to different decay modes, as shown in Figure 1.1.

Another nuclear decay is the γ decay. It does not modify the nature of an isotope since it consists in the emission of electromagnetic radiations. Each nucleus can exist in an excited state where, in few ps, it loses the excess of energy by the emission of γ rays until it reaches the ground state.

The low-lying excited states of a nucleus are discrete in energy and their properties are governed by the rules of quantum mechanics. The locations of the excited states differ for each nucleus and the excitation energy depends on the internal structure of the system. Each excited state is characterized by a set of quantum numbers, such as spin, angular momentum, parity and isospin.

The ground state properties of a nucleus, as well as its spectroscopic features, as transition energies, decay lifetimes, etc..., are not easily predictable.

In the present Chapter we present different theoretical approaches that have been applied to describe a nuclear physics system and its properties.

1.1 Nuclear models

A nuclear model is a mathematical construction that grasps the main physical ingredients of a certain system and aims at a description of the nuclear behavior, in a way as universal as possible. It allows to predict and interpret many features of the nuclei such as the binding energy, the lifetimes and the excited levels. By using γ -ray spectroscopy methods, the prediction of the models, like for example the γ -ray transition energies, can be directly compared with the experimental results.

The nucleus is a unique ensemble of strongly interacting fermions (nucleons) that can manifest either a single-particle or a collective behavior, and both degrees of freedom have to be accounted for by the theoretical models.

The theoretical study of the atomic nuclei is based on the solution of the Hamiltonian

$$H = V + T,$$

sum of the kinetic energy T and the potential V of all fermions in a nucleus:

$$H = \sum_{i=1}^A \frac{p_i^2}{2m_i} + \sum_{i>k=1}^A V_{i,k}(r_i, r_k) + \text{higher order many-body interactions}. \quad (1.1.1)$$

Fundamental approaches, like ab-initio methods, aim to exactly solve the Schrödinger equation treating the nucleus as A -interacting fermions. These approaches start from a realistic nuclear interaction, derived from the nucleon-nucleon scattering, and use sophisticated many-body theories to solve the nuclear Hamiltonian. However, calculations are often practically intractable with the exception of very light nuclei, up to mass $A=10$, due to the increasing number of interacting nucleons and therefore the computational cost.

On the other side, the liquid drop model is a macroscopic classical model that treats the nucleus as a drop of incompressible nuclear fluid and introduces the concept of geometrical shape. It predicts the evolution of binding energy and other features in function of global properties of nucleus but fail to predict typical independent-particle phenomena (such as the shell closures effects, see Section 1.1.2). The Bohr and Mottelson model, described in the original papers dating to early 50's and deserving the Nobel prize in 1975, suggests a quantum re-visitation of the macroscopic liquid drop model. The Bohr-Mottelson Hamiltonian considers a nucleus as a drop of *quantum* matter, merging collective and independent degrees of freedom.

Besides this macroscopic approach a variety of theoretical models, relying on a microscopic treatment of the nuclear interaction, have been developed. These mainly include the (large-scale) shell model and the self-consistent mean-field calculations.

The ab-initio methods, that have been mentioned above, won't be discussed further as they are not applicable in the mass region covered by the present experimental results.

1.1.1 The Bohr-Mottelson Hamiltonian and the collective behavior of nuclei

The Bohr-Mottelson collective model considers the nucleus as a liquid droplet, lead to describe nuclear excitation in terms of fundamental collective modes of rotations and vibrations of the surface [3, 4]. Energies of such a system come from the solution of Schrödinger equation with the Bohr-Mottelson Hamiltonian (Eq. 1.1.2), that describes a nucleus in term of its surface that could perform, under the influence of a certain potential V , multipole oscillations around a spherical or a deformed equilibrium shape. The Bohr-Mottelson Hamiltonian is written with the kinetic energy separated in a vibrational term T_{vib} , related with shape vibrations with fixed orientation in space, and a rotational term T_{rot} , related with a rotational motion of the nuclear surface without any change of shape:

$$H_B = T_{vib} + T_{rot} + V. \quad (1.1.2)$$

In order to describe vibrations and deformations of the nuclear surface, the nuclear radius is expressed, in polar coordinates, as an expansion in spherical harmonics $Y_{\lambda,\mu}$:

$$R(\theta, \phi) = R_0 \left(1 + \sum_{\lambda,\mu} \alpha_{\lambda,\mu} Y_{\lambda,\mu}(\theta, \phi) \right), \quad (1.1.3)$$

where R_0 is the radius of the nucleus when it assumes the spherical equilibrium shape. The index λ of the coefficients of the harmonic expansion coefficients, $\alpha_{\lambda,\mu}$, represents the multipolarity of the deformation.

Quadrupole ($\lambda = 2$) is the principal mode of deformation for most medium-mass nuclei at low excitation energies. In this mode, if $\alpha_{2\mu}$ is small, the surface of the nucleus is deformed like an ellipsoid randomly oriented in space. For $\lambda = 2$ Eq. 1.1.3 depends only on five coefficients $\{\alpha_{2\mu}\}$ which could be mapped onto the set of variables $\{\alpha_0, \alpha_2, \theta_1, \theta_2, \theta_3\}$. Variables α_0, α_2 are related to the extent of surface deformation and the last three variables describe angular orientations of the ellipsoid. Mapping the

system to an intrinsic frame of reference,¹ in which the orientation of the axes coincide with the principal symmetry axes of the ellipsoid, we reduce the problem to only two degrees of freedom, α_0, α_2 . The well-known deformation coordinates are obtained by rewriting α_0, α_2 as:

$$\begin{aligned}\alpha_0 &= \beta \cos \gamma, \\ \alpha_2 &= \frac{\beta}{\sqrt{2}} \sin \gamma.\end{aligned}\tag{1.1.4}$$

where the set $\{\beta, \gamma\}$ define a two-dimensional polar coordinate system within the five dimensional quadrupole deformation space.

In this coordinate system a shape is essentially described, in the intrinsic frame of reference, by a quadrupole deformation parameter β and an axial asymmetry parameter γ . $\sum_{\mu} \alpha_{\mu}^2 = \beta^2$ is the total deformation of the nucleus, in such a way that $\beta = 0$ represents a sphere and $\beta \neq 0$ is an ellipsoid. The larger the value of β , the more deformed the surface. The parameter γ describes the deviations from rotational symmetry.

In a two-dimensional polar plane where β is a radius and γ is an angle that could range from 0 to 2π , every point (β, γ) is associated with a fix ellipsoidal shape (see Figure 1.2). Each radius in the polar plot (marked with a solid line) of Figure 1.2 corresponds to an axially symmetric ellipsoid (prolate or oblate) with a well-specified symmetry axis. Every point in the areas within the radii corresponds to triaxial shapes, that are characterized by three different semi-axes. By re-labelling the axes in the intrinsic frame of reference, it is possible to confine this representation to a 60° wedge, due to the symmetry relationship as found by Bohr.

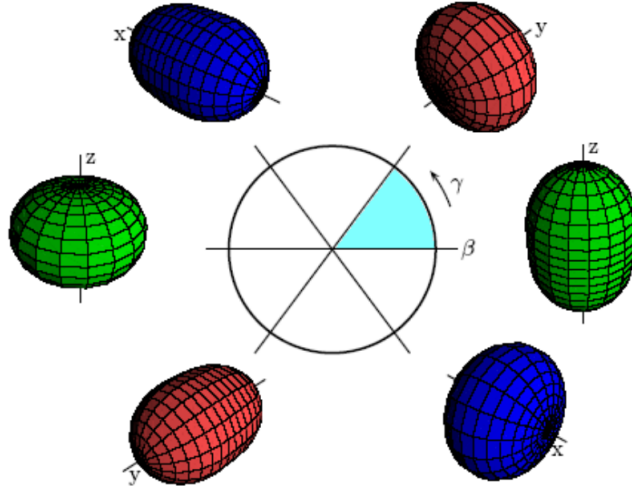


Figure 1.2: Deformation coordinates $\{\beta, \gamma\}$. The quadrupole deformed shapes corresponding to $\beta = 0.4$ and $\gamma = n\pi/3$ (with $n = 0, \dots, 5$) are shown for reference. Different colors are connected with different principal axes of symmetry (green for z, red for y and blue for x). The fundamental 60° wedge is sufficient to describe all possible intrinsic ellipsoidal shape.

The *prolate* shape, for $\gamma = 0^\circ$, results in a cigar-like shape, while the *oblate* shape, for $\gamma = 60^\circ$, results in a disc-like shape. When the γ is different from 0° or 60° , the nucleus

¹For nuclei the intrinsic reference frame can have any orientation with respect the laboratory reference frame. We could specify the mutual orientation of these two reference frame by using Euler angles.

is said to be triaxial, that is an ellipsoid with the rotational axis that does not match any of its symmetry axes, as shown in Figure 1.3. While the majority of nuclei have axially symmetric shapes, evidence for triaxial nuclear deformations has been elusive. The clearest signatures come from the γ -ray spectroscopy of rotating nuclei. If the system is triaxial, the associated rotational bands show specific features that allow for distinguishing it from an axial one [5].

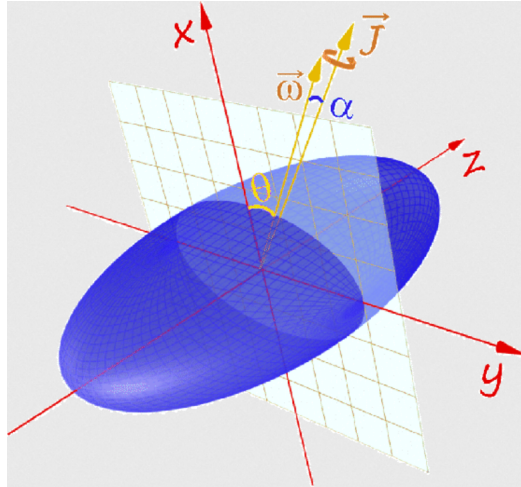


Figure 1.3: Schematic picture of a triaxial deformed shape. The angles θ (between the x -axis and the rotational axis) and α (between $\vec{\omega}$ and \vec{J}) are defined in the $x - y$ plane. The short, medium, and long axes of the ellipsoid are denoted by x , y , and z , respectively. Picture coming from reference [5].

The Bohr-Mottelson Hamiltonian contains a potential term, $V(\beta, \gamma)$ as a function of the deformation coordinates β and γ , that determines the behavior of the nuclear surface as a response of an external stimulus. The knowledge of this potential is essential to calculate eigenstates and eigenenergies of the nucleus by solving, analytically or numerically, the Bohr-Mottelson Hamiltonian. However, this potential is unknown, hence is important to rely on a good theoretical model.

Considering a more schematic situation of that presented above, we suppose the system to behave as a microscopic rigid rotor with moment of inertia \mathcal{I} . The energies obtained solving the equation for the Hamiltonian $H_{\text{rotor}} = \frac{\hbar^2}{2\mathcal{I}} \vec{J}^2$, as a function of the total angular momentum \vec{J} , are:

$$E_{\text{rotor}}(J) = \frac{\hbar^2}{2\mathcal{I}} J(J+1) \quad (1.1.5)$$

and can be related at the excited levels of a given rotational band of the nucleus. The typical energy difference obtained by Eq. 1.1.5, considering a constant (or slowly changing) momentum of inertia, lead to a very characteristic rotational spectrum (see later Figure 1.7).

1.1.2 Shell model

The nuclear shell model aims to explain the behavior of nuclei in a way which was successfully applied to atoms. It considers a nucleus as a set of A fermions which

occupy specific orbitals in a well-defined shell structure. Orbitals are the eigenstates of a Hamiltonian that considers a single nucleon inside a central mean-field nuclear potential, obtained averaging over the other $A-1$ particles (that can be modeled with square well, harmonic oscillatory, Wood-Saxon potential, etc...), which normally include the spin-orbit and the Coulomb contribution.

The Hamiltonian 1.1.1 can be rewritten bringing out a term for a common mean-field potential H_0 and the remaining term, H_{res} , that correspond to all the residual interactions between pairs of nucleons:

$$H = \left[\sum_{i=1}^A \frac{p_i^2}{2m_i} + U_i(r) \right] + \sum_{i>k=1}^A V_{i,k}(r_i - r_k) - \sum_{i=1}^A U_i(r) := H_0 + H_{res}. \quad (1.1.6)$$

The Hamiltonian H_0 considers non-interacting nucleons in a mean-field potential $U_i(r)$, that has to be chosen such that H_{res} can be treated as a perturbation.

The shell structure predicted with a spherical harmonic oscillator potential plus spin-orbit interaction is shown in Figure 1.4. Each orbital is characterized by three quantum numbers: the shell number N , the angular momentum

$$l = 0(s), 1(p), 2(d), 3(f), 4(g), \dots$$

and the total angular momentum $\vec{j} = \vec{l} + \vec{s}$, where $s = \pm 1/2$ is the spin. The parity of a state is related to the symmetry of the wave function of the state and depends on l through

$$\pi = (-1)^l.$$

The number of protons or neutrons that fill each orbital is equal to $2j + 1$, due to the projection of j onto the quantization axis, z , giving the quantum number m_j . Numbers in the right side of Figure 1.4 indicate the cumulative number of nucleons up to a major shell for such an Hamiltonian.

Neutrons and protons separately fill the different orbitals respecting the Pauli exclusion principle. According to the configuration assumed by fermions in the shell structure, the nucleus will be in a specific state with a proper energy. In a non-excited state the nucleons fill first the inner shells. Similarly to the atomic model, nucleons in a filled shell are not easily excited as nucleons in an unfilled shell, thus a closed shell is particular stable. There are groups of levels with relative energy distance much smaller than the distance between two such groups. The number of nucleons required to fill completely these major shell are called *magic numbers* and correspond to experimental evidence of an higher binding energy for the nucleus. For spherical nuclei close to stability magic numbers are:

$$N, Z = 2, 8, 20, 28, 50, 82, 126, \dots \quad (1.1.7)$$

If in a nucleus both numbers of protons and neutrons are equal to a magic number, the nucleus is tightly bound and is called doubly-magic. Considering the energy of the 2^+ state, one example of a doubly magic-nucleus is $^{56}_{28}\text{Ni}_{28}$ where the first excited state is at 2700 keV. We can compare this with the $^{60}_{30}\text{Zn}_{30}$ which has its first excited state at 1004 keV.

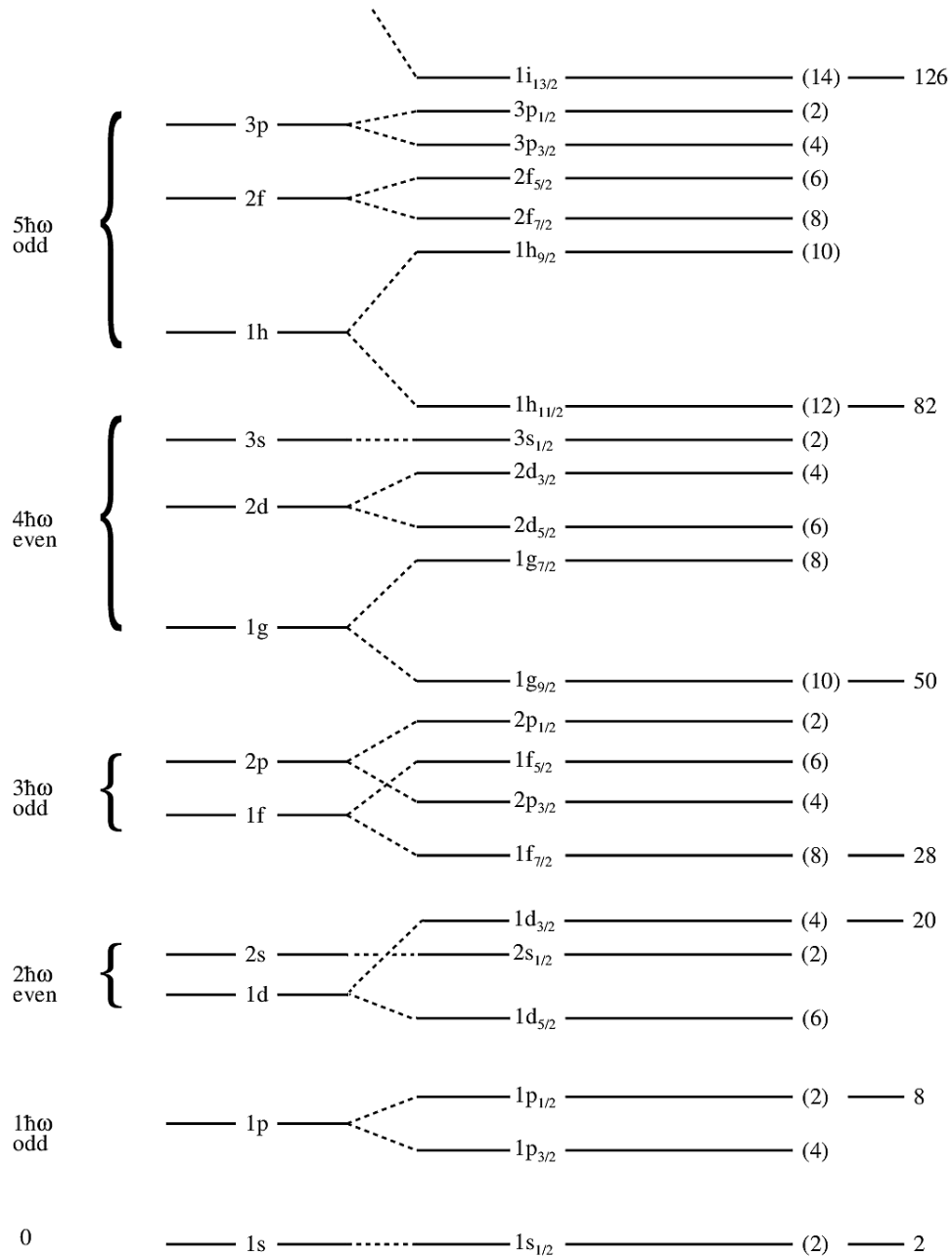


Figure 1.4: Shell model structure predicted with a spherical harmonic oscillator potential, unperturbed in the left side and with the integration with a spin-orbit interaction in the right side.

Due to the nuclear interaction properties, magic numbers are not universal. For example, deformation in exotic nuclei implies structural changes of energy levels which can lead to an alteration, or complete disappearance, of the well known shell closures.

When energy is brought into the system, the shell occupation is modified in different ways. One or more nucleons in the last occupied shell can move to an higher level or can leave a lower orbital, creating a *hole*. Also, pairing of two identical nucleons in an orbital can be broken. Nuclear excitations are naturally produced in this way with energies

and properties determined by the nucleons in the valence orbitals and considering the residual interactions between each other. The other nucleons, filling the shells below, are expected to form an inert core.

Shell model calculations are commonly used to describe the structure of light and medium-mass nuclei near shell closures, where we have to take into account only a few nucleons or holes. In heavier nuclei too many configurations become possible, being higher the number of nucleons outside a closed shell, and sophisticated ensemble of residual interactions has to be employed.

The residual interactions

The comparison between shell-model predictions and experimental energy levels of nuclei reveals that the application of an average potential is not sufficient to absorb the entire nucleon-nucleon interaction. As a consequence, the residual term H_{res} in equation 1.1.6 cannot be neglected. In certain cases the residual interactions are of the same order of magnitude of the separations between the single-particle levels, and the nuclear structure can be deeply modified. In the contest of deformation, the residual interactions between valence protons and neutrons, where the proton-neutron interaction energy is a major contribution, could drive the nucleus into a deformed shape [2].

The residual interaction can essentially be determined with three methods:

- Derive the residual interaction from first principles, i.e. from the nucleon-nucleon interaction.
- Exploit some simple interactions, as the Dirac δ .
- By fitting experimental data using two-body matrix elements. In this case the calculated interaction is usually named effective interaction.

1.1.3 Mean field

The complexity that arises when one treats a many-body system, such as the nucleus, comes from the huge number of degrees of freedom that must be considered. We are forced to seek simplifications where the number of relevant degrees of freedom is much lower. The simplest approximation of a N -body problem is to assume that each particle is subjected to a self-consistent mean field created by all other particles. For fermionic systems, this is the so-called *Hartree-Fock* approximation [6]. The Hartree-Fock method allows to derive a single-particle potential from the many-body interaction using a variational principle and Slater determinants as trial wave functions. The reduction of information to one-body degrees of freedom, when a Slater determinant is used instead of a more complex many-body state, can be seen as a projection of an optimum path onto the one-body space. One says in that case that the information on the system is contained entirely in one-body degrees of freedom and the knowledge of the system is reduced solely to the knowledge of the one-body $\rho^{(1)}$ density matrix. The one-body density matrix can be expressed microscopically in terms of the single-particle states as:

$$\rho_{ij} = \sum_{\alpha} \varphi_{\alpha}(i) \varphi_{\alpha}^*(j). \quad (1.1.8)$$

The variational method allows to obtain the best single-particle wave functions that minimize the total energy of the interacting system. The expectation value of H , using a Slater determinant of the type

$$|\Phi\rangle_{1,\dots,A}(\vec{r}_1, \dots, \vec{r}_A) = \prod_i \varphi_i(\vec{r}_i),$$

becomes a functional of the one-body density matrix components:

$$E_{HF}[\rho] = \frac{\langle\Phi|H|\Phi\rangle}{\langle\Phi|\Phi\rangle}. \quad (1.1.9)$$

The Hartree-Fock ground state is finally obtained by minimizing the energy in the space of Slater determinant. Successively, the single-particle states are obtained by solving the set of equations:

$$h_{HF}[\rho]|\varphi_i\rangle = \epsilon_i|\varphi_i\rangle \quad (1.1.10)$$

being h_{HF} the Hartree-Fock mean-field hamiltonian and ϵ_i the energy of the single-particle states.

It is indeed well known that Hartree-Fock method only starting from the bare nucleon-nucleon interaction is a poor approximation. This indicates that effects *beyond* Hartree-Fock are important. To treat this effect, one needs to introduce a residual interaction such that:

$$H_{nuc} = \sum_i h_{HF}(i) + V_{res}, \quad (1.1.11)$$

where the definition of V_{res} includes all that has not been accounted for in the mean-field part and requires many-body techniques. The huge number of degrees of freedom, with all their combinations, become soon a problem, overall for excited states, for computational reasons. Furthermore, the Hartree-Fock theory must be extended in some way to treat excitations and nuclear spectroscopy.

Guided by experimental observations, nuclear physicist have implemented the self-consistent mean-field models introducing the nuclear Energy Density Functional (EDF) concept, that is a simplification of the mean field. The EDF is a functional of powers and gradients of ground-state nucleon densities and currents, representing distributions of matter, spins, momentum and kinetic energy. This functional is defined by making use of effective forces like Skyrme [7] or Gogny [8] interaction to include correlations that arise from symmetry restoration and fluctuations around the mean-field minimum. One of the great advantage of nuclear EDF is its simplicity and its short computation time, so that massive comparisons with experimental data over the whole range of the nuclear chart can be made, especially for what concern charge densities. Using a specific effective force and the EDF method, it is possible to calculate the axial quadrupole deformation of the nuclei, and plot it in the (β, γ) space of the deformation parameters, together with the nucleus level scheme.

1.2 Shapes in nuclei: deformation and shape coexistence

The shape of a nucleus is a fundamental propriety that reflect the spatial distribution of nucleons but it is not a physics observable. Within the shell-model approach, doubly-closed nuclei favor a spherical shape for their ground state, since all orientation in space

of nucleons are equally probable. Far away from the closed shell the number of valence protons and neutrons increase and nuclei could assume a deformed equilibrium shape.

A wide variety of shapes have been theoretically predicted and experimentally observed from light to heaviest nuclei, with different shapes that often coexist in the same nucleus. It is predicted that the Segrè nuclear chart present typical areas of deformation, as we can see in Figure 1.5, where some experimental confirmations are also indicated, with mass numbers around 40, 60, 80, 130, 150, 190 and 240.

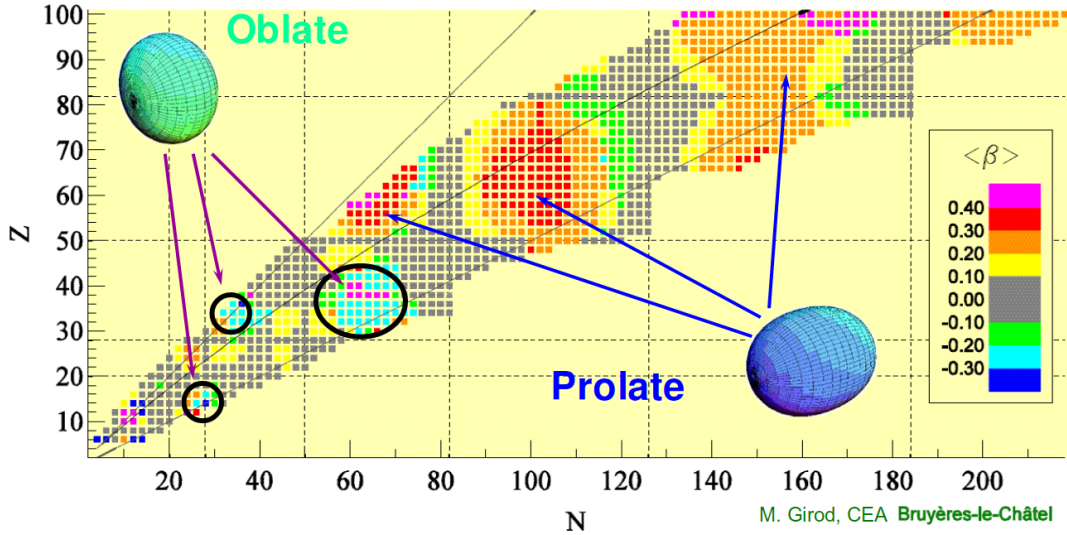


Figure 1.5: Quadrupole deformations of nuclear ground state are marked with different color in function of Z (vertical axis) and N (horizontal axis) [9].

Deformation comes from the property of a nucleus to reach a minimum in energy in a deformed shape, rather than a spherical one. Plotting the potential energy as function of the deformation parameters (β, γ) it is found that many potentials have minima for $\beta \neq 0$. The corresponding nuclei then reach the stability in a deformed shape [10]. An example of the potential energy as a function of the quadrupole deformation parameters (β, γ) is presented in Figure 1.6. In addition to the absolute minimum, that correspond to a spherical shape, other two local minima are visible. It is possible, for instance, that an oblate minimum coexists with the prolate minimum in the ground state.

When a nucleus exhibits low-lying states near in energy but characterized by a different shape, we could talk about a *shape coexistence*. In the early studies, shape coexistence was observed only near closed shell. The development of the investigations review the conditions needed to a system to manifest shape coexistence. However, the regions displaying shape coexistence fall on isotopes with a few nucleons off the magic number. Nuclei with more neutrons or protons out of shells, preferably show a strongly deformed shape in the ground state and there are less evidences of shape coexistence. For more detailed informations we refer to a recently review of shape coexistence by K. Heyde and J. Wood, Ref. [2].

If a nucleus assumes a certain shape in the ground state while it exhibits a pronounced different deformation at high excitation energy, we are talking about *superdeformation*. The first manifestation of the existence of super-deformed band was obtained by studying the ^{152}Dy isotope by Twin et al. [11], which exhibit series of γ transitions almost equally

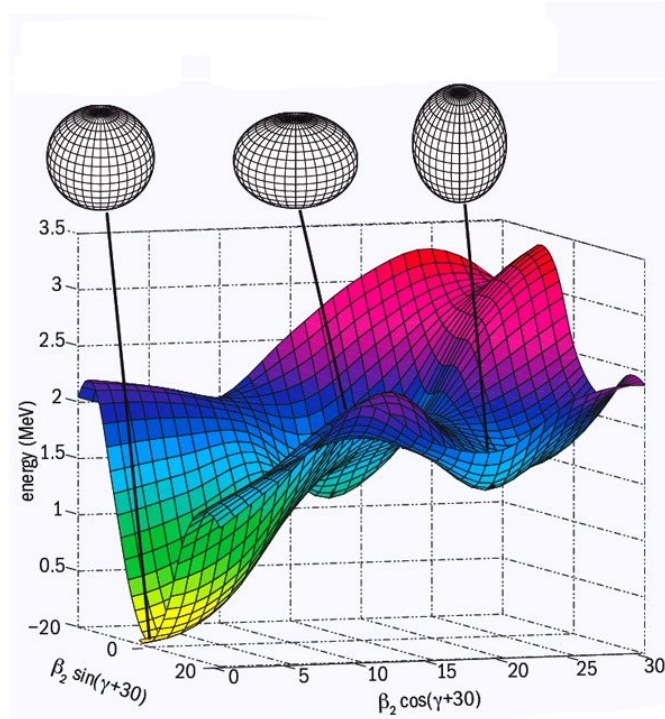


Figure 1.6: Potential energy surface for ^{186}Pb indicating the spherical, oblate and prolate minima (Andreyev et al. 2000). This is one of the most spectacular example of deformed shape. Here, studies of the α decay of the parent nucleus ^{190}Po have revealed a triplet of low-lying states ($E^* < 650$ keV). The nuclear potential energy surface suggest a spherical state in the ground state but many experiment probe the existence of bands build on the prolate and oblate shape for this system.

spaced. This is a characteristic of a clear deformed rotational nucleus, as shown in Figure 1.7.

The best information on the nuclear shape are the diagonal $E2$ matrix elements and the $B(E2)$ values, which require safe Coulomb excitation experiments and lifetime measurements, respectively [2]. These quantities are quite useful because they can be related to the intrinsic quadrupole moment and because, if combined, they do not depend on a specific nuclear model.

The estimate of the $BE(2)$ value is not the goal of the present work, but further shape investigations in the region of mass $A \sim 60$ may consider measurements of lifetimes or Coulomb excitations.

In our case, the experimental indication of the shape coexistence in even-even nuclei is the observation of the low-lying 0_2^+ state, which can be interpreted as the band head of a presumably different shape.

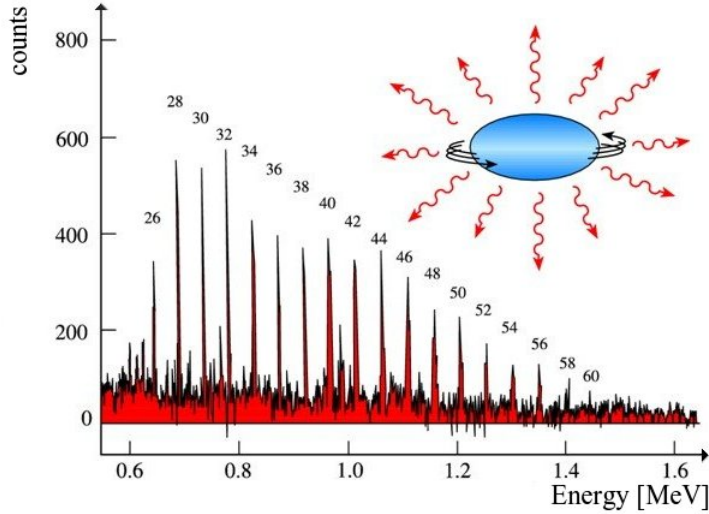


Figure 1.7: Gamma spectrum of ^{152}Dy isotope, a perfect manifestation of a rotational super-deformed band.

1.2.1 The region of $\text{N}=\text{Z}$ nuclei above ^{56}Ni

In the last decades, the structure and the properties of nuclei with an equal number of proton and neutron has been widely investigated, both experimentally and theoretically. Spectroscopy studies shed light on the structure of such nuclei and provide essential informations about the isospin symmetry of the nuclear force as well as the correlations between proton and neutron and their residual interactions. Due to the challenge in production of such exotic nuclei, new cutting-edge experimental tools became necessary like for example the advent of large Compton suppressed γ -ray arrays and associated ancillary detectors (Chapter 2).

Atomic nuclei in the region of mass between $28 < \text{N} = \text{Z} < 50$ present a remarkable diversity of shape. The ground state shape along the $\text{Z} = \text{N}$ line is predicted to change from spherical (^{56}Ni), triaxial (^{64}Ge), oblate (^{68}Se , ^{72}Kr), strongly prolate (^{76}Sr , ^{80}Zr), to spherical again (^{84}Mo) as $\text{N} = \text{Z}$ increases [12]. These deformation effects could be associated principally to two facts:

- Valence nucleons occupy the fpg -shell. The large occupation numbers of the shell-model orbitals $2p_{3/2}$, $1f_{5/2}$, $2p_{1/2}$, $1g_{9/2}$ (see Figure 1.4), in which valence nucleons could be arranged, provide a large amount of possible configurations.
- Protons and neutrons occupy the same level ($\text{N} = \text{Z}$). The resulting overlap of the nucleon wave functions leads to an amplification of the residual proton-neutron interactions and promote an extreme sensitivity of nuclear properties to small changes of nucleon numbers.

The residual interactions depend on which particular orbital is occupied by protons and neutrons. By studying excited levels in a self-conjugated system, it is possible to achieve informations about residual interactions.

The current knowledge is that for deformed nuclei there is an extreme scarcity of axial-oblate shape, when compared with the much more frequent occurrence of prolate

system. The considerations about shape deformations, as a function of Z and N , involve microscopic and macroscopic effects that are symmetric in the sign of deformation, suggesting that the prolate and the oblate shape should occur with approximately the same frequency [13]. Oblate and non-axial shape (such as triaxiality) are predicted far from stability, thus investigations in region of the Segré chart that exhibit these features become of extraordinary importance (see Figure 1.5). Manifestations of the above effects are the neutron-deficient nuclei above the doubly-closed ^{56}Ni nucleus, that change rapidly their collective properties, moving from the spherical shape of ^{56}Ni to the prolate deformation of ^{80}Zr .

1.2.2 The case of ^{60}Zn

The zinc isotope ^{60}Zn is placed at the lower edge of the region of transitional nuclei described in the previous paragraph. For this nucleus the interplay between the stabilizing effects of the near closed shell and the residual correlation energy gains by valence nucleons is very subtle, being very close to $N=Z=28$ nucleus, ^{56}Ni .

In the seventies, excited levels in ^{60}Zn have been populated in the $(3\text{He},n)$ reaction and their energy and spin parity was assigned by fitting the neutron angular distributions [14].

Afterwards, in a following experiment, γ rays emitted in $(3\text{He},n\gamma)$ reaction have been also detected by using the same reaction [15]. In this experiment, informations about the γ decay of the levels was obtained by measuring direct γ radiation in coincidence with the outgoing neutrons. In Figure 1.8 we show the proposed level scheme from this work.

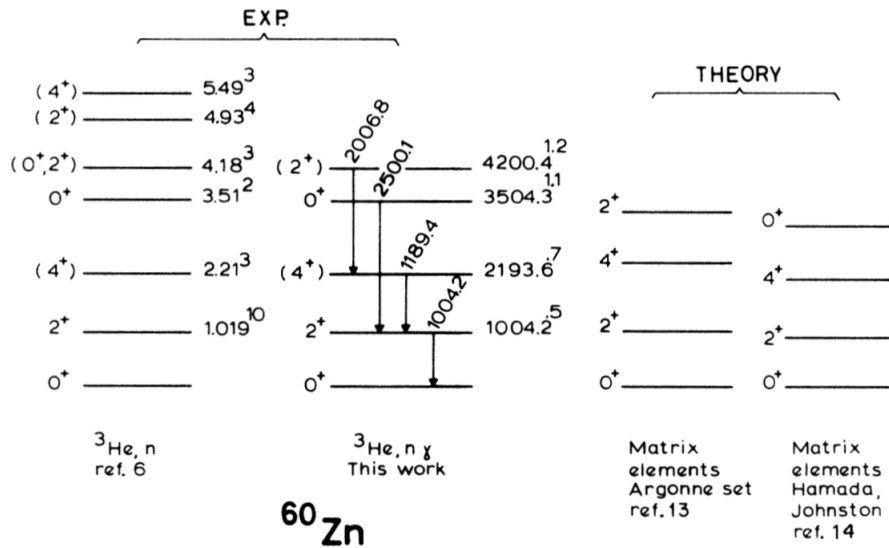


Figure 1.8: Proposed level scheme of ^{60}Zn from Ref. [15]. Reference 6, cited in the level scheme on the left, is the study [14] mentioned above. By assuming ^{58}Ni as an inert core, shell model calculations for ^{60}Zn were done with matrix elements derived from Hamada-Johnston potentials and Argonne interaction (see [15] for these reference). These two calculations are shown in the right side of figure and compared with the experimental data.

The assigned spin and parity were speculated on the basis of previously assigned values and intensity and no γ - γ coincidence were obtained. The resulting level scheme

is therefore far from being firmly established. Comparison with shell-model calculations, using a inert ^{56}Ni core and trimmed matrix elements, could reproduce the excited 0_2^+ state.

Theoretical shell-model calculations, using a pairing plus quadrupole-quadrupole force in fpg model space, predict a prolate to oblate transition in $N=Z$ nuclei above ^{56}Ni , by moving from the ^{60}Zn to ^{68}Se , and shape coexistence for the ^{60}Zn , ^{64}Ge and ^{68}Se nuclei [16]. In Figure 1.9 on the right, the calculated energy spectra are compared with experimental data in the fpg -shell nuclei, ^{60}Zn , ^{64}Ge and ^{68}Se . In addition to the ground-state band, the second positive-parity band, beginning from the $J^\pi = 2^+$ state, is reported in these three nuclei. Figure 1.9 on the left shows the calculated spectroscopic quadrupole moments for the first and second excited 2^+ states for ^{60}Zn , ^{64}Ge and ^{68}Se .

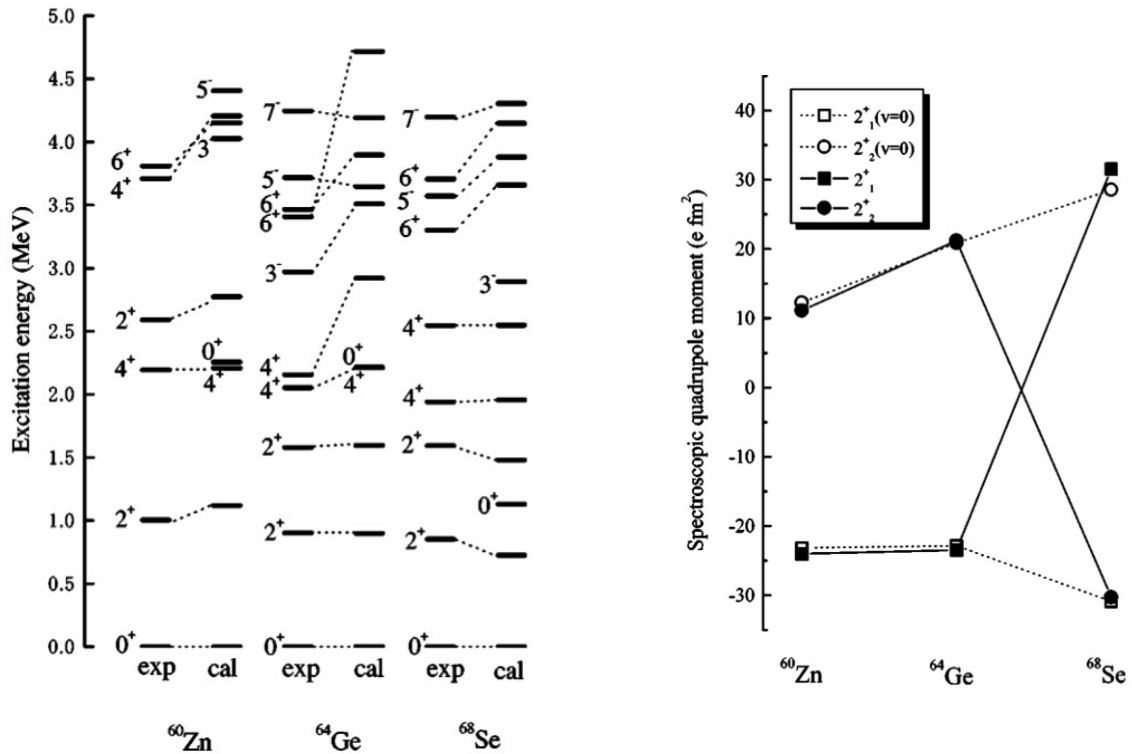


Figure 1.9: On the right, experimental and calculated energy levels, and, on the left, spectroscopic quadrupole moments of ^{60}Zn , ^{64}Ge and ^{68}Se . The solid squares and circles are quadrupole moments of the first and second excited 2^+ states, respectively, obtained by the shell-model calculations. The open squares and circles are those obtained by ignoring the $T=1$ monopole matrix elements [16].

Indeed, energy-density functional calculations (EDF), presented in Chapter 5, do not predict coexistence for ^{60}Zn , but rather a γ -soft potential, or a triaxial deformation.

So far, in this nucleus, neither a firm assignment for the 0_2^+ and 2_2^+ level exist, nor experimental information suffices to prove the predictions of coexisting band.

Therefore, the goal of the present work is to measure 0_2^+ and 2_2^+ state and to produce an assignment of the existence of a side band at low energy and thus shape coexistence or triaxial nature for this nucleus. This will be achieved by measuring the energy of the transitions de-exciting the non-yrast low-lying states 0_2^+ and 2_2^+ .

Chapter 2

The experimental setup for fusion-evaporation reactions at LNL

The experiment reported in this thesis was performed at the Legnaro National Laboratories, during May 2016. In this Chapter, the experimental setup, the accelerator and the detection devices are described. A brief introduction of the fusion-evaporation reactions is also given, while the basic notions on γ -ray spectroscopy and interaction of γ rays with matter are included in the Appendix.

2.1 The nucleus ^{60}Zn and the reaction to populate its excited states

Shape coexistence is a fundamental phenomenon occurring in most of the nuclei. The goal of the experiment was to study such effects in the ^{60}Zn , by measuring the energy of the transitions de-exciting the non-yrast low-lying states 0_2^+ and 2_2^+ .

To explore the shape coexistence in ^{60}Zn , an asymmetrically fusion-evaporation reaction is required, in order to populate non-yrast states that should form the side band, as well as the yrast ones. The energy of the ^{12}C beam was chosen at 60 MeV, well above the Coulomb barrier, in order to maximize the reaction cross section. The same approach was successfully used in the $^{12}\text{C}(^{58}\text{Ni},2n)^{68}\text{Se}$ reaction, at a beam energy 50% higher than the Coulomb barrier, where both yrast and non-yrast levels were populated [13].

The high selectivity of GALILEO in combination with the Neutron Wall and EUCLIDES will allow to resolve the γ -ray transitions de-exciting the side band and the transitions feeding the ground-state band. With this experiment we thus intend to probe the existence of the expected second-oblate band which has a different nature with respect to the prolate ground-state band.

The reaction used to populate excited states in ^{60}Zn was:



The corresponding reaction channel can be selected by placing conditions on the charged particles (EUCLIDES) and neutrons (Neutron Wall) that are evaporated by the compound nucleus, ^{66}Ge .

A target of ^{54}Fe of 2 mg/cm^2 thickness is located within the EUCLIDES charged particle detector, where a vacuum of 10^{-6} mb was obtained. The beam of ^{12}C , produced with a sputtering ion source, is accelerated by the Tandem XTU accelerator. A target as thick as possible is used to enhance the yield of the reaction, ensuring, at the same time, that the low-spin excited states of ^{60}Zn , produced inside the target, leave the target before they decay, according with their lifetimes. A low-lying excited state has a typical lifetime of few ps. With increasing spin, usually lifetimes become shorter. For our purpose, a maximum target thickness of 2 mg/cm^2 was adopted considering that the states of interest have spin 0 and 2 and a lifetime from few hundred of fs to few ps.

2.1.1 Fusion-evaporation reactions

Fusion-evaporation reactions are a standard experimental technique for populating excited states in atomic nuclei [17]. It practically consists to accelerate a nucleus (projectile) at a certain energy on a nucleus at rest (target). If the energy of the projectile is high enough, the projectile and the target fuse together and form a nucleus (compound nucleus) with a number of neutron and proton equal to the sum of those of projectile and target.

When two nuclei approach to each other, an interaction potential $V(r)$ rises giving form to a potential barrier due to the combination of the attractive nuclear interaction and the coulombian repulsion between the two nuclei (see Figure 2.1). In order that a fusion reaction take place, the energy of the system must exceed the energy of the Coulomb barrier.

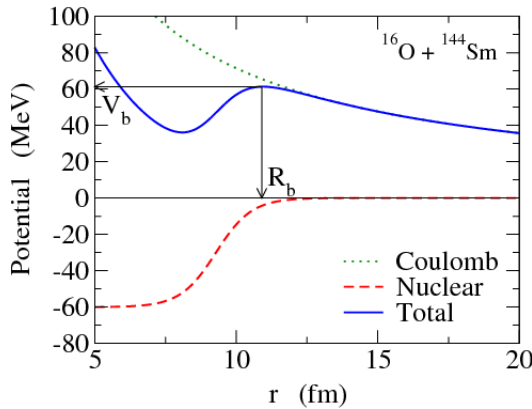


Figure 2.1: The interaction potential $V(r)$ is the sum of the attractive nuclear potential $V_{Nuclear}(r)$ and the repulsion electrostatic potential $V_{Coulomb}(r)$. Here for the system $^{144}\text{Sm}+^{16}\text{O}$. R_b and $V_b = V(R_b)$ are the radius and the height of the Coulomb barrier respectively.

The compound nucleus is produced in a highly excited state. Its energy

$$E_{ex} = E_{CM} + Q, \quad (2.1.1)$$

is the sum of the Q -value of the reaction and the kinetic energy of the system in the center of mass frame, calculated via

$$E_{CM} = E_B \frac{m_t}{m_t + m_p}, \quad (2.1.2)$$

where E_B is the beam energy, m_t, m_p the masses of the target and the projectile respectively. The angular momentum transferred to the compound nucleus is proportional to the linear momentum $m_p v$ of the beam particles and to the impact parameter b through

$$l = m_p v b. \quad (2.1.3)$$

From this formula, higher incident beam energies result in larger angular momentum of the compound system.

The excited compound nucleus is very unstable and within 10^{-19} seconds begins to emit (evaporate) light particles like α particles, protons and neutrons, losing a lot of its energy. Typically, α particles take away ~ 15 MeV, protons ~ 6 MeV and neutrons ~ 2 MeV. The compound nucleus can also de-excited via fission. In our case the fission channel is very unlikely because of the low mass of the compound nucleus.

The evaporation process finally ends in a nucleus (the evaporation residual) at high excitation energy and spin (depending on how the reaction is asymmetric) since the evaporated light particles can only carry away a few units of angular momentum. At this point the nucleus cools down by emission of γ -rays, until the cascade reaches the yrast line and then ends at the ground state. The yrast line is the line connecting the lowest energy states for a given value of angular momentum (yrast states).

For a certain system, the decay probability depends only on the total energy given to the system; in effect, the compound nucleus “forgets” the process of formation and decays governed primarily by statistical rules. In the region of $A \sim 60$ mass the evaporation process favors the emission of α particles and protons, rather than neutrons.

When dealing with fusion-evaporation reactions we often uses the word *channel* to refer to a certain combination of evaporated particles. For instance, from the compound nucleus $^{66}_{32}\text{Ge}$, the residual nuclei $^{60}_{29}\text{Cu}$, $^{61}_{30}\text{Zn}$ and $^{60}_{30}\text{Zn}$ are formed via the so-called $1\alpha 1p1n$, $1\alpha 1n$, and $1\alpha 2n$ channels, respectively.

The whole process is quite fast and within $10^{-11} - 10^{-9}$ seconds the particles and γ -rays have been emitted and the residual nucleus has reached its ground state. A schematic picture of the fusion-evaporation reaction process is presented in Figure 2.2.

2.1.2 The acceleration system: Tandem XTU

The Tandem XTU is a electrostatic accelerator build in the mid-80's at the Legnaro National Laboratories; it accelerates particle beams of energy in the range $5 \div 10$ MeV/A. At the center of the accelerator, an High Voltage Terminal (HVT) can reach a nominal tension of about 16 MV. To prevent electric shock because of the high voltage, it is located inside a tank (shown in Figure 2.3) filled with an insulation gas (SF₆ sulfur hexafluoride) at about 7 atm nominal pressure [19, 20].

Ions to be accelerated are generated outside the tandem by a sputtering source and by crossing through a highly electro-positive gas (Cs), they take a weakly negative

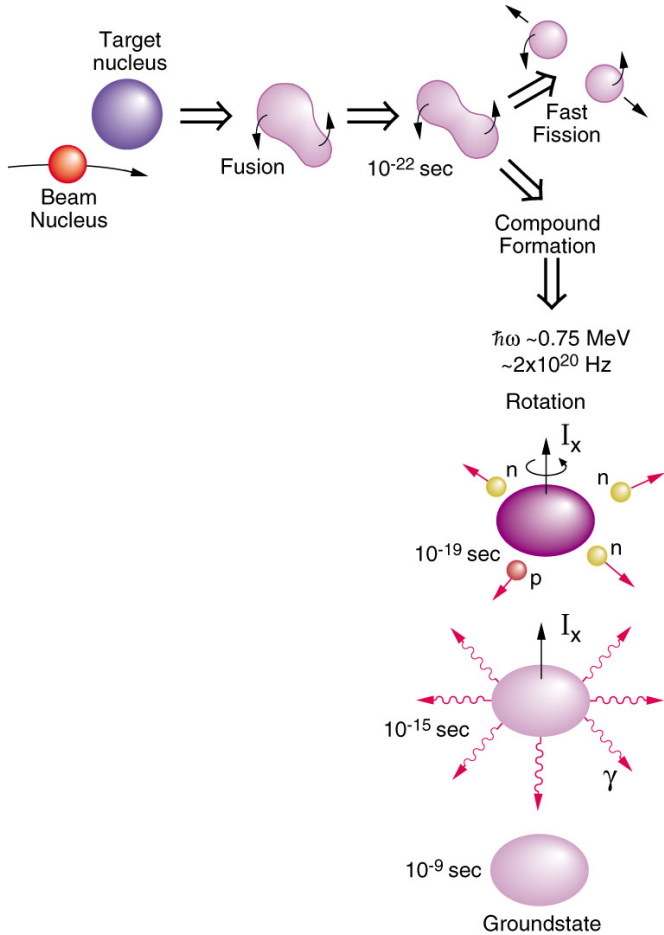


Figure 2.2: Schematic picture of the fusion-evaporation reaction process taken from [18]. See text for details.

charge ($q = -1$). With such charge state, ions enter the tandem and are attracted (i.e. accelerated) towards the HVT at max $VT = +16$ MV. Here, ions pass through a very thin carbon foil (called "stripper") that, absorbing a relatively small fraction of beam current, removes a number of electrons (up to $10 \div 20$, depending on the ion type and acquired energy). Now ions leave HVT with a highly positive charged state and therefore they undergo an attractive electrostatic force in the second half of tandem. The charging current to the high voltage terminal will be delivered by two laddertrons charging system.

At the exit of Tandem ions are driven by magnetic deflectors and lenses, and distributed by a switching magnet, towards the desired beam line where the appropriate experimental apparatus is located.

2.2 γ -ray detection devices

The design of a γ -ray detector needs to take into account the interaction of γ -rays with matter and the various kind of detectors that can be used, such as gas detectors, scintillator detectors or semiconductor detectors. The best energy resolution for a γ -ray spectroscopy study is achieved by a semiconductor detector where, by measuring the

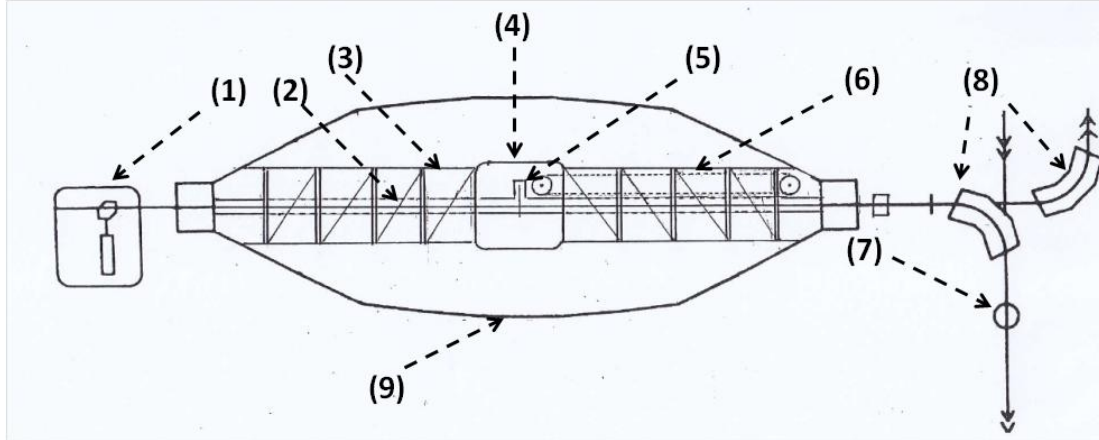


Figure 2.3: Schematic diagram of a Tandem accelerator (courtesy by F. Cervellera). The following elements may be identified: the ion source platform (1); the accelerating pipe (2); the column (3) which supports the high voltage terminal (4), where the ion beam “stripping” station is located (5); the laddertron charging belt (6); the beam diagnostic station (7); bending magnets (8); enclosure tank filled in SF6 gas at 7 atm pressure (9) [19].

electron-hole pairs number, it is possible to derive the intensity of the incident radiation. An ideal material for a γ -ray detector does not exist and a compromise between efficiency and resolution have to be reached.

Advances in detector technology resulted in new discoveries and innovations have improved detector performance (energy resolution, efficiency, peak-to-total ratio, polarization, angular distributions, auxiliary detectors). Nowadays germanium is the common choice for in-beam γ -ray spectroscopy. Due to the low Z of Ge, the Compton effect is the dominating interaction process for $E > 180$ keV (as explained in A). The Compton continuum of all the γ -rays summed in the spectrum, creates Compton background and makes the identification of a weak full-energy peak challenging.

Actually, two different technologies are used to overcome the problem of background derived from Compton-scattered events in a γ spectrum. These are the Compton suppression technology (GAMMASPHERE, EUROBALL, GALILEO, ...) and the γ -ray tracking technology (AGATA, GRETA, ...) [21].

- Compton suppression technology consists in surrounding each Ge detector of an array by a large scintillator detector, used as an escape-suppression shield. The main detector and the suppression detector are adopted in anti-coincidence, i.e. if the γ -ray has scattered out of the main detector before depositing all of its energy, then both the detectors detect the γ -ray in coincidence and such event is discarded. In this way, mostly full energy events are acquired and the Compton continuum is reduced with an improvement of the peak-to-total ratio.
- The γ -ray tracking technology use segmented Ge detectors where energy, time and position of all interactions are recorded to reconstruct the full interaction through proper tracking algorithms. In a segmented Ge detector a single crystal is divided into many electric segments. The high granularity due to segmentation allows an accurate Doppler correction resulting in an improvement of the energy resolution. Moreover, the absence of a suppressed shield enables a quasi- 4π coverage, enhancing the total detector efficiency.

The resolution of a detector is always a function of the incident radiation energy and depends on many contributions. It is a fundamental propriety to distinguish an energy peak from the background and Ge detectors are characterized by a great energy resolution.

The highest is the energy resolution, the smallest is the FWHM of a peak. The contribution to the FWHM of a γ line by the statistical fluctuation is given by

$$\Delta E_\gamma = 2.35 \sqrt{F \cdot 2.96 \cdot E_\gamma} = 1.28 \sqrt{E_\gamma}.$$

where F is a correction factor introduced by Fano in attempt to quantify the departure of the observed statistical fluctuations in the number of charge carries for pure Poisson statistics.

The other main contribution to the energy resolution comes from the detector current and the noise of the preamplifier. The noise contribution of the preamplifier and especially of the field-effect transistor (FET) at the input stage makes a significant contribution to the resolution.

The intrinsic resolution ΔE of a Ge detector is related to the width of energy peaks and varies depending on the energy of the incoming γ ray. In order to determinate the value of ΔE of different detectors, it is a standard practice to quote the intrinsic resolution at an energy of 1332 keV of a ^{60}Co source.

2.2.1 The GALILEO γ -ray spectrometer

GALILEO is a γ -ray spectrometer recently installed at the Legnaro National Laboratory. GALILEO [22] is composed by Compton suppressed Ge detectors and use anti-Compton shields of BGO ($\text{Bi}_4\text{Ge}_3\text{O}_{12}$) scintillator in order to reach, for the whole array, a peak-to-total ratio of about 50%. In present configuration, GALILEO consists on 25 GASP detectors (together with their anti-Compton shields), placed at 22.5 cm from the target position, arranged on 4 rings at 90, 121, 129 and 159 degrees with respect to the beam axis. Figure 2.4 shows, on the left, the array infrastructure together with the Neutron Wall and, on the right, a frontal view of GALILEO with the 10 detectors at 90°, visible in foreground, and the remaining 15 detectors, at backward angles, covered behind them.

The GALILEO spectrometer uses a novel digital electronics able to sustain the high counting rate expected in experiments with intense stable beams. The GALILEO electronics digitizes the signals from each germanium crystal and the respective anti-Compton shield.

For GALILEO the intrinsic FWHM at 1332 keV is around 2.4 keV, corresponding to a relative intrinsic error, $\Delta E/E$, of about 0.18%. The total efficiency is estimated around 2.4%, at 1332.5 keV. In the next section we will discuss in detail the efficiency calibration of GALILEO spectrometer.

According to the different experimental conditions, GALILEO can be coupled with different ancillary detectors: a light-charged particles detector like EUCLIDES, SPIDER or TRACE, the Neutron Wall detector and the plunger device.

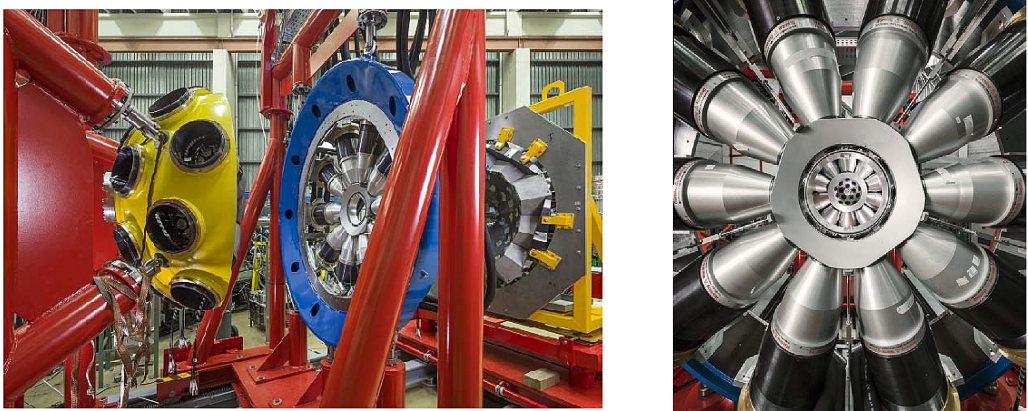


Figure 2.4: On the left, a picture of the GALILEO infrastructure with the Neutron Wall. On the right, a frontal view of GALILEO. The 10 detectors placed at 90° are visible, hiding the shell with the remaining 15 detectors [22].

2.3 Ancillary detectors

In a fusion-evaporation reaction many different reaction channels are open. In our case the compound nucleus is ^{66}Ge that it can evaporate different kinds of particles. Each evaporation residue is produced with a different cross section (see Table 4.1 for the most probable evaporation residues). Each residual nucleus de-excites through γ radiation detected by the GALILEO spectrometer. The intensity of a peak in the γ spectrum is proportional to the cross section of the corresponding residual nucleus. If a nucleus is produced with a small cross section it is challenging to extract its γ -ray decay since it is hidden in the background, due to the other most intense channels.

For example, the channel that provides the evaporation residue ^{60}Zn is



and has a predicted cross section of about 1 mb. The ^{66}Ge is an exotic proton-rich nucleus and exotic nuclei are usually produced with a relative small cross section. Therefore, to overcome the difficulties in the observation of these nuclei, detection systems with an high resolving power had to be developed. In the present configuration GALILEO can be used in conjunction with ancillary devices to improve the selectivity and reduce the background in the final spectrum for the nucleus of interest. In our experiment, the ancillary detectors are the charged particle detector, EUCLIDES, and the neutron detector, Neutron Wall. The detection in coincidence of a fixed set of particle allows to isolate a particular reaction channel and to produce a γ spectrum where in principle only γ -ray energies emitted from a certain nucleus are presented. In order to select the γ -rays emitted by ^{60}Zn , it is necessary to observe in coincidence one α in EUCLIDES and two neutrons on the NW.

Furthermore, the resolution in a γ spectrum is also related to the Doppler broadening (as fully explained in Section 3.3) due to the Doppler effect present when a γ -ray is emitted by a nucleus with a velocity $\beta \neq 0$. An event-by-event kinematic reconstruction to reduce the Doppler broadening and correct for the Doppler shift is possible with the informations coming from the ancillary detector EUCLIDES.

Summarizing, a channel selection to enhance the resolving power and a kinematics Doppler correction to improve the energy resolution are both possible with the use of ancillary detectors.

2.3.1 The charged-particle detector EUCLIDES

EUCLIDES [23] is an high efficient 4π light charged particle Si detector and it is principally used as an ancillary device for GALILEO.

The EUCLIDES array consist of 40 ΔE -E n-type silicon detectors arranged in a 42-faces polyhedron. Two of these faces are empty and used for the incoming and outgoing beam. The Si thickness is $\sim 130 \mu\text{m}$ for ΔE and $\sim 1000 \mu\text{m}$ for E layers. The E layer is placed behind the thinner one and they have the same area, which is about 10.2 cm^2 .

The telescopes are arranged in a self-supported structure so that the distance between neighbouring telescopes is 0.2 mm. The reaction chamber, with a diameter of 20 cm, hold EUCLIDES with its support structure and cables.

To achieve a proper channel selection EUCLIDES relies on the ΔE -E method. The energy loss in the ΔE layer and the total energy loss in the second E layer follow the Bethe-Bloch equation. A correlation matrix ΔE -E show locus of points characteristic of a certain particle. The ΔE -E matrix is reported in Figure 3.9 of Chapter 3, where the details of the particle identifications are given.

The Bethe-Bloch formula describes the mean energy loss per distance traveled by a charged particle with velocity $v = \beta c$ through a medium with density ρ , atomic number Z and relative atomic mass A. The interaction of the particle within the material ionizes the atoms and leads to an energy loss of the traveling particle. For low energies, i.e. for small velocities of the particle $\beta \ll 1$, the Bethe-Bloch formula has its classical version:

$$-\frac{dE}{dx} = \frac{4\pi n z^2}{m_e v^2} \cdot \left(\frac{e^2}{4\pi \varepsilon_0} \right)^2 \cdot \left[\ln \left(\frac{2m_e v^2}{I} \right) \right], \quad (2.3.1)$$

where

$$n = \frac{N_A Z \rho}{A M_u} \quad (2.3.2)$$

is the electron density of the material, with N_A the Avogadro number and M_u the Molar mass constant.

At even lower energy the expression 2.3.1 can be approximated to:

$$-\frac{dE}{dx} \propto \frac{z^2}{v^2} = \frac{z^2 M}{E} \quad \rightarrow \quad E \frac{dE}{dx} \propto -z^2 M \quad (2.3.3)$$

and therefore an identification of (z, M) from different hyperboles in the $(E, \Delta E)$ plane is possible.

To achieve a good particle discrimination for kinematic reconstruction, E detectors should be as thick as possible. In fact the total energy of light-particle is required to perform an accurate calculation of the value of β of the emitting nucleus.

Low energy particles stop inside the ΔE layer. These events are visible in the ΔE -E matrix along the vertical axis.

EUCLIDES is an high efficiency detector thanks to its almost 4π solid angular coverage and because of its segmentation in 40 telescopes that minimize the multiple hit probability in the same telescope. Furthermore, the high segmentation allows a good kinematic Doppler correction.

The segmentation also allows to reduce the problem of pile-up, that arises when the individual detector counting rate exceeds several tens of kHz. Since in a typical fusion-evaporation reaction most particles are emitted in the forward, the forward detectors can hardly sustain such high counting rate. To overcome this problem, the 5 forward telescopes are segmented (see Figure 2.5) in 4 identical sectors. Thus, the total counting rate for such segmented detector could reach about 100 kHz, a limit that has not yet attained during any of the experiments performed so far.

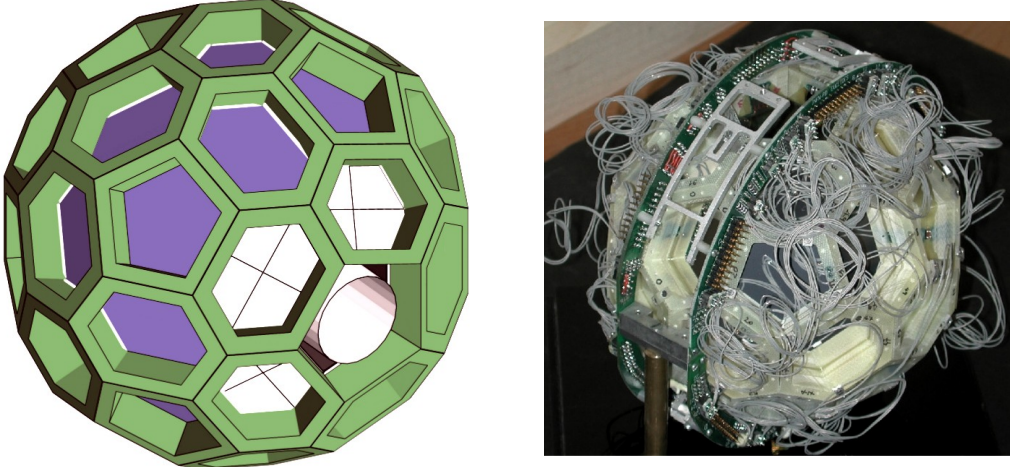


Figure 2.5: Schematic view of EUCLIDES array on the left with the insert absorber; a picture of the fully assembled detector on the right.

An Upilex absorber, with $7\text{-}\mu\text{m}$ thickness, is permanently placed in front of each telescope for mechanical and electrical protection. An additional cylindrical layer of Al is placed inside EUCLIDES (as shown in Figure 2.5) with the aim of preventing the elastically scattered beam to reach the detector. The layer of the absorber must be such to stop every scattered nuclei of ^{12}C , but allowing most of the light particles to pass. A detailed calculation as been performed to adjust the thickness of the absorber foil as explained in Section 3.6.

The EUCLIDES electronic is fully digital and is based on the time stamp distributed by the GTS (Global Trigger and Synchronization) system which enables the coincidence between GALILEO, EUCLIDES and the Neutron Wall. The EUCLIDES detectors are read out by home-designed preamplifier for Si detectors. From preamplifiers the signals are sent to four 32-channel Digitizer. The data are finally processed in a FPGA (Field Programmable Gate Array) where custom algorithms select the informations from the events of interest and send the data to the hosting PC. Inside FPGA the data are grouped into Domains. Each domain has one logic trigger (ΔE layer) and a slave channel (E detector). The occurrence of the trigger channel forces the readout on both sub-domains (ΔE and E). FPGA performs digital trapezoidal shaping of the acquired signals to retrieve the information on the amplitude of the signal which is proportional to the energy deposited inside each Si-detector [23].

The estimated total efficiency for α -particles and protons is of the order of 55% and 30% respectively, as described in Ref. [24] (to be published).

2.3.2 The Neutron Wall detector

The use of a neutron detector is very important for the study of neutron-deficient nuclei, where the identification of very weak reaction channels are often characterized by the evaporation of one or few neutrons.

Neutron Wall [25] is an array of liquid organic scintillators BC501. It is formed by 15 hexagonal detectors (H1 10 units and H2 5 units) and 1 pentagonal detector (P) (see Figure 2.6). H1 and H2 detectors have 3 segments per unit, each one filled with 3.2 liters of liquid scintillator (BC501). P detector is composed by 5 segments, 1.1 liters each.

In the GALILEO configuration, there is a total of 45 detector segments for a volume of liquid scintillator of about 150 liters.

The detectors are mounted in a closely packed configuration forming a pseudo-spherical shell that covers about 30% of 4π solid angle. NW is mounted in the forward hemisphere, with GALILEO detectors occupying the backward hemisphere. The distance from the target to the front face of the detectors is about 50 cm.

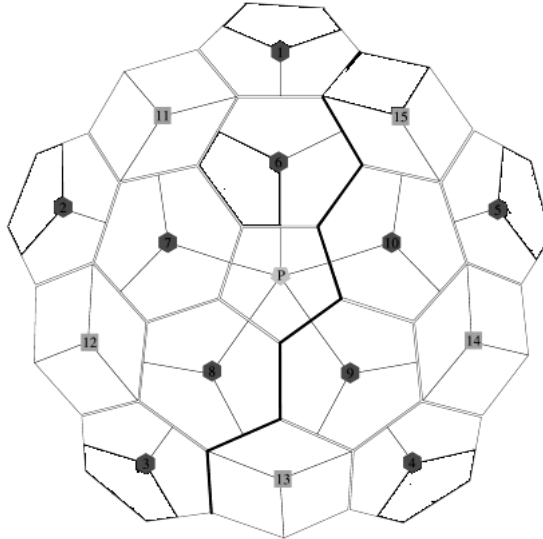


Figure 2.6: Schematic view of Neutron Wall.

The mechanism for neutron detection, in the scintillator liquid, is an elastic scattering of neutrons on protons. When a neutron hits a proton of the liquid, the proton gains kinetic energy that will be lost by slowing down into the scintillator. Its kinetic energy is therefore converted into internal excitations of the molecules of the liquid. When these molecules de-excite, they emit photons with wavelengths suitable for detection by the Photomultiplier Tube (PMT), which preamplifies the light signal [26].

For each event, the ZCO (Zero Cross Over) and TOF (Time Of Flight) parameters, as well as the QVC (charge integrated anode signal) are read out for all neutron detectors which have triggered and given a signal above the selected CFD threshold.

The pre-trigger for a NW event was chosen as $2\gamma 2n$. This means that the data acquisition starts when 2 γ and 2 hits (γ -rays or neutrons within a one-dimensional gate in the ZCO, see Figure 2.7) are simultaneously present in GALILEO and NW detectors respectively. The read out electronic of NW is analogic, resulting in a high dead time with respect to the rate of the incoming neutrons and γ 's, in our experimental conditions. Without any particle trigger we can loose many good events ($2n$ events for our reaction channel); in contrast the $2\gamma 2n$ trigger allows the data acquisition to record the events of interest and to reduce the dead time.

The typical total efficiency of NW, considering its 1Ω angular coverage, is $\epsilon_n = 25 \div 30\%$ and $\epsilon_{2n} = 3\%$, for the detection of one neutron and two neutrons respectively [27].

Neutrons and γ -particles are tagged during the acquisition by the ZCO information. A typical ZCO spectrum is shows in Figure 2.7. Two peaks are visible, the neutron peak on the left side of the spectrum and the γ peak on the right. A gate directly on the ZCO information discriminate the neutrons from the γ particle. Of course this distinction is not perfect and, in fact, instead of a nn , we can have some γn and even $\gamma\gamma$ events as trigger.

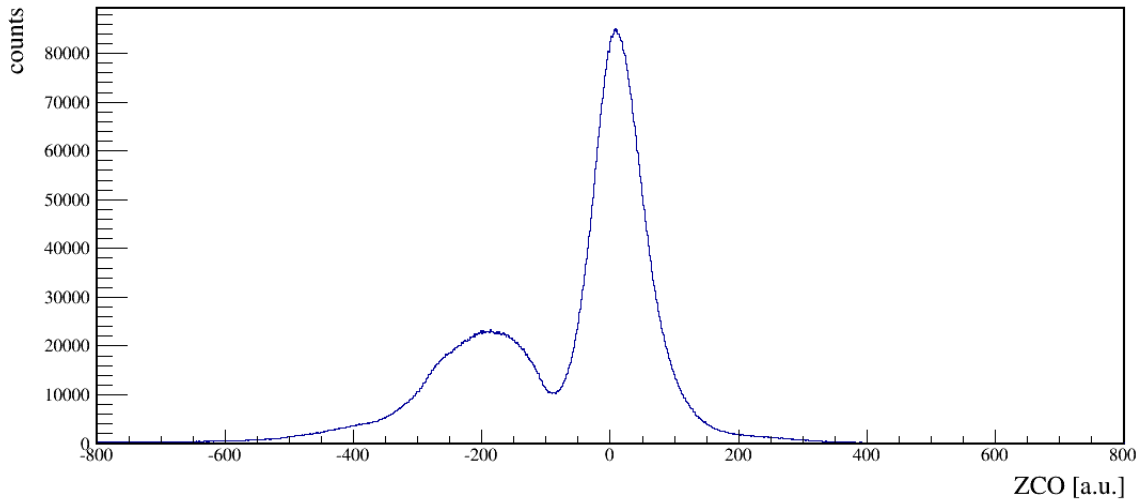


Figure 2.7: Zero Cross Over spectrum of NW detector number 4. The two peaks visible are the ZCO of neutrons on the left and the ZCO of the γ on the right. Note the higher intensity associated with γ events and that the left tail of γ peak could inevitably included in a neutron gate in this first analysis. In the off-line management we could better discriminate neutrons from γ thanks to the ZCO-TOF coincidence matrix (explained in Section 3.5.1)

Neutron scattering

Ideally, an incoming neutron will interact and leave all its kinetic energy in one neutron detector. In practice, it is often possible that the neutron scatter from one detector to another. It is not easy to distinguish such an event from two separate incident neutrons depositing the energy in the two detectors. A possible approach is to discard the events when the firing detectors are the nearest ones. If the time difference between two neutron signals, in the same event, is larger than a predetermined value, one can assume that the two signals are indeed coming from a scattered neutron. The

value is predetermined by measuring the average TOF between each pair of detectors in NW. This is because the flight time for all neutrons emitted from the reaction in the target should be approximately the same.

However, also after the discrimination process described above, a large amount of scattered neutron events are identified as two neutrons. This fact is visible if we compare two spectra corresponding to channels including one neutron and two neutrons, eventually with an equal number of evaporated charged particles (see for example the $1\alpha 1n$ and the $1\alpha 2n$ spectra in Figure 4.12 in Chapter 4: the spectra are very similar).

The problem of neutron scattering strongly affects the performance of the Neutron Wall detector and in general the resolving power of the detection system. In particular, a further reduction of the array total efficiency occurs, since we reject all the events recognized as one-scattered neutron.

Chapter 3

Pre-sorting of the experimental data

In this Chapter we present the pre-sorting of the data for the subsequent analysis. The pre-sorting consist in the energy and the efficiency calibration of the GALILEO detectors, the kinematic Doppler correction of the γ -ray energies and the optimization of the time alignment for the events recorded by the EUCLIDES detectors. The selection of a reaction channel from the identification of light-charged particles and neutrons, in EUCLIDES and Neutron Wall respectively, is also presented. The last section is dedicated to describe the design of the EUCLIDES absorber, which is fundamental for our experiment as the channel of interest involves the detection of an α particle, that has to pass through the absorber.

For our experiment the accelerated ^{12}C beam is pulsed with a frequency of 2.5 MHz, i.e. a bunch of ^{12}C ions impinges on the target every 400 ns. Considering a fusion-evaporation reaction cross section of about 1 barn and a typical beam current of 5 pnA, at most one fusion reaction per bunch is expected to occur. An event is characterized by a set of energy and time informations of all the γ rays and the particles measured to be in coincidence in a specific time interval of about 400 ns.

The trigger for the acquisition system is a γ - γ detection in GALILEO in coincidence with a charged particle detected in EUCLIDES or/and a neutron detected in the Neutron Wall.

3.1 Energy calibration

Detector calibration allows to convert the ADC channels into the energy deposited in the detector. For this experiment, the GALILEO detectors were calibrated with the following sources: ^{22}Na , ^{54}Mn , ^{57}Co , ^{60}Co , ^{88}Y , ^{133}Ba , ^{137}Cs , ^{152}Eu and ^{241}Am . These are standard radioactive sources that are widely used in γ -ray spectroscopy to determine efficiencies and calibrate detectors. These sources cover, with their γ -ray energies, the region of interest for the experiment, that is below 4 MeV. The sources are placed separately in the center of the reaction chamber under running conditions.

A dedicated program, **RecalEnergy**, locates the characteristic peaks in the uncalibrated spectra and calculates centroid, area and FWHM, in units of channels, assuming that each peak in the spectrum follows a gaussian distribution.

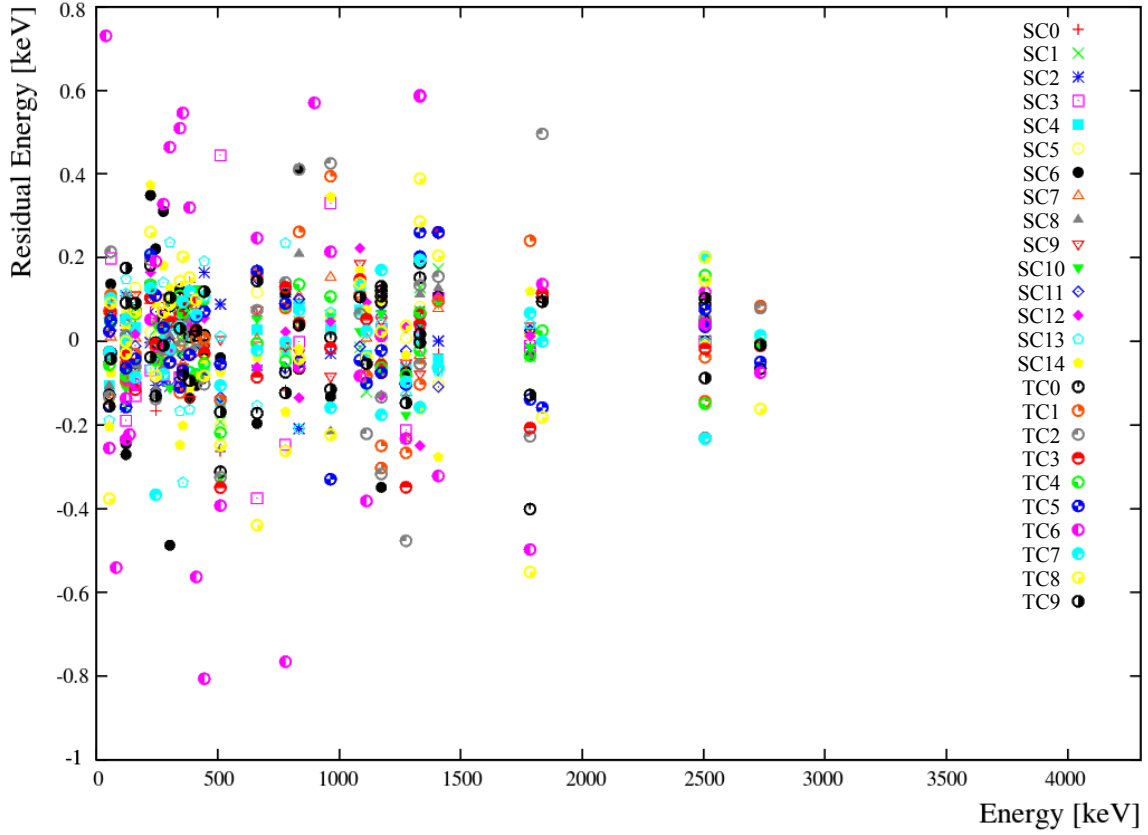


Figure 3.1: The graph shows for each detector the residuals $E_{calib} - E_\gamma$ between calibrated and tabulated energy for all the peaks used in the interpolation. On the average, the calibration is within ± 0.5 keV.

In our case, the energy calibration consists in the determination of a function, a fifth degree polynomial, describing the energy dependence from the channel number in the spectrum:

$$E_\gamma(ch) = A_0 + A_1 ch + A_2 ch^2 + A_3 ch^3 + A_4 ch^4, \quad (3.1.1)$$

where E_γ is the γ -ray energy and ch is the channel number in the spectrum corresponding to the centroid of the peak. The interpolation of the data (E_γ, ch) is performed individually for each GALILEO detector by the script **Calib**, based on the Marquaratz-Lievenberg minimization algorithm. The **Calib** script calculates coefficients of the interpolating polynomial, and provides, for each detector, a plot of all energy residues $E_{calib} - E_\gamma$, i.e. the difference between the energy obtained with the calibration and the tabulated energy. In Figure 3.1, except for a detector with problems (TC6), most of the residues lie within ± 0.8 keV at maximum. This calibration brings an error of about 0.5 keV, that is comparable with the intrinsic HPGe resolution.

3.2 Efficiency calibration

A γ -ray spectrometer has a detection efficiency which depends on the (detected) energy. In order to built up a level scheme, an efficiency calibration is needed. A HPGe γ -ray detector is most efficient in the range of 200-300 keV while its detection efficiency falls exponentially at higher energy, where the incoming γ ray may partially deposit its energy by escaping from the detector.

For the efficiency calibration, five radioactive sources were used: ^{241}Am , ^{152}Eu , ^{133}Ba , ^{60}Co and ^{22}Na . They emit γ rays in the energy range of interest for the experiment.

When different radioactive source are used, a normalization factor is required. The absolute efficiency is defined as the number of photons detected divided by the total number of photons emitted from the source:

$$EFF(E_\gamma) = \frac{\text{Integral}(E_\gamma)}{BR(E_\gamma) \cdot \text{Activity} \cdot \Delta t}. \quad (3.2.1)$$

The number of detected photons corresponds to the area of the full-energy peak, $\text{Integral}(E_\gamma)$, in the spectrum. The fit of the energy peaks was performed with the same program used to calibrate the crystals. The total number of photons emitted from the source during the acquisition, for a specific time Δt , depends on the source activity and on the relative intensity of the E_γ transition, branching ratio $BR(E_\gamma)$. The activity values adopted for each source are those relative to the time of the experiment, May 2016.

The efficiency calibration is performed for each GALILEO detector and then a total efficiency is obtained by summing for every γ -ray transition values. A dedicated program reads the list of gaussian fits, obtained for the main energy peaks in each γ -ray spectrum, and calculates efficiencies and errors. The error associated to each area is the statistical one, that is $\sqrt{\text{Integral}(E_\gamma)}$.

An alternative way to normalize the intensity of the peaks in each source spectrum, is to divide their areas by the area of the 1460-keV peak of ^{40}K . This isotope is a primordial radionuclide that is present in the environmental background. Its constant presence in each spectra provides an information proportional to the time that the detector is exposed to a specific radioactive source. Thus, it is possible to calculate a relative efficiency by the following expression:

$$EFF(E_\gamma) = \frac{\text{Integral}(E_\gamma)}{BR(E_\gamma) \cdot \text{Integral}({}^{40}\text{K})}, \quad (3.2.2)$$

where $\text{Integral}({}^{40}\text{K})$ is the area of the 1460 keV peak of ^{40}K .

The program provides the parameters of the interpolating function efficiency *vs* energy. Once obtained the function $EFF = f(E_\gamma)$, one can calculate the right peak intensities.

The interpolating function is the fourth degree polynomial:

$$f(x) = p_0 + p_1 \ln(x) + p_2 \ln^2(x) + p_3 \ln^3(x) + p_4 \ln^4(x). \quad (3.2.3)$$

The efficiency plot is shown in Figure 3.2.

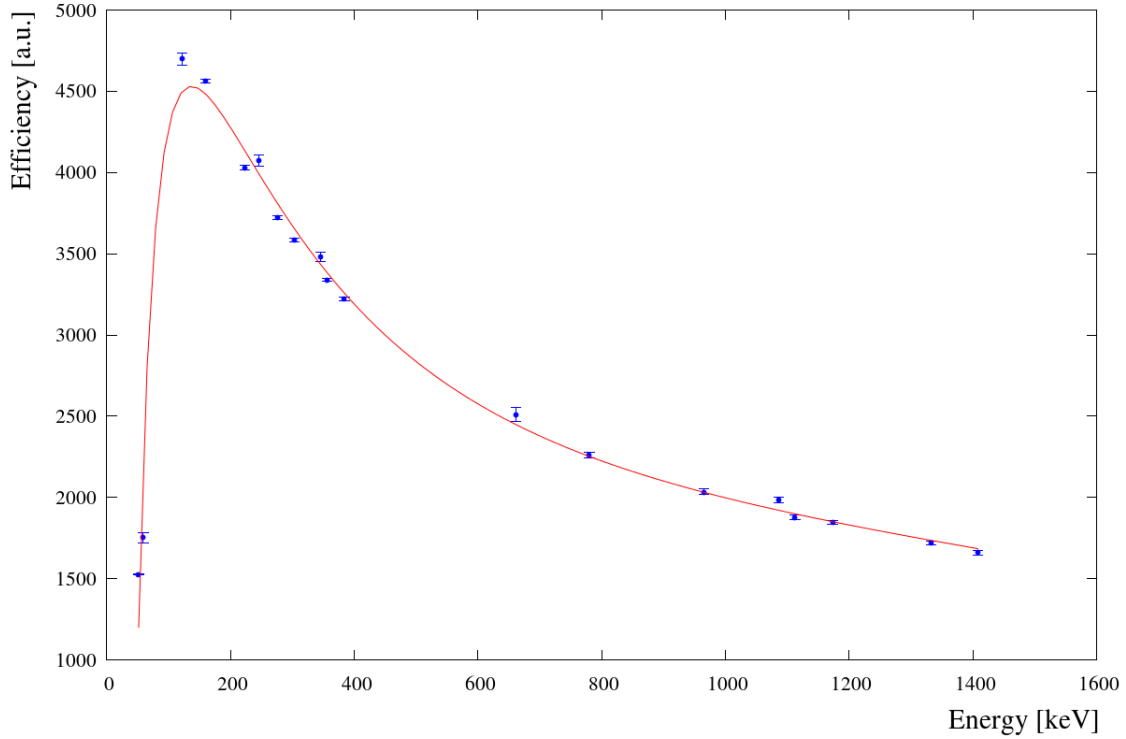


Figure 3.2: The efficiency curve obtained for the SC2 GALILEO detector. The x axis indicates the γ -ray energy and the y axis the relative detection efficiency. The polynomial interpolating function is shown in equation 3.2.3.

3.3 Average and kinematic Doppler correction

γ rays emitted from a nucleus in motion with a velocity β and a direction that forms an angle θ with the detector detecting the γ ray (see Figure 3.3), experience a Doppler effect. The Doppler effect shifts the γ -ray energy, E_γ , from its value E_0 , i.e. the energy corresponding to the γ ray emitted in a system of reference at rest, to the energy in the laboratory frame of reference where the nucleus moves with velocity $\vec{\beta}$:

$$E_\gamma = E_0 \frac{\sqrt{1 - \beta^2}}{1 - \beta \cos \theta}. \quad (3.3.1)$$

For low-energy nuclear physics, typical velocities for the evaporation residues are $\beta \sim 0.014 \div 0.017$, so the above relation can be approximated by considering $\beta^2 \sim 0$:

$$E_0 \simeq E_\gamma (1 + \beta \cos \theta). \quad (3.3.2)$$

For an average Doppler correction we assume that the residual nuclei proceed forward along the z axis, that coincides with the beam optical axis.

The Doppler shift depends on the angle θ of the detector where the γ -ray is interacting. GALILEO detectors are placed backward, so $180^\circ < \theta \leq 90^\circ$ and $-1 < \cos \theta \leq 0$. As a result, in the spectra the peaks are broadened and shifted to the left, at lower energies. From Eq. 3.3.2 we have that γ ray detected at 90° will only experience the Doppler broadening and not the Doppler shift.

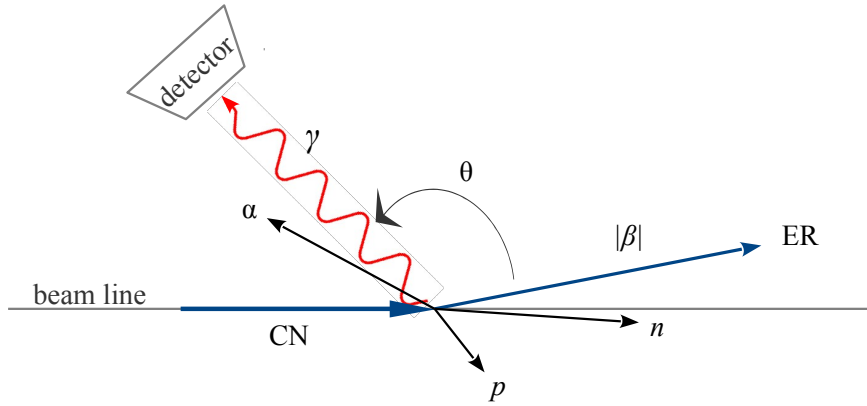


Figure 3.3: Sketch of the reaction kinematics. After having evaporated a particle, the compound nucleus (CN) ^{66}Ge , now an evaporation residue (ER), can emit γ rays in a certain direction that forms an angle θ with the ER. The CN is supposed to have the same direction as the beam.

The detector angle θ is defined by the line connecting the target position to the center of the detector and the velocity vector of the residue, assuming the evaporation at the center of the target. To determine the velocity vector $\vec{\beta}$ of the emitting source (ER), two ways are possible:

- use an *average* value of β , i.e. the mean value of each evaporation residues, along the beam axis,
- use a full *kinematic* reconstruction, event-by-event, to extrapolate a more accurate value of β for a single ER.

For the full kinematic correction, the reconstruction of β is obtained by profiting of the presence of a charged particle detector (EUCLIDES) and a neutron detector (NW). We can reconstruct the kinematics of the event and calculate the momentum of the residual nuclei \vec{p}_{ER} through the momentum conservation law:

$$\vec{p}_{ER} = \vec{p}_{CN} - \sum_i \vec{p}_i,$$

where \vec{p}_i are the momentum of the evaporated particles. The mean velocity of the compound nucleus is used as an input parameter while its direction is assumed to be along the beam direction.

As verified in previous specific experiments [23, 28], Doppler correction can be performed with superior quality with kinematic reconstruction rather than the standard Doppler correction based on the average velocity value. This is confirmed by our results. In particular, for the 2α channel ($^{66}\text{Ge} \rightarrow 2\alpha + ^{58}\text{Ni}$), it is evident that the average Doppler correction does not work as well as the kinematic one. In Figure 3.4 the kinematically corrected spectrum is shown in blue and the average corrected spectrum in red for the 2α channel in the energy range between 900 keV and 1500 keV. A double peak structure in the average Doppler corrected spectrum of ^{58}Ni emerges, especially for the transitions at 1004.8 keV and 1454.3 keV. The average-corrected peak is overlapped to the peak

obtained by a kinematic correction, that also corresponds to the energy detected by the 90° GALILEO detectors. In fact, from the equation 3.3.2, it results that no energy shift is present for $\theta = 0$. The rightmost peak corresponds to the energy detected by the backward GALILEO detectors. In fact, the velocity of ^{58}Ni is lower than the velocity used in the average Doppler correction; therefore, the E_0 calculated by Equation 3.3.1 has an absolute value higher than the kinematic corrected energy.

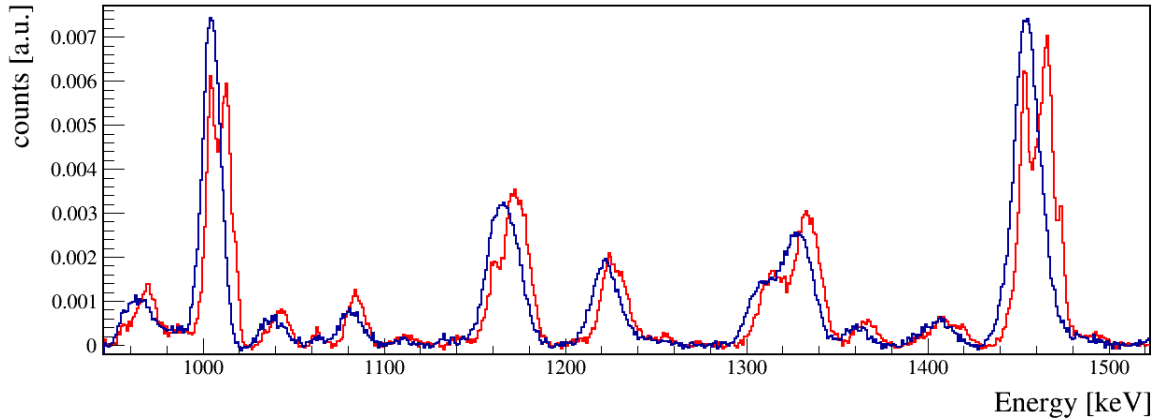


Figure 3.4: Zoom of the 2α channel-spectrum ($^{66}\text{Ge} \rightarrow 2\alpha + ^{58}\text{Ni}$). The $4^+ \rightarrow 2^+$ and the $2^+ \rightarrow 0^+$ transitions, at 1004.8 keV and 1454.3 keV respectively, are clearly visible. The blue, the kinematic reconstruction Doppler correction, in red, the average Doppler correction.

The velocity of the compound nucleus used to perform the kinematic reconstruction is obtained by the minimization of the FWHM of the ^{60}Ni peak at 1173.2 keV. In Figure 3.5 we plot the kinematic Doppler corrected γ -ray energies for the $\alpha 2p$ channel ($^{66}\text{Ge} \rightarrow \alpha + 2p + ^{60}\text{Ni}$) as a function of the different values of the CN velocities (input β on y -axis). The minimum value of FWHM is achieved for $\beta = 0.0142$.

The energy resolution of GALILEO, ΔE_γ^{final} , is often much worse than the intrinsic one, ~ 2 keV at 1332 keV. In fact, to the intrinsic resolution of the detector ΔE_γ^{int} , which includes contributions from the detector itself and the electronics used to process the signal, we must add the Doppler broadening of the peaks, due to the presence of unavoidable errors in the measurement of θ and β (Equation 3.3.1). The fact that a single HPGe crystal of GALILEO array has a nonzero opening angle implies that a γ ray is detected with a geometrical angular uncertainty $\Delta\theta$. This leads to a contribution of ΔE_γ^θ to the total resolution. Furthermore, the determination of the recoil velocity has an uncertainty $\Delta\beta$ owing to the velocity variation of the recoils across the target ΔE_γ^{vel} and to the assumption (during the kinematic reconstruction) that the velocity of the compound nucleus is along the beam direction ΔE_γ^{dir} .

The combination of these factors, added quadratically, gives the final energy resolution:

$$(\Delta E_\gamma^{final})^2 = (\Delta E_\gamma^{int})^2 + (\Delta E_\gamma^\theta)^2 + (\Delta E_\gamma^{vel})^2 + (\Delta E_\gamma^{dir})^2. \quad (3.3.3)$$

For the 1332 keV transition of ^{60}Ni , populated in beam during our experiment, ΔE_γ^{final} is ~ 13 keV.

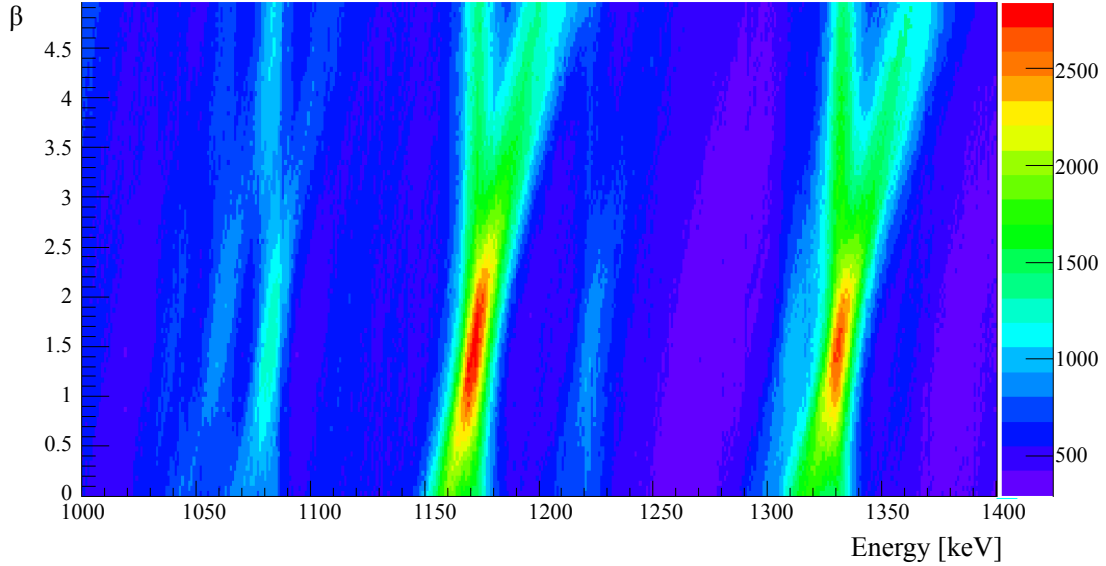


Figure 3.5: Matrix of the β values, as a function of the γ -ray energy, for the $\alpha 2p$ -channel. For the correct values of β , the γ -ray energy energies correspond to the energies detected at 90° by detectors (region around $0.014 \div 0.015$). For different values of β the separation between the 90° and the rest of the detector is visible.

3.4 Time alignment

The compound nucleus, ^{66}Ge , populated in the fusion-evaporation reaction $^{12}\text{C} + ^{54}\text{Fe}$, immediately evaporates some particles, has discussed previously. The time difference (Δt) between two hits in the same event is of the order of the EUCLIDES time resolution, about 5 ns.

A particle that hits one EUCLIDES detector produces a signal with a typical waveform whose height is of few hundred mV and rise time is of few hundred ns. If the signal exceeds a preset threshold, the acquisition system records the signal. The time when the signal exceeds the threshold trigger time is defined by the TimeStamp distributed by the GTS (Global Trigger and Synchronization) and this is an absolute time. The digitizers sample the trace with a frequency of 100 MHz (a point every 10 ns) and therefore the TimeStamp has a time resolution of 10 ns. The acquisition system saves 100 samples for each triggered waveform, corresponding to 1 μs : 500 ns before the trigger time and 500 ns after. Time is measured again from this saved trace with a higher precision, by using a linear interpolation between the baseline and the rising slope of the signal. We call TimeSecond the new time information. TimeSecond is the off-line time of the particle hitting the first thin layer of EUCLIDES (ΔE), while TimeFirst is the time of the particle hitting the second layer of EUCLIDES (E).

Therefore, the time of a signal consists in the sum of the TimeStamp (TS) and the TimeSecond (TT):

$$t = TS + TT.$$

Each trigger channel has to be synchronized with all the others. This means that signals of each detectors in the same event must be triggered at the same time, i.e.,

once defined a short time interval Δt (depending on the time resolution), the difference between each signal must be less than Δt .

Considering the two EUCLIDES detectors mentioned in Figure 3.6, it is evident that the time difference is shifted by few tens of ns from zero before alignment process (dash line in Figure 3.6).

A good synchronization implies a time-difference peak centered around zero. This is, practically, not always achieved and to align the time signals, we adopt the following procedure.

We check the spectra for any pair of EUCLIDES detectors and calculate the centroid of the time difference peak. The time-shift corrections of each detector is determined by a dedicated program, **solveTT**. The program calculates corrections for the time parameter of a set of detectors by minimizing the dispersion of their relative time peaks $t_i - t_j$. The shifts are obtained by a χ^2 minimization of the distance between all pairs of Δt_{ij} and Δt_{ji} peaks. The Figure 3.6 show the obtained corrections for the two EUCLIDES detectors: the aligned time-difference peak is centered around zero (continue line in Figure 3.6).

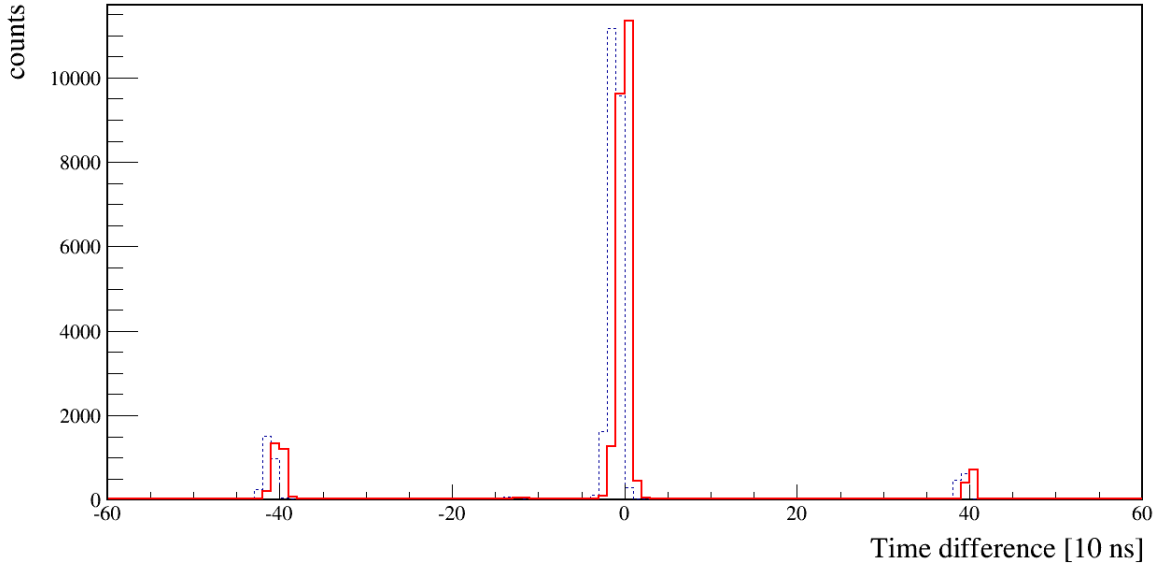


Figure 3.6: Aligned time difference between EUCLIDES detectors number 71 and 82 (continue line) in comparison with the time difference before the alignment (dash line).

In Figure 3.7 we plot in a single graph the time difference of every couple of detectors and on average we obtain a peak centered around zero. The time corrections leads to a narrower peak. In the figure two small peaks at about ± 400 ns, that correspond to the preceding and following beam bunches, are also visible.

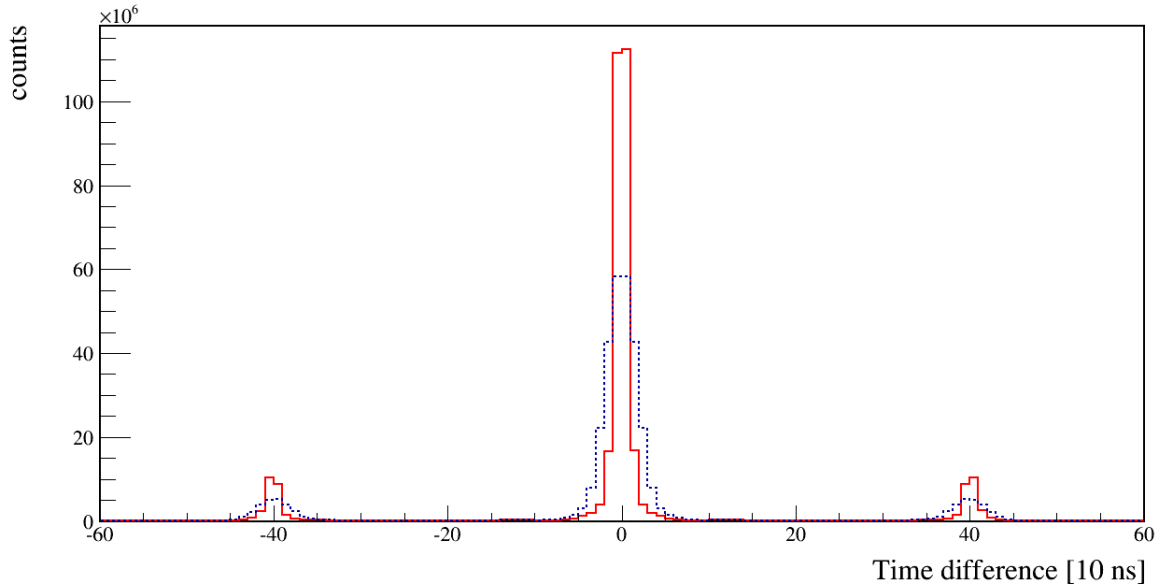


Figure 3.7: Aligned time difference between each pair of the EUCLIDES detectors (continue line). For comparison, the time difference before the alignment is also presented with a dashed line.

3.5 Particle selections

The EUCLIDES array and the Neutron Wall detect light charged particles and neutrons respectively. By selecting a combination of alpha particles, protons and neutrons, different reaction channels can be isolated.

3.5.1 Neutron- γ discrimination with the Neutron Wall

The Neutron Wall detects neutrons and, with a much higher efficiency, γ rays originated in the fusion-evaporation reaction. The ratio between the number of γ detected and the neutrons is of the order of 5. The neutron- γ discrimination is achieved by combining the zero-cross-over (ZCO) and the time-of-flight (TOF), measured with respect to a reference signal [29]. A typical TOF *vs* ZCO correlation matrix obtained from a NW detector is shown in Figure 3.8. In the ZCO-TOF matrix the more intense area in the middle corresponds to the γ rays, while the less intense blob, lower left, corresponds to neutrons. During the off-line analysis we selected the neutrons area in the correlation matrices for each NW detector.

3.5.2 Light-charged particle discrimination in EUCLIDES

Two-dimensional gates in the ΔE -E matrix, shown in Figure 3.9, were applied in order to select events corresponding to different light charged particles [23]. In this matrix different loci are visible and they correspond to the detection of $1p$, $1d$, $1t$, $2p$, 1α , $1\alpha 1p$ and 2α . The two curves with a different trend, visible just above the 1α and $1p$ loci, are an effect due to the segmentation of the detector. They correspond to particles entering the segmented telescope through the passivated area in between the segments.

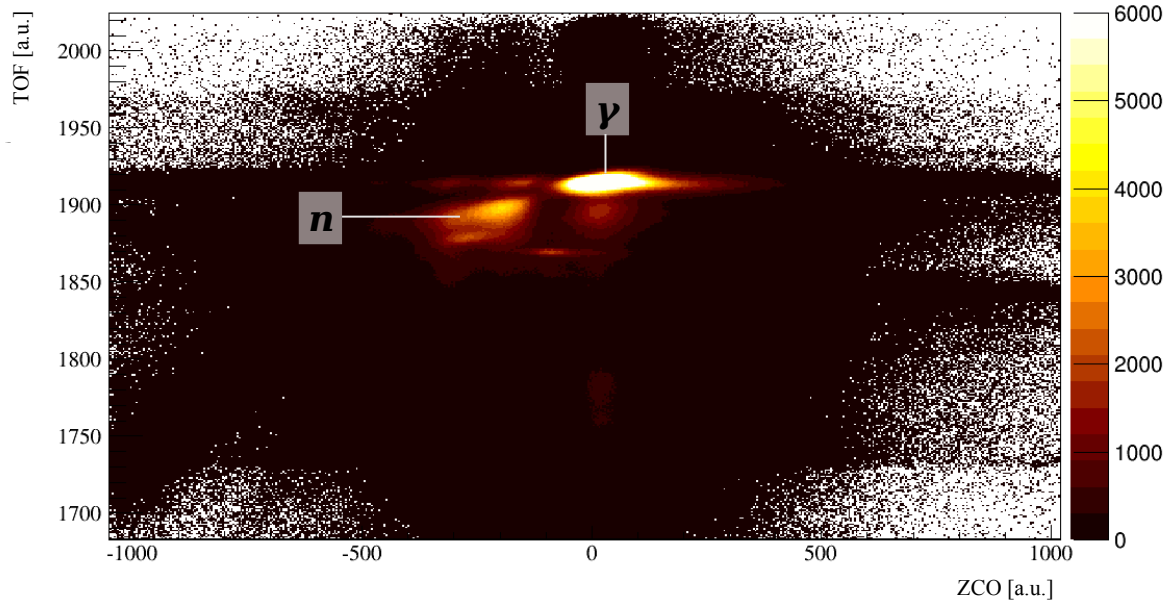


Figure 3.8: A typical TOF *vs* ZCO correlation matrix from NW detectors. The two locus of points corresponding to neutrons and γ -rays are indicated.

Here there is some charge collection due to the fringe electric field at the borders of the active area: this fringe field is strong enough in the ΔE detector to collect almost the whole deposited charge, while in the thicker E crystal a large fraction of the deposited charge is lost [30].

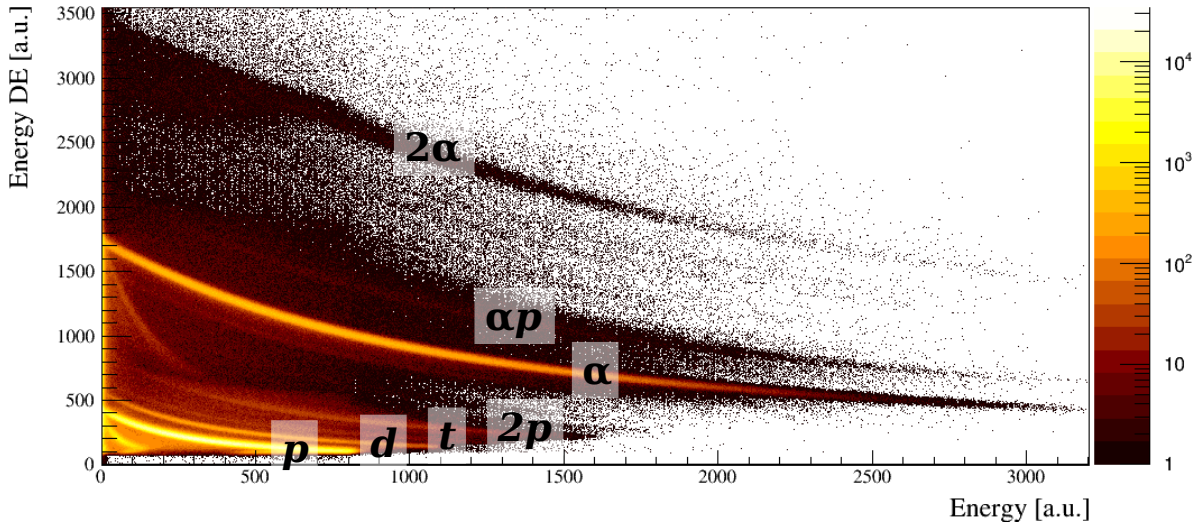


Figure 3.9: A $E vs \Delta E$ correlation matrix from one of the EUCLIDES telescopes at a forward angle. The different curves correspond to protons, deuterons, tritons and α particles.

The α -particle discrimination obtained by a cut in the EUCLIDES ΔE -E matrix, allows to select all those events corresponding to clean α particles detected in the E layer. Instead, α particles stopped in ΔE layer, have a wrong energy measurement due

to the large fraction of energy loss in the absorber, to respect of their total energy. In our case, the events stopped in the ΔE layer of the EUCLIDES array are the majority, about six times more than the remaining α particles reaching the E layer. During the analysis we treated them separately to have the chance to further compare the two classes of events and eventually sum them up.

The events selected by an alpha particle stopped in the ΔE layer have a kinematic reconstruction with a large error with respect to the events corresponding to a detection of an alpha in the E layer. In fact, the error in the measurement of the α energy leads to an error on the kinematic reconstruction of β .

The difference between events corresponding to alpha particles stopped in the ΔE and the E layer, respectively, are also visible if we compare the spectra corresponding to the $\alpha 2n$ channel with and without the events corresponding to stopped alpha in ΔE , as shown in Figure 3.10.

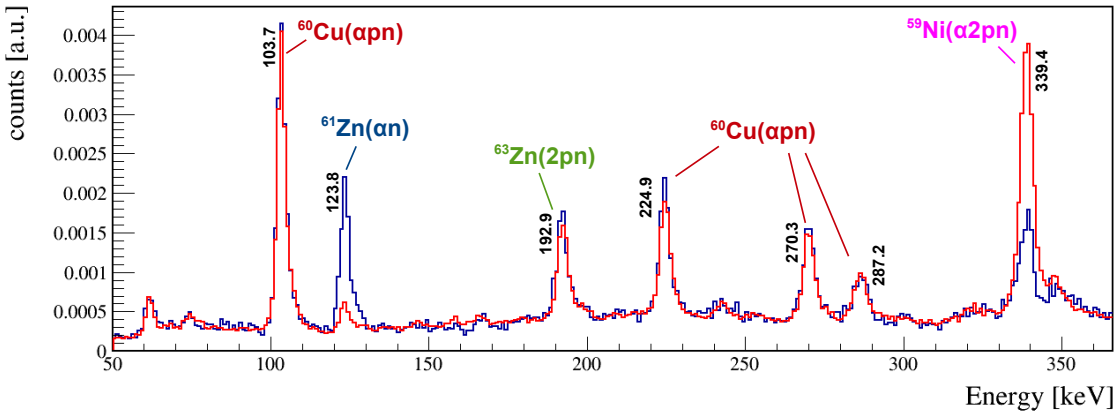


Figure 3.10: Comparison between the $\alpha 2n$ -channel spectrum with (red) and without (blue) the events corresponding to stopped α 's in ΔE layer. The main peaks in the spectrum are marked.

In the spectrum, we note the different intensity of the 339.4 keV transition of ^{59}Ni ($1\alpha 2p1n$) and 123.8 keV transition of ^{61}Zn ($1\alpha 1n$). To explain such behavior we have to consider how the events are selected in both cases. The α particles that pass through the ΔE layer and deposit the remaining energy in the E layer, are selected with a gate around the α “hyperbole” in Figure 3.9, avoiding the region around $\Delta E=0$. Instead, alpha particles stopped in the ΔE layer are selected with a 1D gate along the y axis from 400 keV to 1000 keV. With this condition it is possible that the selected particles are not only the α stopped but also two protons stopped in ΔE layer, which, at such lower energy have a range shorter than the thickness of the ΔE layer. Thus, in the α stopped in the ΔE spectrum the peak at 339.4 keV of ^{59}Ni that corresponds to the evaporation channel $1\alpha 2p1n$ is more evident than the peak at 123.8 keV of ^{61}Zn that corresponds to an evaporation channel with any evaporated proton. This effect is also visible for the 936.7-keV transition in ^{61}Zn .

EUCLIDES angles [°]	^{12}C energy [MeV]	Absorber thickness [μm]
148.28	27.0	25.0
121.72	31.2	30.3
116.57	32.4	31.7
90.00	39.7	41.9
63.43	48.6	56.1
58.28	50.4	59.2
39.38	56.4	69.8
25.90	59.5	76.1

Table 3.1: Thickness of the Al absorber foil needed, at different angles, to stop a ^{12}C scattered beam ion. The ^{12}C energy indicate the energy of the ^{12}C scattered beam ions at the corresponding polar angles.

3.6 The EUCLIDES absorber

As mentioned previously in Section 2.3.1, a layer of absorber is needed to stop the scattered beam of ^{12}C and to prevent the EUCLIDES detectors to be damaged.

The absorber is a 15-cm-long cylindrical foil of Al, usually prepared for each particular experiment. The calculations performed to adjust at best the thickness of the absorber are based on the beam-target reaction kinematics. Only Rutherford scattering is considered here, since other kinds of channels involve particles with lower energy and intensity.

With the LISE++ package we studied the kinematics of the elastic scattering $^{54}\text{Fe}(^{12}\text{C}, ^{12}\text{C})^{54}\text{Fe}$ to obtain the energy of scattered ^{12}C as a function of the polar angle of the EUCLIDES detectors, corresponding to the center of each detector (see Table 3.1), in the laboratory frame. Then, we calculated the thickness of aluminum absorber needed to completely stop a ^{12}C nucleus at these energies. For a ^{12}C beam at 63 MeV and a ^{54}Fe target of $0.7 \mu\text{g}/\text{cm}^2$ the results obtained are listed in Table 3.1.

The thinnest Al foil available is $12.5 \mu\text{m}$, so we can only choose multiples of such thickness. We have also to consider that the thickness of the absorber change as a function of the polar angle θ of the scattered ions, as shown in Figure 3.11. If a is the thickness of the layer, the effective layer crossed by an ion is:

$$x = \frac{a}{\sin \theta}. \quad (3.6.1)$$

As in the main channel of interest of our experiment an α particle is evaporated, together with two neutrons, we chose a layer as thin as possible to minimize the α -energy loss in the absorber. According to our calculations of the α -energy distribution, we expect to stop α particles with an energy lower than x MeV, that correspond to a fraction of $y\%$ of the total α particles emitted. In Table 3.2 the value of x and y are listed for each EUCLIDES detector and the final thickness of the absorber, that consists of $25 \mu\text{m}$ (two layers) for the backwards angles and $50 \mu\text{m}$ (four layers) for the forward angles.

EUCLIDES angles [°]	Layers	x [MeV]	y
148.28	2	8.5	77%
121.72	2	6.2	39%
116.57	2	6.0	24%
90.00	4	8.8	35%
63.43	4	9.5	21%
58.28	4	9.4	12%
39.38	4	11.7	15%
25.90	4	14.8	36%

Table 3.2: For each EUCLIDES detector angle we report: the numbers of layers of the absorber used, the energy of the α particles lost in the corresponding layer (x) and the fraction of α stopped by the absorber (y).

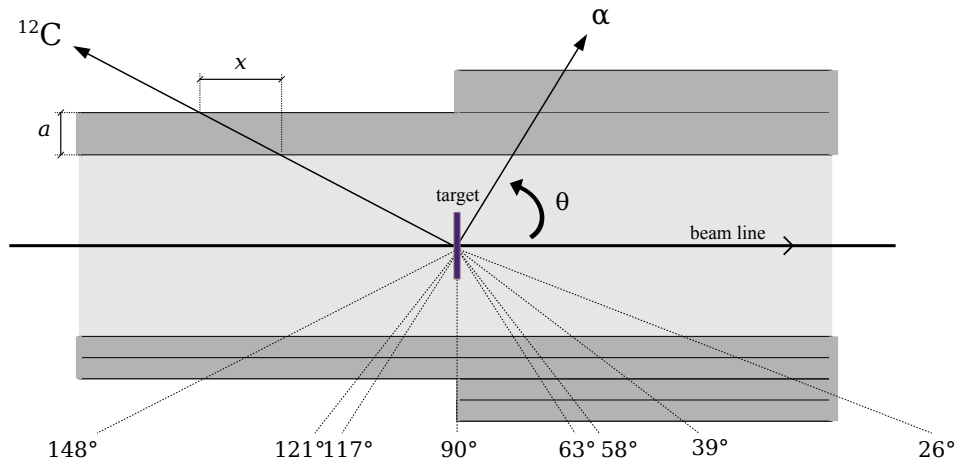


Figure 3.11: Longitudinal section of the EUCLIDES absorber. The angles of the detectors and the final layers chosen for the absorber are shown.

Chapter 4

Analysis of the experimental data

In a fusion-evaporation reaction the compound nucleus evaporates different combinations of light particles. Each combination corresponds to a specific reaction channel and therefore a specific final nucleus. Statistical calculations, performed by the PACE4 software code, provided the different reaction channels with their relative cross section. The results of such calculation are listed in Table 4.1. In Figure 4.1 the region of interest populated in our experiment is shown.

^{60}Ge	^{61}Ge	^{62}Ge	^{63}Ge	^{64}Ge $2n$	^{65}Ge n	^{66}Ge
^{59}Ga	^{60}Ga	^{61}Ga	^{62}Ga	^{63}Ga $p2n$	^{64}Ga pn	^{65}Ga p
^{58}Zn	^{59}Zn $a3n$	^{60}Zn $a2n$	^{61}Zn an	^{62}Zn a	^{63}Zn $2pn$	^{64}Zn $2p$
^{57}Cu	^{58}Cu $ap3n$	^{59}Cu $ap2n$	^{60}Cu apn	^{61}Cu ap	^{62}Cu $3pn$	^{63}Cu $3p$
^{56}Ni	^{57}Ni $2an$	^{58}Ni $2a$	^{59}Ni $a2pn$	^{60}Ni $a2p$	^{61}Ni $4pn$	^{62}Ni $4p$
^{55}Co	^{56}Co $2apn$	^{57}Co $2ap$	^{58}Co $a3pn$	^{59}Co $a3p$	^{60}Co	^{61}Co
^{54}Fe $3a$	^{55}Fe	^{56}Fe	^{57}Fe	^{58}Fe $a4p$	^{59}Fe	^{60}Fe

Figure 4.1: Part of the nuclide chart showing the region of interest for our reaction $^{12}\text{C} + ^{54}\text{Fe}$. The proton number and the neutron number are given on the y and x axis respectively. For some nuclei the reaction channel is reported in red. Top right is the compound nucleus $^{66}\text{Ge}^*$. Theoretical relative cross section of the nuclei identified in the experiment are reported in Table 4.1.

The evaporation of $1\alpha 2n$ from ^{66}Ge leads to the isotope ^{60}Zn . This nucleus has a quite low cross-section compared with the other nuclei produced in the reaction and, as a consequence, γ -rays de-exciting levels in this nucleus are not immediately visible in any γ -ray spectra, unless some conditions on the evaporated particles are applied.

A		Z	N	channel	x-section [mb]
65	Ga	31	34	1p	0.1
64	Ge	32	32	2n	2.9
64	Ga	31	33	1p1n	37.6
64	Zn	30	34	2p	28.7
63	Ga	31	32	1p2n	14.2
63	Zn	30	33	2p1n	175
63	Cu	29	34	3p	53.9
62	Zn	30	32	1 α	0.7
62	Cu	29	33	3p1n	1.6
61	Zn	30	31	1 α 1n	31.6
61	Cu	29	32	1 α 1p	114
60	Zn	30	30	1 α 2n	1.8
60	Cu	29	31	1 α 1p1n	145
60	Ni	28	32	1 α 2p	226
59	Ni	28	31	1 α 2p1n	1.7
58	Ni	28	30	2 α	85
57	Ni	28	29	2 α 1n	47.8
57	Co	27	30	2 α 1p	65.4
54	Fe	26	28	3 α	1.6

Table 4.1: List of most probable residual nuclei calculated with PACE4 software code for the reaction $^{12}\text{C} + ^{54}\text{Fe} \rightarrow ^{66}\text{Ge}$.

The cross section is estimated, by extrapolating the systematics of the measured cross sections in the mass region 60÷80, to be above 1 mb (see Figure 4.2). The calculated cross section is in the range 1 ÷ 10 mb. The lower value, 1 mb, is, however, 5 times larger than the value of about 200 μb for ^{68}Sn , reported in Ref. [13], and the value for ^{50}Fe reported in Ref. [31].

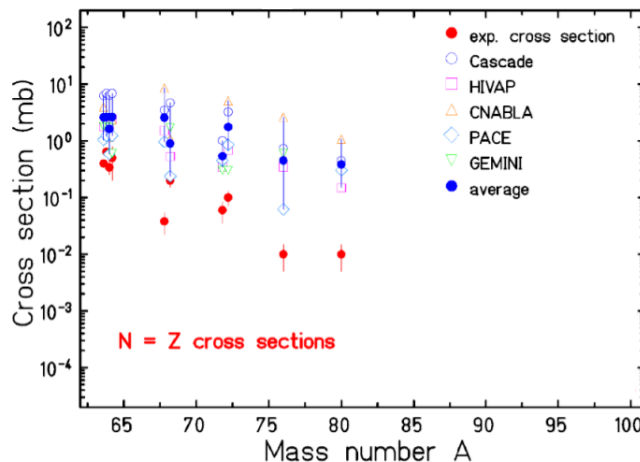


Figure 4.2: Measured cross section for evaporation residues in the mass region from mass 64 to 80 [32].

4.1 γ -ray energy spectra and matrix in coincidence with evaporated particles

4.1.1 1α , $1p$ and $1n$ gates

To verify the presence of a specific reaction channel, coincidences among the evaporated particles and γ -rays are, practically, often needed. First, we started to search for the most abundant species by exploring three different spectra, in coincidence with only one α , only one proton and only one neutron respectively. However, in each spectrum, we expect to observe those residual nuclei obtained from the evaporation of *at least* one α , *at least* one proton and *at least* one neutron respectively. In fact, due to the limited efficiency of EUCLIDES and the Neutron Wall, these spectra will be contaminated by other reaction channels, according to their cross section, if the other particles have not been detected. For instance, the ^{60}Ni γ -ray transitions are easily visible in the α spectrum, being the ^{60}Ni an $1\alpha 2p$ channel. protons of the ^{60}Ni reaction channel. Thus the acquisition system record ^{60}Ni like a 1α evaporating channel.

The main γ -ray peaks in the α , p , n spectra come from the following channels:

- α : $^{60}\text{Cu}(1\alpha 1p1n)$, $^{61}\text{Zn}(1\alpha 1n)$, $^{61}\text{Cu}(1\alpha 1p)$, $^{60}\text{Ni}(1\alpha 2p)$, $^{58}\text{Ni}(2\alpha)$, $^{57}\text{Co}(2\alpha 1p)$,
- n : $^{63}\text{Zn}(2p1n)$, $^{60}\text{Cu}(1\alpha 1p1n)$, $^{59}\text{Ni}(1\alpha 2p1n)$, $^{62}\text{Cu}(3p1n)$,
- p : $^{63}\text{Zn}(2p1n)$, $^{60}\text{Cu}(1\alpha 1p1n)$, $^{63}\text{Cu}(3p)$, $^{62}\text{Cu}(3p1n)$, $^{59}\text{Ni}(1\alpha 2p1n)$, $^{60}\text{Ni}(1\alpha 2p)$, $^{57}\text{Co}(2\alpha 1p)$.

The spectra in coincidence with 1α , $1p$ and $1n$ are shown in Figure 4.3, Figure 4.4 and Figure 4.5, respectively.

To identify a particular peak in one of these spectra, we put a gate of 5-10 keV around the chosen energy in the corresponding γ - γ coincidence matrix. A dedicated description of a γ - γ coincidences matrix will be given in Section 4.1.2. In the resulting spectrum, only the γ -rays in coincidence with the one gated are present and most of the peaks correspond to those of a specific known nucleus. However, peaks belonging to other nuclei are always present, due to the consistent background resulting in random coincidences with the one selected.

The main energy peaks that are visible in the spectrum of Figure 4.3 belong to $^{60}\text{Cu}(1\alpha 1p1n)$, $^{60}\text{Ni}(1\alpha 2p)$ and $^{57}\text{Co}(2\alpha 1p)$. γ -ray peaks from $^{61}\text{Zn}(1\alpha 1n)$, $^{61}\text{Cu}(1\alpha 1p)$ and $^{58}\text{Ni}(2\alpha)$ are also present.

In Figure 4.4 transitions belonging to many nuclei, in coincidence with at least one proton, are visible. The most important are those of ^{63}Zn ($2p1n$), ^{62}Cu ($3p1n$) and ^{60}Ni ($1\alpha 2p$).

The γ -energy spectrum gated on $1n$, see Figure 4.5, confirms the presence of the ^{63}Zn ($2p1n$), ^{60}Cu ($1\alpha 1p1n$) and ^{62}Cu ($3p1n$) isotopes.

A contaminating channel that is often present as background is ^{63}Zn ($2p1n$). Its most intense γ -ray transitions, from a projection in the range [190,197] keV, from the γ - γ matrix gated on $1p$, are presented in Figure 4.6.

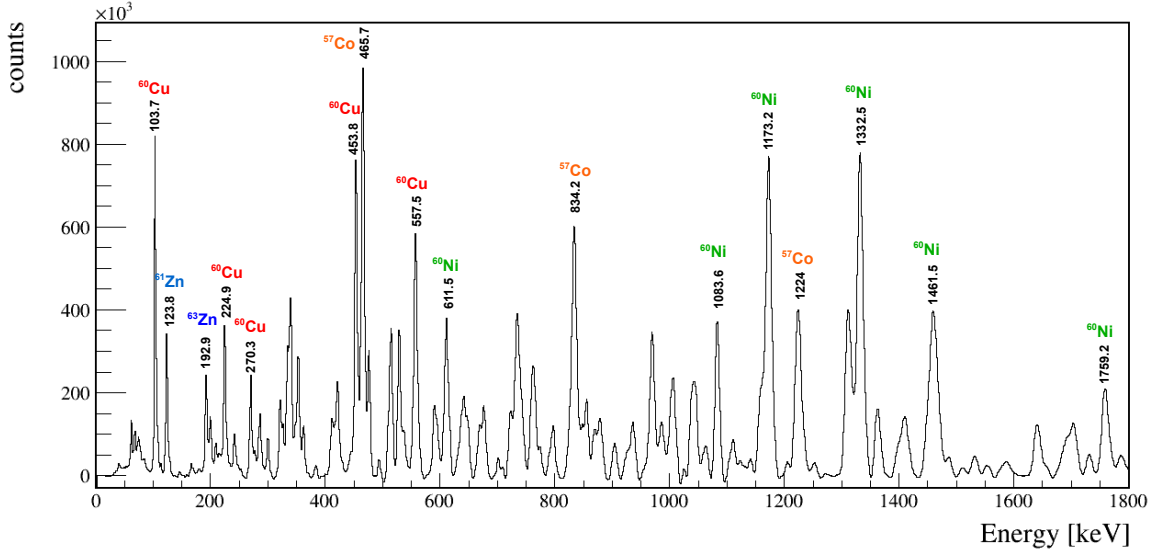


Figure 4.3: γ -ray energy spectrum gated on 1α . Main peaks have been identified and tagged.

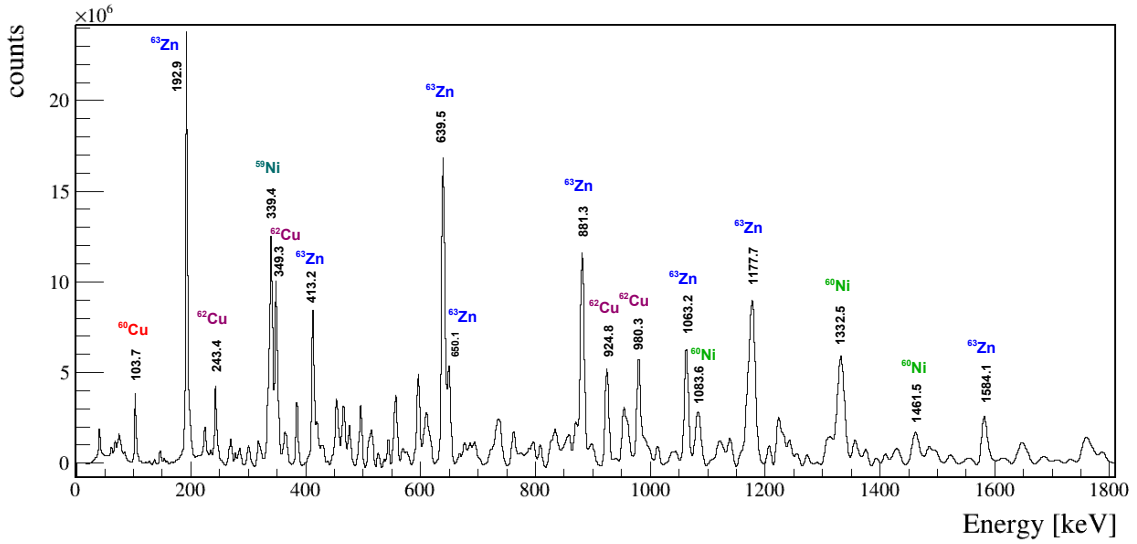


Figure 4.4: γ -ray energy spectrum gated on $1p$. Main peaks have been identified and tagged.

4.1.2 γ - γ coincidence matrix

Beside coincidences with the evaporated particles, a well established technique to analyze, in a selective manner, data from a γ -ray spectrometer is the use of a γ - γ coincidence matrix. Two γ rays are said to be in coincidence if they are detected within a difference in time that is of the order of the intrinsic time resolution of the detector. Such events are placed in a γ - γ coincidence matrix. For example γ rays from ^{61}Zn with energies of 123.8 keV, 872.7 keV and 1403.4 keV are detected simultaneously, i.e., the energy transition of 123.8 keV is in coincidence with the 872.7 keV and the 1403.4 keV transitions. A γ - γ coincidence matrix allows to identify whether a certain peak belongs to a nucleus and, varying the energy range of the gate, organize all the γ transitions into a level scheme with well defined de-excitation paths.

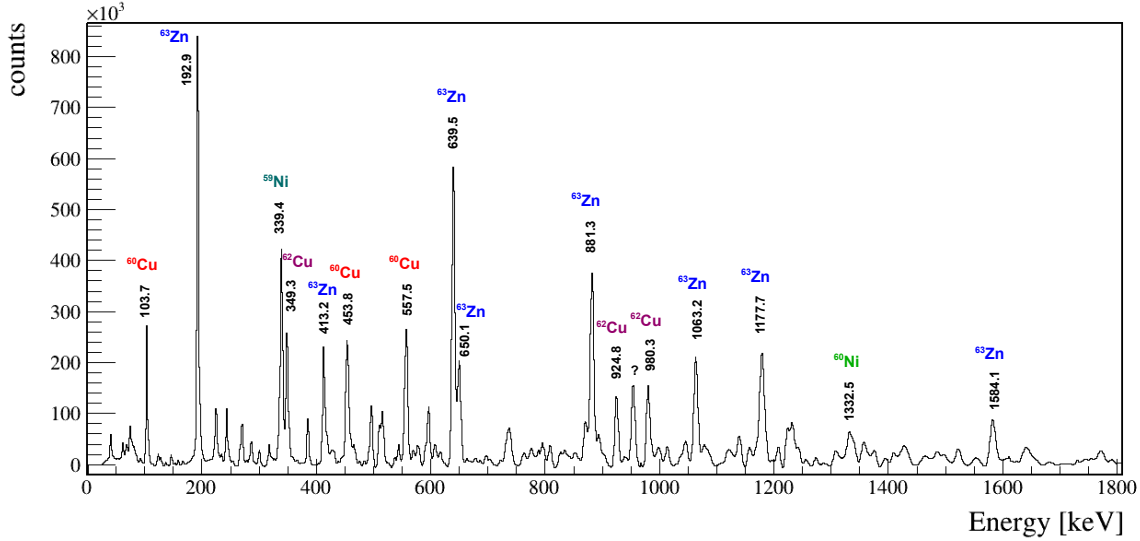


Figure 4.5: γ spectrum gated on 1 neutron with the identification of the principal peaks.

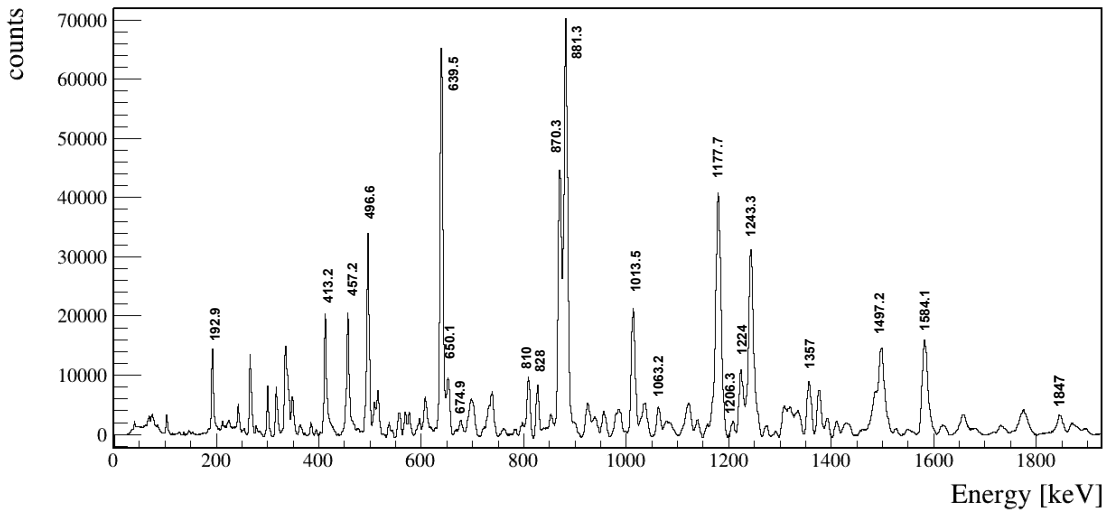


Figure 4.6: Projection on the interval [190,195] keV from the $\gamma\gamma$ coincidence matrix gated on 1p.

In Figure 4.7 a $\gamma\gamma$ coincidence matrix in coincidence with 1α is presented. The accumulation of points in correspondence of the most intense γ -ray transitions is evident.

In order to emphasize the capability of a $\gamma\gamma$ coincidence matrix to identify a de-excitation path belonging to a specific nucleus, we present two spectra of ^{63}Zn , gated from the 1n-channel $\gamma\gamma$ matrix on different energies: 192.2 keV and 413.2 keV (see Figure 4.8). It is evident that certain peaks are present or disappear and this reflects the different path of de-excitation towards the ground state. In the top panel of Figure 4.8, the projection in the range [190,197] keV shows all the energy transitions in coincidence with the 192.9-keV transition de-exciting the $5/2^-$ to the $3/2^-$ ground state. In the bottom panel of Figure 4.8, the projection in the range [410,417] keV shows the transitions in coincidence with the $7/2^- \rightarrow 5/2^-$, 413.2-keV transition. Different peaks emerge in a spectrum rather than in the other (they are marked with a red number). Note, in

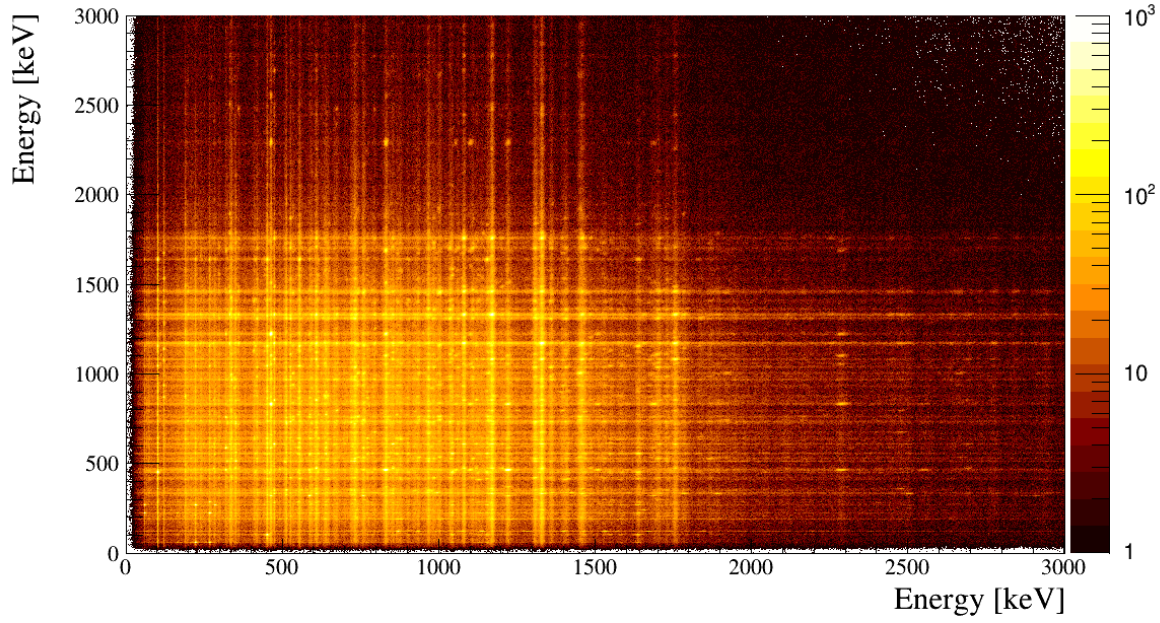


Figure 4.7: $\gamma\text{-}\gamma$ coincidence matrix gated on $1\ \alpha$. The accumulation of points in correspondence of the main γ -ray energy transitions are evident.

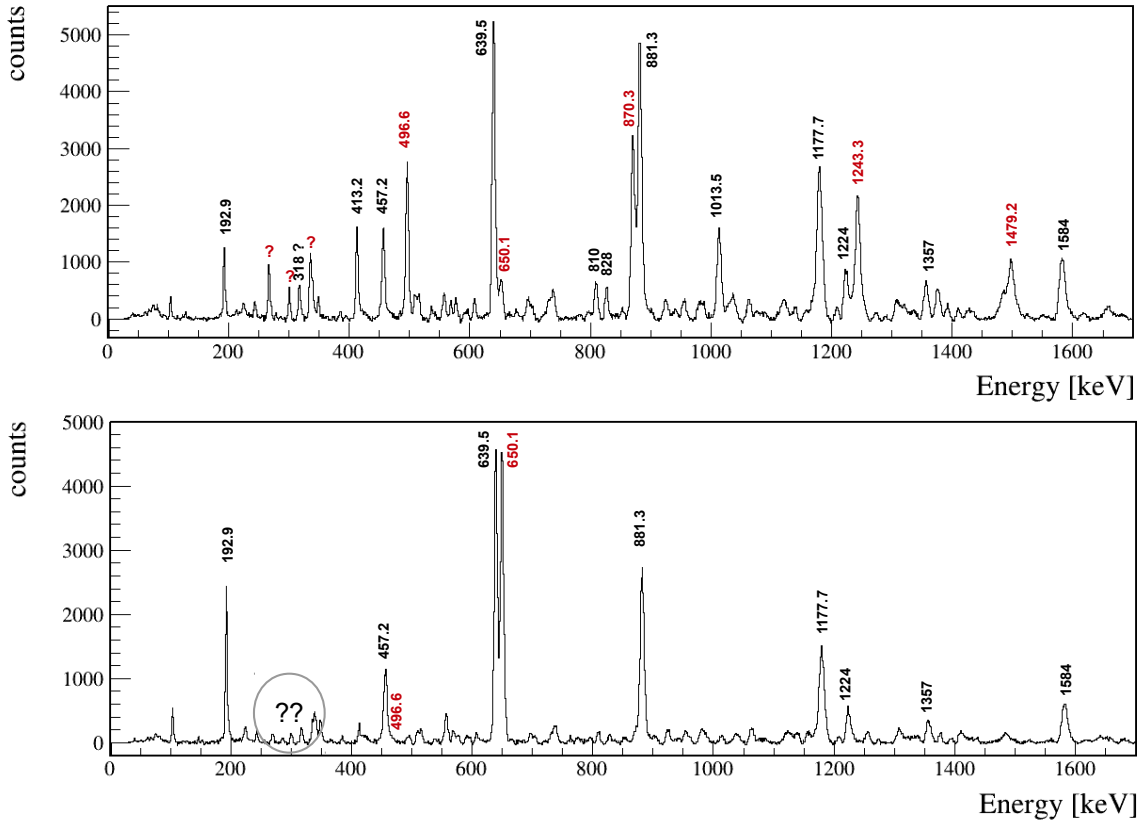


Figure 4.8: Comparison between two projections, from the $1n$ -channel $\gamma\text{-}\gamma$ matrix, resulting from two different gates on transitions of ^{63}Zn . See text for details.

particular, in the second spectrum, the much higher intensity of the peak at 650.1 keV. This transition de-excites the $5/2^-$ (650.1 keV) level directly to the ground state, and therefore it is not in coincidence with the 192.92-keV, $5/2^- \rightarrow 3/2^-$, transition. In the upper spectrum, the transition at 650.1 keV is at the level of the background.

The γ - γ coincidence technique is an extremely powerful tool to select specific transitions and reflects the resolving power of the γ -ray spectrometer. This will be of the utmost importance for the selection of the weak transitions belonging to ^{60}Zn .

However, when the background is dominant, as it is in the case of ^{60}Zn channel, its subtraction becomes an extremely delicate operation, as we will discuss in Section 4.2.1.

4.2 Search for new transitions in ^{60}Zn

The aim of the present experiment is to search for a new side band in ^{60}Zn . This side band is expected from some indications in the literature [14, 16, 33], as well as by dedicated calculations that we performed and that will be presented in Chapter 5.

Before searching for the existence of a possible side band, we have verified the presence of the main yrast transitions of ^{60}Zn in our dataset. The known level scheme of ^{60}Zn is reported in Figure 4.9, from Ref. [34]. We have used different methods to confirm the presence of these transitions.

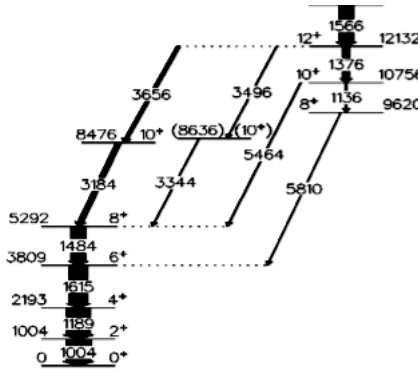


Figure 4.9: The ground state band of ^{60}Zn . A super-deformed (SD) band, taken from Ref. [34], is feeding the low-lying ground state band and begins at $J^\pi = 8_2^+$.

The GALILEO-EUCLIDES-NW combination allows to produce the γ spectrum in coincidence with $1\alpha 2n$, corresponding to ^{60}Zn . In that spectrum, shown in Figure 4.10, there are indications of the $2^+ \rightarrow 0^+$ and $4^+ \rightarrow 2^+$ transitions of the low-lying yrast band, but they appear just above the background. Instead, there are no indication of the 1615-keV and 1484-keV transitions. A significant problem in this spectrum is the huge presence of a background that prevents to identify these peaks.

The identification of the 1004-keV and 1189-keV γ -ray transitions in the $1\alpha 2n$ spectrum is supported when comparing the spectra from different channels, namely the $1\alpha 2n$, $1\alpha 1n$, 1α , 2α and the $1n$ spectrum. In Figure 4.11 such comparison is presented in the range between 900 keV and 1700 keV, to include the transitions of the ground state band of ^{60}Zn . There, the presence of ^{58}Ni , the 2α -channel, with the $4^+ \rightarrow 2^+$ 1004-keV transition is clear. The presence of this transition is a problem because it has

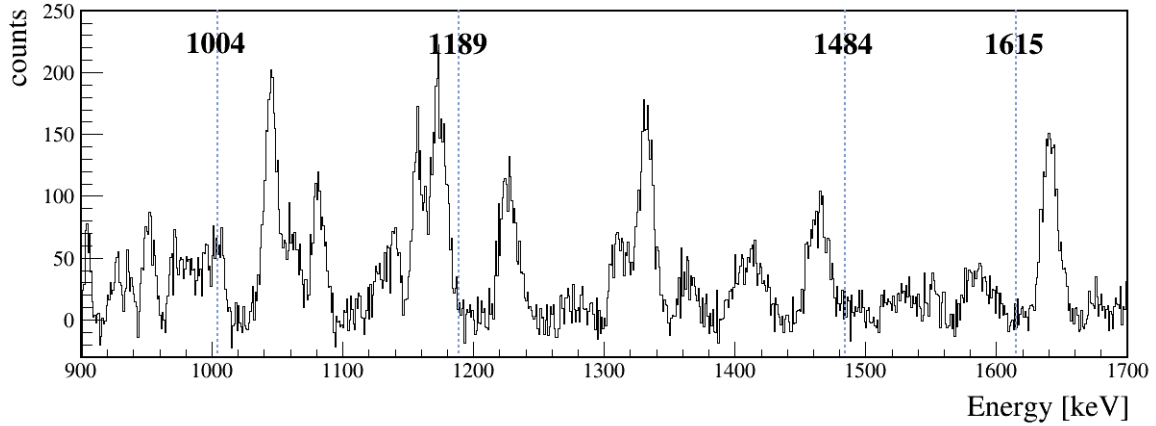


Figure 4.10: γ -ray energy spectrum, gated on $1\alpha 2n$, zoomed around the energies of interest, that are marked with dashed lines.

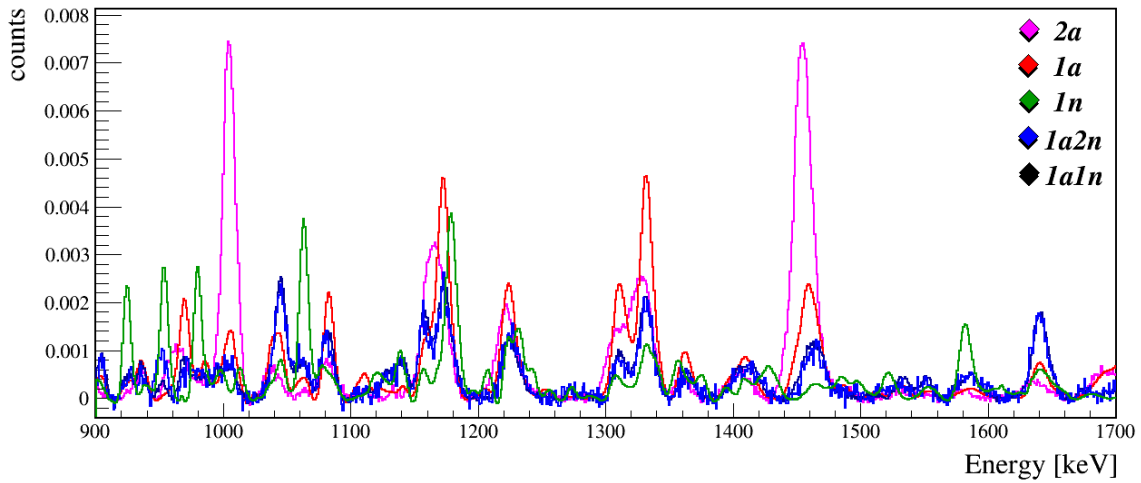


Figure 4.11: Comparison between the following five spectra (normalized): 2α (pink), 1α (red), $1n$ (green), $1\alpha 1n$ (black) and $1\alpha 2n$ (blue). Energy range between 900 keV and 1700 keV. Note the high intensity of the peaks at 1004 keV and 1454 keV of ^{58}Ni in the 2α spectrum with respect of the other spectra.

the same energy of the $2^+ \rightarrow 0^+$ 1004-keV transitions in ^{60}Zn . However we see that the γ -ray peaks of the 2α channel vanish when we apply a neutron condition, at the expense of statistics.

The Neutron Wall has an efficiency of about 26% for the detection of one neutron and of less than 3% for two neutrons. The statistics of the $1\alpha 2n$ spectrum is therefore very limited and significantly lower with respect the $1\alpha 1n$ spectrum. Furthermore, due to the problem of the scattering in the NW discussed in Section 2.3.2, in the $1\alpha 2n$ spectrum we observed nuclei, which evaporated only one neutron that scattered in the NW detectors, and therefore identified as a two-neutron event. Eventually, the $1\alpha 1n$ and $1\alpha 2n$ spectra are very similar, once scaled for their statistics, as shown in Figure 4.12. Of course, it is more convenient, for its larger statistics, to analyze the $1\alpha 1n$ spectrum which also contains ^{60}Zn .

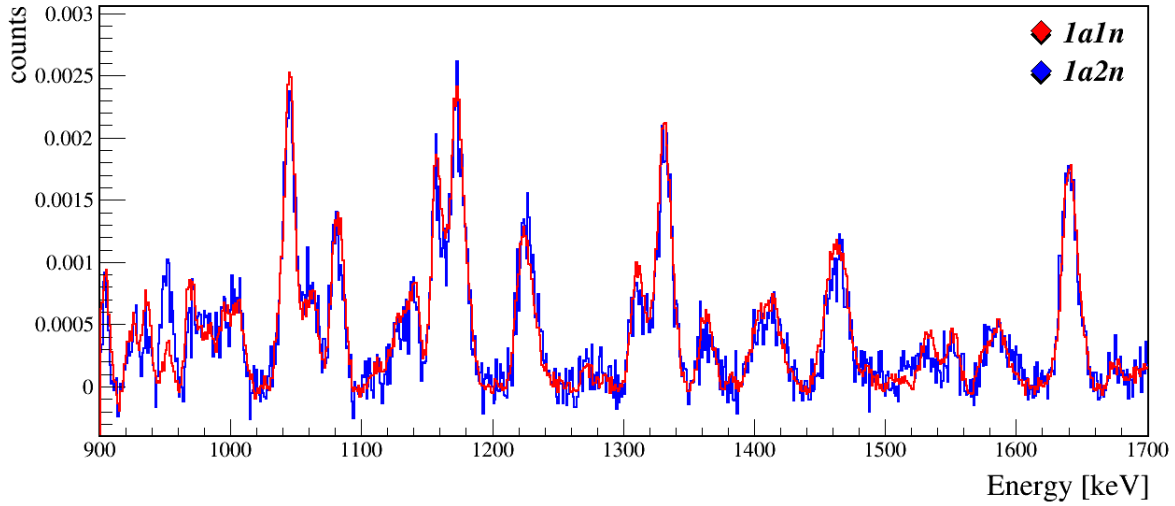


Figure 4.12: Comparison between the spectrum with $1\alpha 2n$ condition (blue) and the one with the $1\alpha 1n$ condition (red). No particular differences are evident.

4.2.1 Background subtraction

Having ^{60}Zn a tiny relative cross section, its γ spectrum is, whatever gate is applied, much contaminated. The background subtraction is therefore critical to allow the peaks of interest to emerge from the background.

We have attempted to subtract from the $1\alpha 1n$ spectrum other gated spectra, as the $1\alpha 1p1n$, $1p1n$ or $1p$, in order to enhance the ^{60}Zn . In the $1\alpha 1n$ spectrum the most intense background channels, ^{63}Zn and ^{60}Cu , are both present. The result of the subtraction in the energy region of interest is shown in Figure 4.13. The main peaks of the ground state band of ^{60}Zn are present although the $8^+ \rightarrow 6^+$ 1615-keV and $6^+ \rightarrow 4^+$ 1484-keV transitions, are still partially hidden in the background.

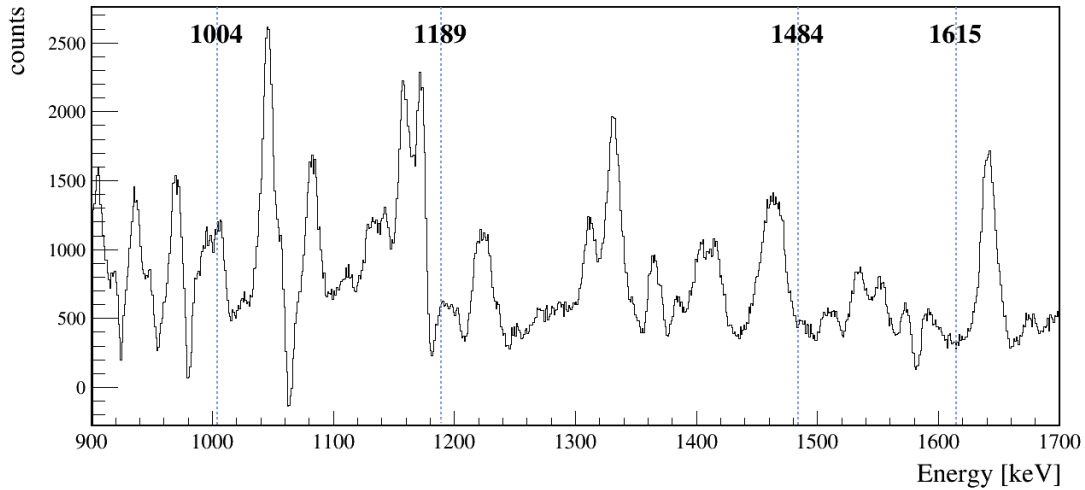


Figure 4.13: The $1\alpha 1n$ gated spectrum obtained by subtracting the $1p1n$ spectrum. The energy range 900÷1700 keV includes the γ -ray energy transitions of the ground state band in ^{60}Zn : 1004 keV, 1189 keV, 1615 keV and 1484 keV.

The results in Figure 4.13 are encouraging, but the statistic of the ^{60}Zn lines is poor and it does not allow any further investigation. Therefore, we tried a different strategy to enhance the peaks of interest by making use of the 1α -gated $\gamma\text{-}\gamma$ matrix. This matrix, in spite of the presence of ^{58}Ni and ^{60}Cu as major contaminants, is very useful for our purpose, the study of ^{60}Zn .

By applying gates, corresponding to the main transitions of the ground state band of ^{60}Zn , we obtained the spectra shown in Figure 4.14. Each gated spectrum has been background subtracted, by taking regions nearby the peaks. In addition, other background subtractions have been applied to some of them, when needed, to remove the dominant contaminant peaks.

By summing the individual spectra (once normalized) of Figure 4.14, the spectrum of Figure 4.15 is obtained. It shows the presence of the ground-state band transitions and accumulation of counts in some points of the higher energy part, above ~ 2 MeV, shown in the inset. These can be weak indications of possible peaks at the following energy: 2018 keV, 2040 keV, 2149 keV, 2453 keV. Two peaks belonging to ^{58}Ni are visible at 1923 keV and 2669 keV.

Some of the above transitions are visible in the spectrum gated on the 1004-keV energy, from the α -gated $\gamma\text{-}\gamma$ matrix, in particular at energies 2018 keV, 2040 keV and 2149 keV, see Figure 4.16. These peaks are not present in the 2α -gated spectrum, corresponding to ^{58}Ni , and are proven not to be in coincidence with the 1004.8-keV $4^+ \rightarrow 2^+$ transition of ^{58}Ni . This has been further check in the existing nuclear data base; the 2149-keV transition can be associated with a 2146-keV transition from the 7^- to the 6^+ state. In any case, the 2α gated spectrum of ^{58}Ni , normalized to the height of the 2_1^+ state, has been subtracted from the spectrum in Figure 4.16.

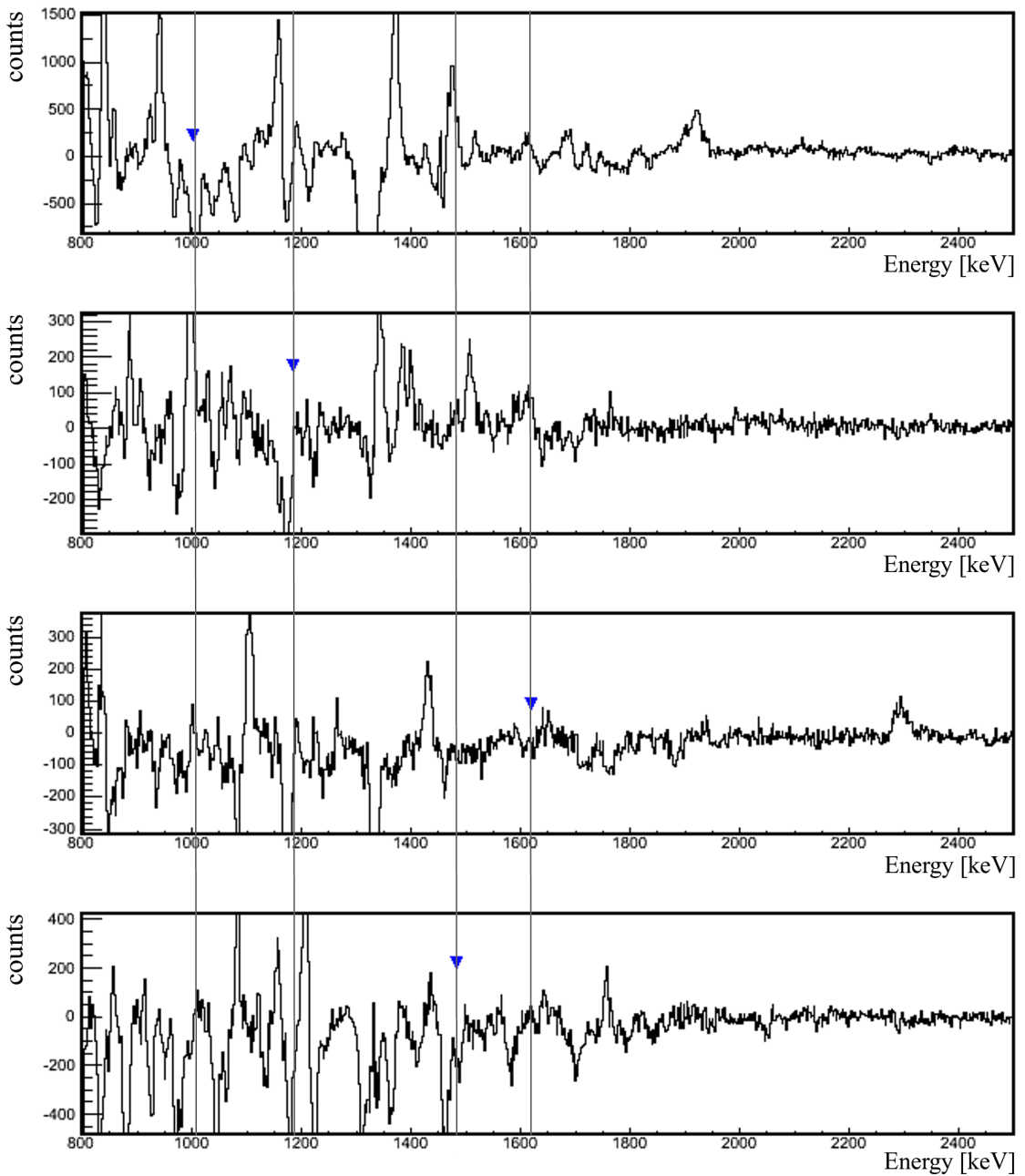


Figure 4.14: Four gates on the 1α -channel $\gamma\gamma$ matrix in the energy ranges corresponding with the four transitions of the ground state band of ^{60}Zn . In each spectrum a blue-triangular marker indicates the specific gate. The spectra have a 2-keV binning.

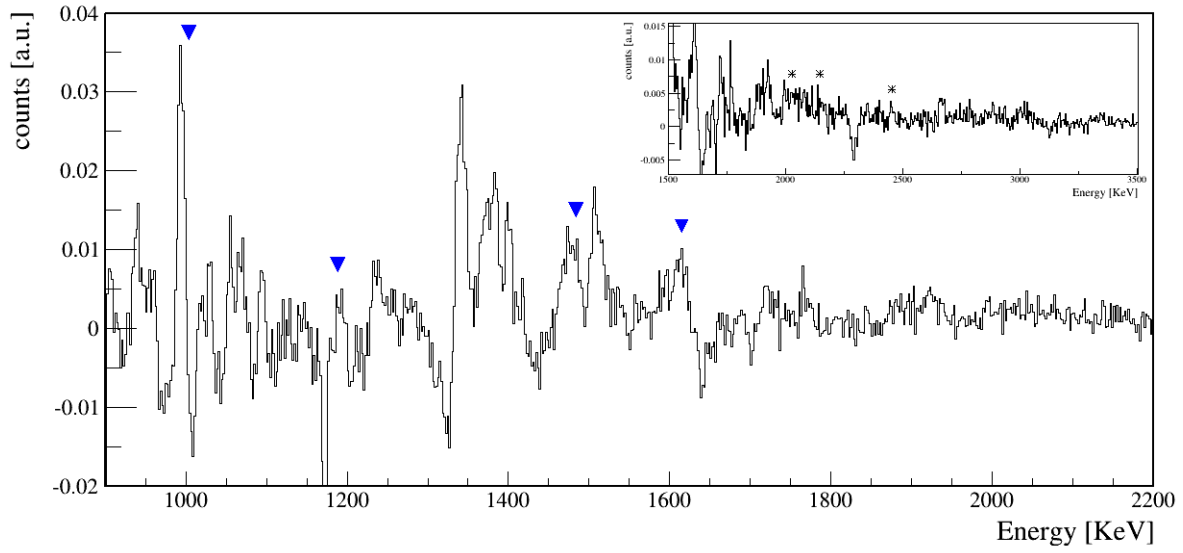


Figure 4.15: γ -ray spectrum showing the sum of the individual gates, corresponding to the low-lying yrast transitions presented in Figure 4.14. The yrast band of ^{60}Zn is enhanced and indications of higher-energy transitions are visible in the inset.

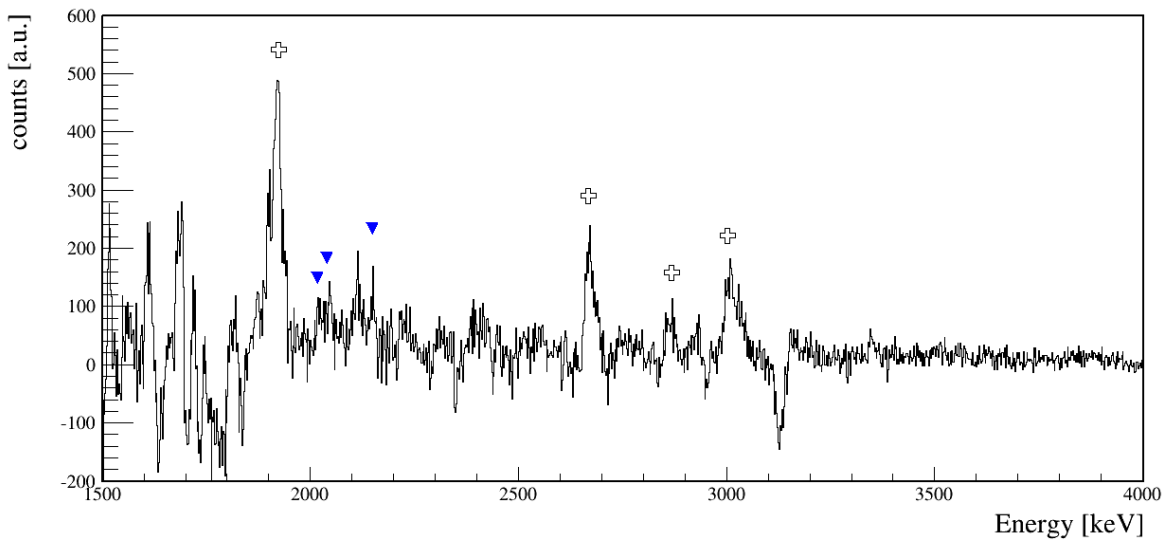


Figure 4.16: γ -ray spectrum in coincidence with the 1004-keV transition, obtained from the α -gated γ - γ matrix. In addition to the dominant ^{58}Ni peaks, marked by a cross, some transitions, marked by a triangle, at energies higher than ~ 2 MeV are visible: 2018 keV, 2040 keV and 2149 keV.

4.3 Neighboring nuclei of interest

4.3.1 The nucleus ^{61}Zn

The most neutron-deficient nucleus in the Zn isotopic chain, that is abundantly populated in this reaction, is ^{61}Zn . In the next Chapter we will see how the knowledge of the level scheme of this nucleus has an impact on the study of ^{60}Zn .

The γ -ray transitions of the ^{61}Zn nucleus, when a gate on the $5/2^- \rightarrow 3/2^-$ 123.8-keV transition of ^{61}Zn is applied, are clearer in the α -gated $\gamma\text{-}\gamma$ matrix with respect of the $1\alpha 1n$ spectrum, that is the corresponding reaction channel. This is because of the much higher statistics of such matrix. The corresponding projection is shown in Figure 4.17.

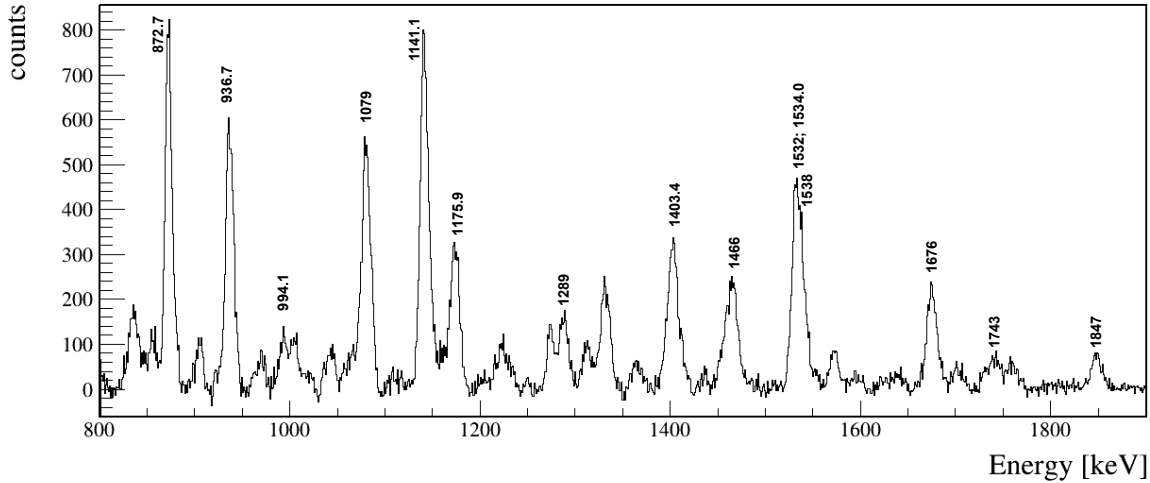


Figure 4.17: Projection of the energy interval [121,126] keV from the 1α -channel $\gamma\text{-}\gamma$ matrix. Levels of ^{61}Zn in coincidence with the transition at 123.8 keV from $5/2^-$ to ground state $3/2^-$ are marked. Any transition, in coincidence with the 123.8 keV transition, is identified below ~ 700 keV.

A total of 14 γ -ray transitions were found up to spin $31/2^-$. A good agreement with the level scheme of ^{61}Zn in Ref. [35, 36] has been obtained. We observe for ^{61}Zn all the main transitions belonging to the normal deformed bands ND1, ND2, ND3 and many of the transitions de-exciting non-yrast levels in the normal deformed band ND6. We report in Figure 4.18 a part of the level scheme of Ref. [36].

4.3.2 The nucleus ^{60}Cu

Another nucleus, that is relevant for comparison with ^{60}Zn , is the mirror nucleus ^{60}Cu , the $T_z = 1$ member of the isobaric multiplet $T = 1$ with mass 60.

From the studies of different spectra gated on 1α -gated $\gamma\text{-}\gamma$ matrix, shown in Figure 4.19, we confirm the transition energies listed in Ref. [37]. The proposed level scheme of ^{60}Cu from Ref. [37] is shown in Figure 4.20.

In the literature, the spin assignment is still tentative. With our dataset we plan to firmly established the spin of the states by using angular distributions, but this goal is beyond the scope of the present work.

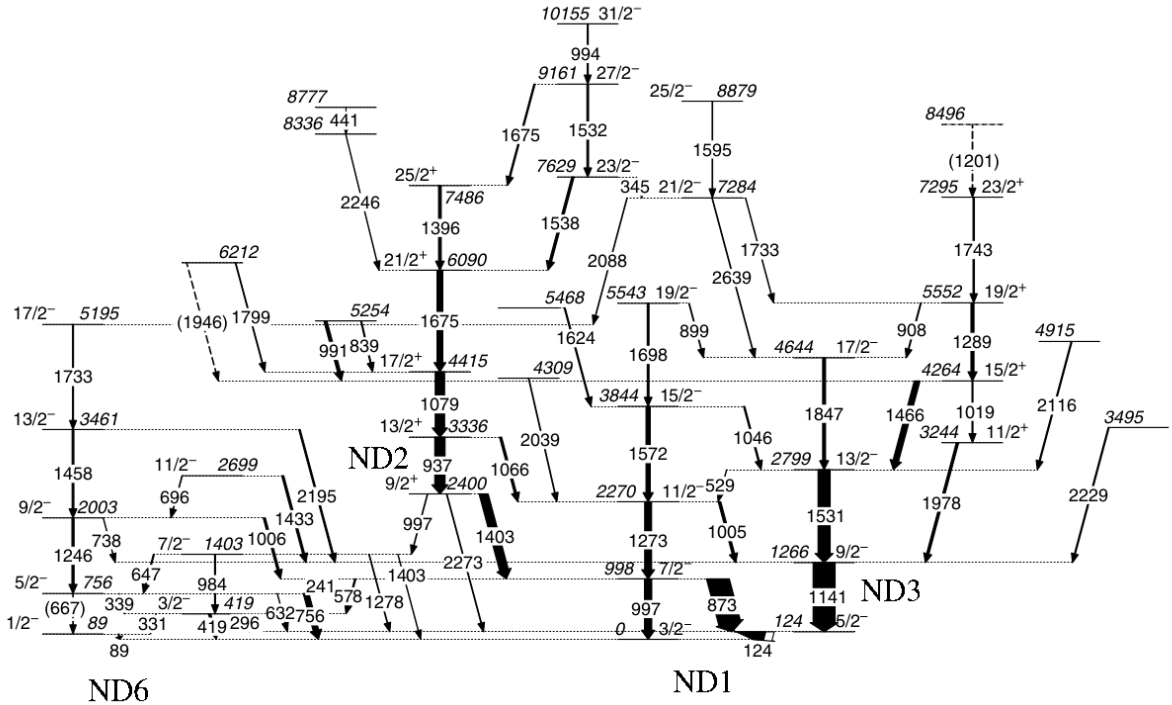


Figure 4.18: Level scheme of ^{61}Zn from Ref. [36]. Energy values are in keV and the widths of arrows corresponds to the relative intensities of the transitions. Tentative transitions and levels are dashed.

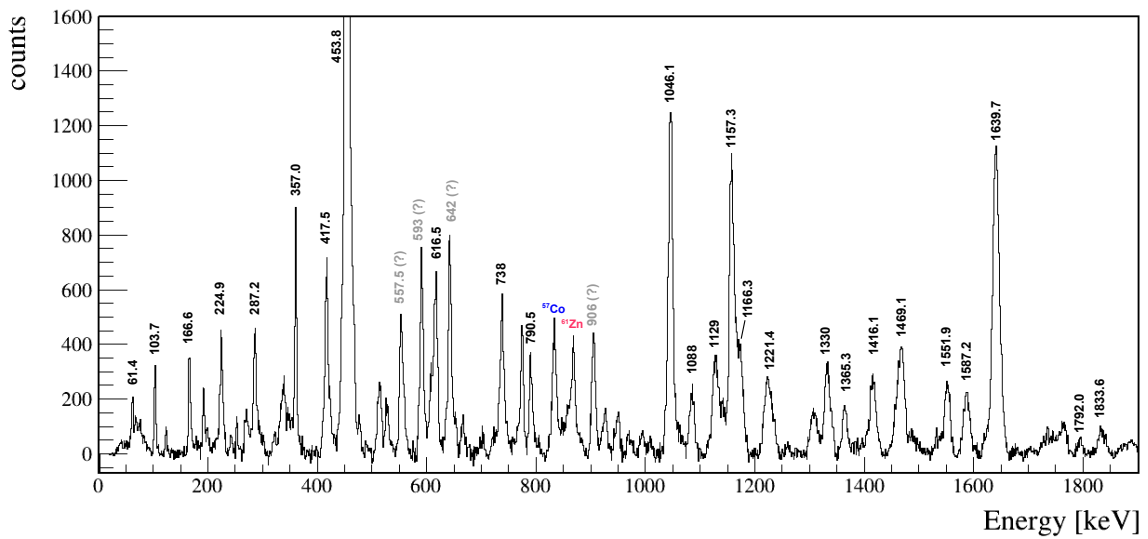


Figure 4.19: Projection of the energy interval [101,106] keV from the γ - γ coincidence matrix, gated on 1α . Several peaks of ^{60}Cu are visible. The 453.8 keV transition, de-excites the 3^+ to the 2^+ ground state, is the most prominent. However, the transitions at 61.4 keV, 224.9 keV, 287.2 keV, 166.6 keV (the last one with an intensity of 1%, with respect to the 453.8 keV transition) are also clearly visible.

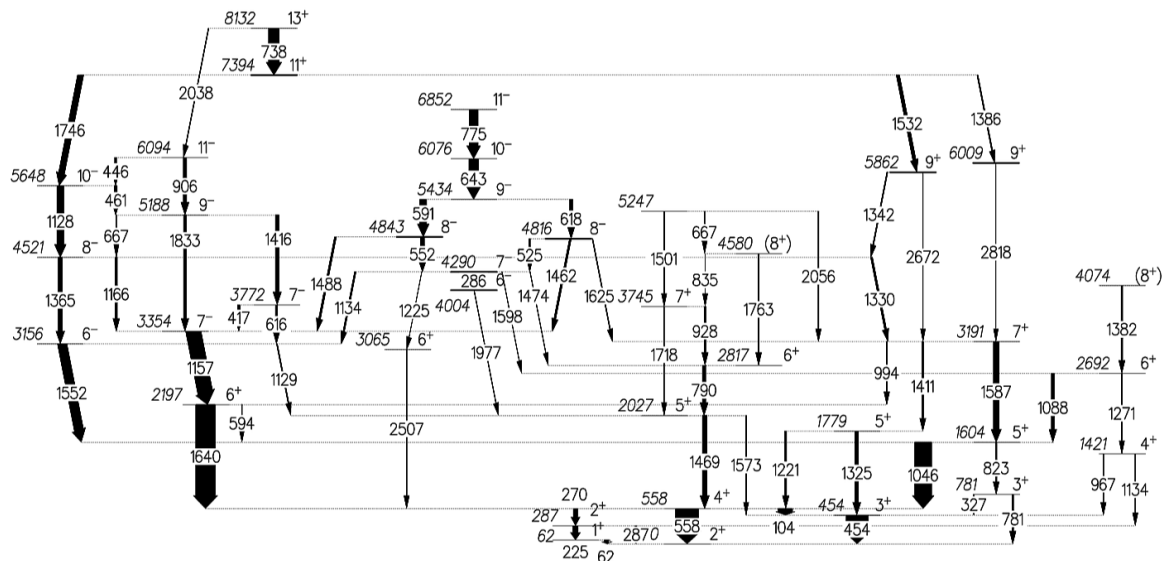


Figure 4.20: The level scheme of ^{60}Cu proposed in [37]. The width of the arrows corresponds to the relative intensities of transitions. Tentative numbers are given in parenthesis.

Chapter 5

Theoretical calculations and interpretation

The experimental results, presented in Chapter 4, are interpreted with the help of theoretical calculations and of the existing experimental results, available in literature.

In this Chapter, large-scale shell-model calculations (LSSM) as well as beyond mean-filed (MF) calculations are presented in order to investigate the structure of ^{60}Zn .

The ^{61}Zn isotope, that has one neutron more in the $p_{3/2}$ orbital, has been also object of shell-model calculations to interpret its possible nature of a neutron weakly coupled to a ^{60}Zn core.

5.1 The nucleus ^{60}Zn

5.1.1 Shell model calculations

As discussed in the shell model paragraph in Chapter 1, the diagonalisation of the hamiltonian matrix provides both the energy, that is a physical observable, and the wave function, which in turn can be used to calculate other observables, i.e. reduced transition probability and (intrinsic) quadrupole moments.

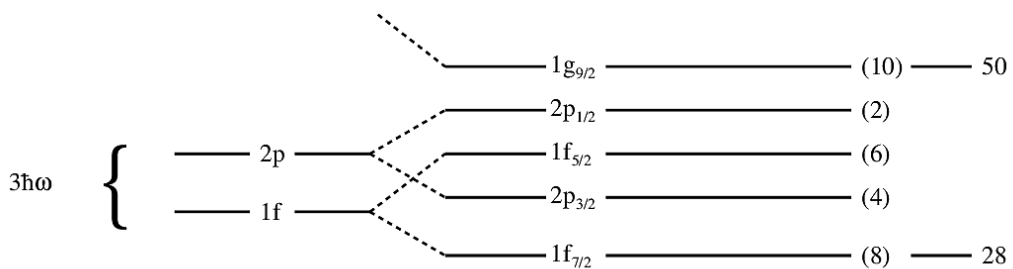


Figure 5.1: Relevant orbitals available for the valence nucleons of the nuclei that are populated in the experiment described in this work.

For the medium-mass nuclei of interest for this work, an inert core has to be assumed and an effective residual interactions normalized to the valence space has to be employed.

The choice of the valence space should reflect a basic physical fact: the most significant components of the low-lying states of nuclei can be accounted for by many-body states involving the excitation of particles in a few orbitals around the Fermi level.

In ^{60}Zn there are 30 protons and 30 neutrons. In the ground state nucleons occupy the inner orbitals, resulting in two protons and two neutrons outside the magic $N=Z=28$ shell closure. When occupying the same orbital, two nucleons of the same kind preferably pair up to spin zero. Thus, the ground state of ^{60}Zn results to have a spin parity of 0^+ . In Figure 5.1 the single particle levels relevant for our calculations are presented.

For the ^{60}Zn and ^{61}Zn nuclei, dedicated calculations have been performed in this work, using either a truncated fp shell or a fpg valence space, the latter with the $f_{7/2}$ blocked and the inclusion of the $g_{9/2}$ orbital, see Figure 5.2.

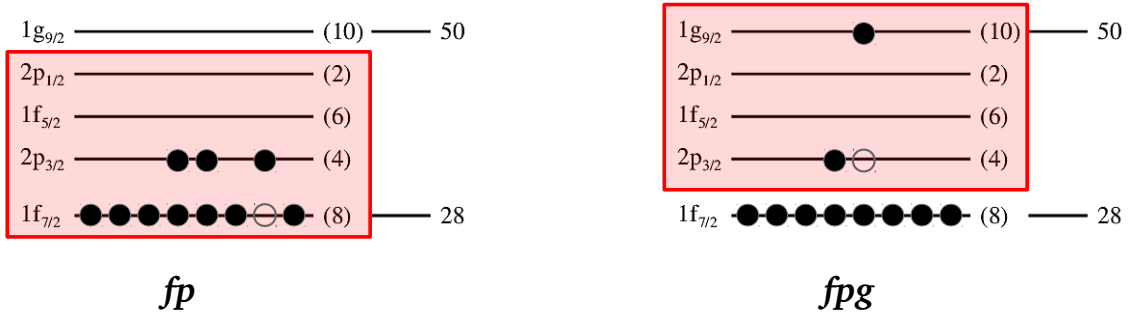


Figure 5.2: Valence space considered in the LSSM calculations for a fp model space (left side) and fpg model space (right side). The nucleons can occupy the $1f_{7/2}$, $2p_{3/2}$, $1f_{5/2}$, $2p_{1/2}$ and $2p_{3/2}$, $1f_{5/2}$, $2p_{1/2}$, $1g_{9/2}$ orbitals, respectively. In the fp model, a nucleon in the $1f_{7/2}$ orbital can jump in a higher level creating a hole in the $1f_{7/2}$. Instead, in the fpg model, all nucleons in $1f_{7/2}$ orbital are fixed but the valence nucleons can occupy the intruder orbital $1g_{9/2}$.

In the first case a ^{40}Ca inert core and the $1f_{7/2}$, $2p_{3/2}$, $1f_{5/2}$, $2p_{1/2}$ valence orbitals are considered. This model space entails the possibility to have cross-shell excitations through the $N=Z=28$ shell gap, that accounts to about 5 MeV [38], and is not a priori excluded, in spite of the relatively low excitation energy for the states of our interest. In fact, some correlation energy could be gained by the system, for example when nucleons occupy the $f_{7/2}$ and $p_{3/2}$ orbitals, being these orbitals quasi SU(3) partners with $\Delta l = \Delta j = 2$. In these case, the GXPF1BR effective interaction [39] has been used for the calculations. A truncation scheme is adopted for the calculation and a max of 10 jumps is permitted for 10 nucleons.

In the second case the $1g_{9/2}$ orbital is included in the valence space. Its high- j nature provides a higher angular momentum as well as larger deformation. It has been seen, in many cases, especially at higher masses or higher spin states, that it could play a significant role already at moderate excitations energies for $N\sim Z$ nuclei. The inert core in this case is ^{56}Ni and jj4b is the effective interaction [40]. No truncation is used for this valence space, with 4 particles.

The predictions of both interactions, for the level energies of the ground-state band of ^{60}Zn , up to the 4^+ state, are in agreement with the experimental observations.

<i>fp</i>		<i>fpg</i>		<i>Exp</i>	
J^π	E [MeV]	J^π	E [MeV]	J^π	E [keV]
0^+	0	0^+	0	0^+	0
2^+	1.05	2^+	1.00	2^+	1003.90 (20)
4^+	1.98	4^+	2.11	4^+	2193.0 (5)
2_2^+	2.67	0_2^+	2.44	(2_2^+)	2559.0 (5)
0_2^+	2.72	2_2^+	3.20	—	—
4_2^+	3.37	6^+	3.8	6^+	3808.4 (7)

Table 5.1: Energy of the levels calculated from LSSM by using the GXPF1BR and jj4b effective interactions. Experimental energies are given in the last column.

The LSSM calculations together with the experimental values are reported in Table 5.1.

For the 6^+ the jj4b interaction is giving better results. The same interaction predicts two bands with similar quadrupole moment, giving a slightly prolate shape, but the theoretical $B(E2)$, linking these two bands, are predicted to be very small. In this model space, the excited 2_2^+ is predicted at 3.2 MeV. However, no firm experimental information is available for the low-lying non-yrast states. The configurations for the 0_1^+ , 2_1^+ and 0_2^+ , 2_2^+ states are reported in Tables 5.2, 5.3, 5.4 and 5.5 respectively. The configuration for the 0_1^+ , 2_1^+ consists in the coupling of the 2π and 2ν to spin 0 and 2, respectively. The relative purity of the wave function is larger in the case of the 0_1^+ , 19%, than for the 2_1^+ , that is much fragmented. For comparison, the occupation numbers for the GXPF1BR are reported in the appendix B.1.1.

0_1^+

Orbital	Configuration	Configuration	Configuration	Configuration
$\pi(2p_{3/2})$	2	0	1	1
$\pi(1f_{5/2})$	0	2	0	1
$\pi(2p_{1/2})$	0	0	1	0
$\pi(1g_{9/2})$	0	0	0	0
$\nu(2p_{3/2})$	2	0	1	1
$\nu(1f_{5/2})$	0	2	0	1
$\nu(2p_{1/2})$	0	0	1	0
$\nu(1g_{9/2})$	0	0	0	0
Percentage	22%	8%	6%	6%

Table 5.2: Composition of the 0_1^+ ground state in ^{60}Zn from the shell-model calculations in the *fpg*-model space. Only the main configurations are shown.

The configuration for the 0_2^+ is very similar to the ground state. The purity of the wave function is also quite similar, amounting to about 20%. The 2_1^+ is extremely fragmented whilst the 2_2^+ accounts for 37% of the wave functions in a 4p-4h excitation from $p_{3/2}$ to $f_{5/2}$.

2_1^+

Orbital	Configuration	Configuration	Configuration	Configuration
$\pi(2p_{3/2})$	2	2	1	0
$\pi(1f_{5/2})$	0	0	0	2
$\pi(2p_{1/2})$	0	0	1	0
$\pi(1g_{9/2})$	0	0	0	0
$\nu(2p_{3/2})$	2	1	2	0
$\nu(1f_{5/2})$	0	0	0	2
$\nu(2p_{1/2})$	0	1	0	0
$\nu(1g_{9/2})$	0	0	0	0
Percentage	9%	8%	8%	5%

Table 5.3: Composition of the 2_1^+ excited state in ^{60}Zn from the shell-model calculations in the fpg -model space. Only the main configurations are shown. The energy predicted for this level is 998 keV.

 0_2^+

Orbital	Configuration	Configuration	Configuration	Configuration
$\pi(2p_{3/2})$	0	2	2	1
$\pi(1f_{5/2})$	2	0	0	0
$\pi(2p_{1/2})$	0	0	0	1
$\pi(1g_{9/2})$	0	0	0	0
$\nu(2p_{3/2})$	0	2	1	2
$\nu(1f_{5/2})$	2	0	0	0
$\nu(2p_{1/2})$	0	0	1	0
$\nu(1g_{9/2})$	0	0	0	0
Percentage	37%	19%	4%	4%

Table 5.4: Composition of the 0_2^+ excited state in ^{60}Zn from the shell-model calculations in the fpg -model space. Only the main configurations are shown. The energy predicted for this level is 2447 keV.

No experimental information about the in- or intra-band transition probabilities exist. LSSM calculations predict a moderate deformation, about $-25 \text{ e}^2\text{fm}^4$ corresponding to a prolate intrinsic shape. In our calculation a similar deformation is expected for the excited 0_2^+ , and increases as a function of the spin.

In Ref [16], by using a pairing plus quadrupole-quadrupole force in a fpg model space, a prolate-to-oblate transition in the $N=Z$ nuclei above ^{56}Ni by moving from ^{60}Zn to ^{68}Se , is predicted. A spectroscopic quadrupole moment of $-24 \text{ e}^2\text{fm}^4$ is expected from calculations. This value is also in a good agreement with the prediction from the EEI scheme, see Ref [41].

2_2^+

Orbital	Configuration	Configuration	Configuration	Configuration
$\pi(2p_{3/2})$	2	0	2	1
$\pi(1f_{5/2})$	0	2	0	0
$\pi(2p_{1/2})$	0	0	0	1
$\pi(1g_{9/2})$	0	0	0	0
$\nu(2p_{3/2})$	2	0	1	2
$\nu(1f_{5/2})$	0	2	0	0
$\nu(2p_{1/2})$	0	0	1	0
$\nu(1g_{9/2})$	0	0	0	0
Percentage	26%	18%	8%	8%

Table 5.5: Composition of the 2_2^+ excited state in ^{60}Zn from the shell-model calculations in the fpg -model space. Only the main configurations are shown. The energy predicted for this level is 3202 keV.

5.1.2 Beyond mean-field calculations: Energy Density Functional results

Energy-density functional (EDF) calculations, by using the DD-PC1 functional [33] do not predict shape coexistence in ^{60}Zn , rather a γ -soft potential, see the potential energy surface (PES) in Figure 5.3, on the left. In the same figure the probability distribution for the wave functions, corresponding to the ground-state and first excited 0_2^+ , are presented. The corresponding level scheme predicted is shown in Fig. 5.4.

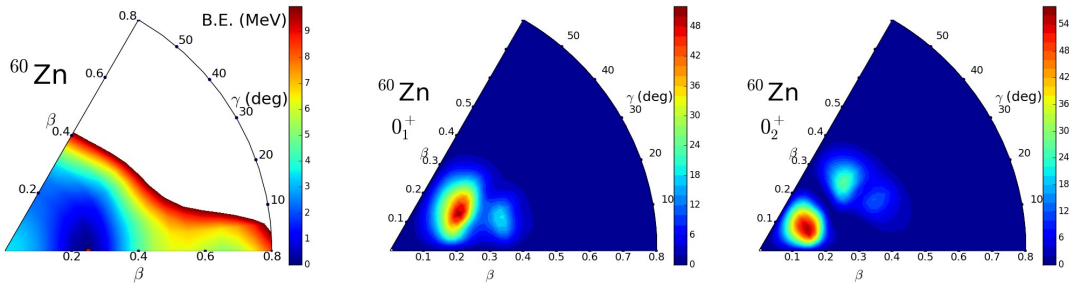


Figure 5.3: In the first panel in the left, the EDF calculations for ^{60}Zn . In the second and the third panel, the wave-function probability for the ground state 0_1^+ and 0_2^+ excited state of ^{60}Zn are given [33].

Similar calculations, but using a different functional, the DP1M, predicts instead an axial rotor behavior, with a prolate shape in the ground state, $-38 \text{ e}^2\text{fm}^4$, and an oblate shape in a side band. The wavefunctions are presented in Figure 5.5. The band structure is visible in the left panel of Fig. 5.6, where, together with the prolate and oblate bands, a triaxial structure based on the prolate band is also predicted. In the right panel of Figure 5.6 the corresponding level scheme is presented.

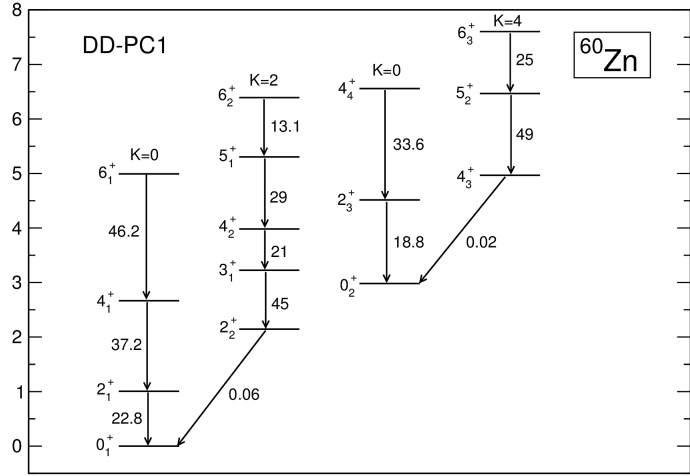


Figure 5.4: Level scheme predicted by EDF calculations in Ref. [33]. The reduced transition probabilities are given in W.u.

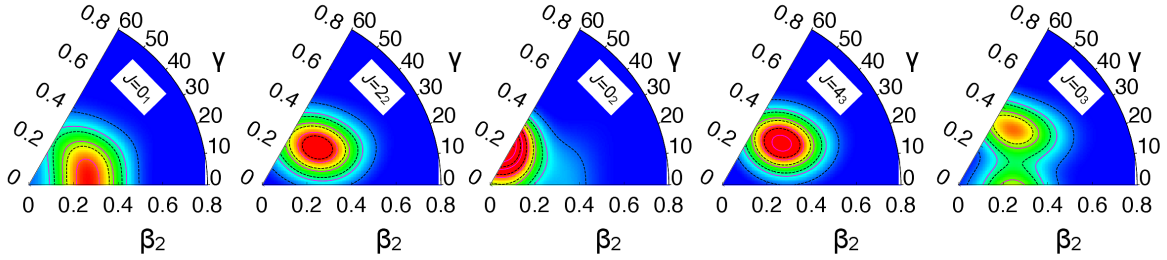


Figure 5.5: Wave-function probability for the ground state 0_1^+ and 0_2^+ excited state of ^{60}Zn predicted by EDF calculations using a PCP1M potential [42]. The reduced transition probabilities are given in W.u.

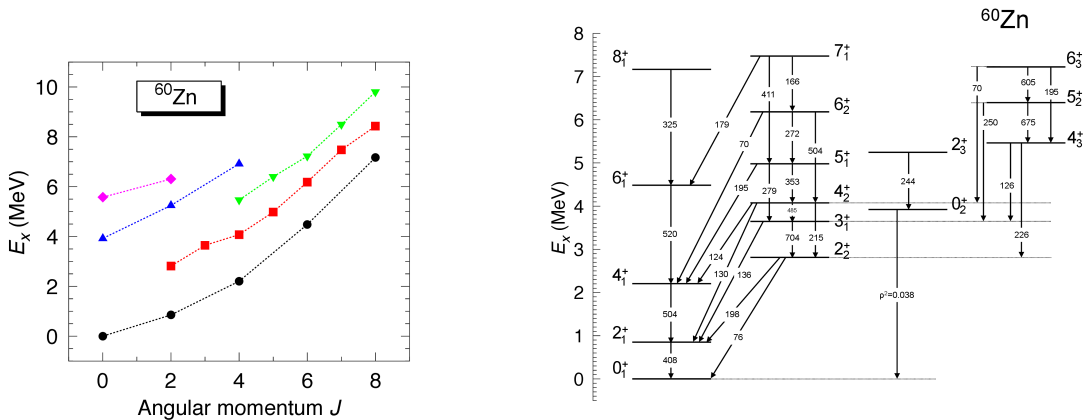


Figure 5.6: Band structure, on the left, and level scheme, on the right, from EDF calculations using a DCP1M potential [42].

5.1.3 Comparison with the present experimental data

In the list of tentative transitions identified in the spectrum of Figure 4.15, at energies higher than 2 MeV, there are peaks compatible with those visible in the 1004-keV gated spectrum, in Figure 4.16, at 2018 keV, 2040 keV and 2149 keV.

LSSM calculations, using the jj4b interaction, predict a 2_2^+ state at an energy of 3.2 MeV, that, by decaying to the 2_1^+ state, involves a transition of 2.145 MeV. This transition is compatible with the one at 2149 keV, although we do not exclude that the other two transitions at 2018 keV and 2040 keV could correspond to such decay. The existence of the 3.2 MeV state implies the presence of a 960-keV transition from the 2_2^+ state to the 4_1^+ state. This can not be experimentally confirmed from our data set.

The EDF calculations predict a 2_2^+ at an energy of either ~ 2 MeV or ~ 3 MeV, considering the DDP1M or the D1S functional, respectively.

The weak experimental evidence for the peak at 2149 keV, that could be interpreted as the transition de-exciting the 2_2^+ to the 2_1^+ , is not in contradiction with our experimental approach, that is a fusion evaporation reaction mainly populating yrast state. In fact, we see in ^{61}Zn low-lying non-yrast states with a much smaller statistics. In a similar -and very asymmetric- reaction $^{58}\text{Ni}(^{12}\text{C},2n)^{68}\text{Sn}$, the side band was populated with a statistics 10 times smaller than the ground-state band.

5.2 ^{61}Zn : particle-core coupled states

In ^{61}Zn there are 30 protons and 31 neutrons. In the ground state two protons and three neutrons are outside the magic $N=Z=28$ shell closure. Thus, the ground state of ^{61}Zn has one unpaired neutron in the $2p_{3/2}$ orbital, and we expect a spin $J^\pi = 3/2^-$ for the state, that is confirmed experimentally.

For ^{61}Zn , consistently with the ^{60}Zn nucleus case, the jj4b effective interaction on the *fpg* valence space and a ^{56}Ni core are used for the shell model calculations.

LSSM calculations predict that the ground state of ^{61}Zn corresponds to a one neutron in the $p_{3/2}$ orbital coupled to the ground-state configuration of ^{60}Zn :

$$3/2_1^- = [0_1^+({}^{60}\text{Zn}) \otimes \nu(p_{3/2})].$$

The occupation numbers are shown in Table 5.6.

We can conclude that the model of a $p_{3/2}$ neutron weakly coupled to a ^{60}Zn core is valid for this state.

However, it is not possible to interpret, in a similar manner, the first excited state $5/2_1^-$ of ^{61}Zn because, from the calculations, it is highly fragmented in terms of the involved configurations. The coupling between 2^+ state of ^{60}Zn and the neutron in $p_{3/2}$, gives in ^{61}Zn a multiplet of states, with spin ranging from $1/2 \div 9/2$, that are not easily comparable to any of the states in ^{60}Zn , especially for the lack of experimental information on the transition probabilities. The occupation number of the excited state $5/2_1^-$ are reported in appendix, in Table B.6.

$3/2_1^-$

Orbital	Configuration	Configuration	Configuration	Configuration
$\pi(2p_{3/2})$	2	1	0	2
$\pi(1f_{5/2})$	0	0	0	0
$\pi(2p_{1/2})$	0	1	2	0
$\pi(1g_{9/2})$	0	0	0	0
$\nu(2p_{3/2})$	3	2	3	1
$\nu(1f_{5/2})$	0	0	0	1
$\nu(2p_{1/2})$	0	1	0	1
$\nu(1g_{9/2})$	0	0	0	0
Percentage	18%	6%	4%	6%

Table 5.6: Composition of the $3/2_1^+$ ground state in ^{61}Zn from the shell-model calculations in the fpg -model space. Only the main configurations are shown.

 $3/2_2^-$

Orbital	Configuration	Configuration	Configuration	Configuration
$\pi(2p_{3/2})$	0	2	1	2
$\pi(1f_{5/2})$	2	0	1	0
$\pi(2p_{1/2})$	0	0	0	0
$\pi(1g_{9/2})$	0	0	0	0
$\nu(2p_{3/2})$	1	1	2	1
$\nu(1f_{5/2})$	2	2	1	1
$\nu(2p_{1/2})$	0	0	0	1
$\nu(1g_{9/2})$	0	0	0	0
Percentage	12%	11%	6%	6%

Table 5.7: Composition of the first $3/2_2^-$ excited state in ^{61}Zn from the shell-model calculations in the fpg -model space. Only the main configurations are shown.

However, other excited states exists, having spin $3/2$, that could be candidates for a particle-core weak coupling between the neutron in the $p_{3/2}$ and the 0_2^+ excited state in ^{60}Zn :

$$3/2_2^- = [0_2^+({}^{60}\text{Zn}) \otimes \nu(p_{3/2})],$$

$$3/2_3^- = [0_2^+({}^{60}\text{Zn}) \otimes \nu(f_{5/2})].$$

The occupation numbers are shown in Tables 5.7 and 5.8.

The energy of the first excited state $3/2_2^-$ of ^{61}Zn is predicted from LSSM calculations at 525 keV and the energy of the second excited state $3/2_3^-$ at 1767 keV. While the first one corresponds to an existing isomers in ^{61}Zn , the latter could correspond to the excited 0^+ in ^{60}Zn , not yet observed. Lifetime or safe Coulomb-excitation measurements would allow to shed some light on the interpretation of these states.

$3/2_3^-$

Orbital	Configuration	Configuration	Configuration	Configuration
$\pi(2p_{3/2})$	0	2	0	0
$\pi(1f_{5/2})$	2	0	2	2
$\pi(2p_{1/2})$	0	0	0	0
$\pi(1g_{9/2})$	0	0	0	0
$\nu(2p_{3/2})$	0	3	0	1
$\nu(1f_{5/2})$	3	0	2	2
$\nu(2p_{1/2})$	0	0	1	0
$\nu(1g_{9/2})$	0	0	0	0
Percentage	15%	12%	6%	5%

Table 5.8: Composition of the second $3/2_3^-$ excited state in ^{61}Zn from the shell-model calculations in the fpg -model space. Only the main configurations are shown.

Chapter 6

Conclusions and Outlook

In this thesis, one of the first experiments with the GALILEO setup at the National Laboratory of Legnaro, is described. The GALILEO setup consists in a Compton-suppressed γ -ray spectrometer combined with a light-charged particles and a neutron detector, EUCLIDES and Neutron Wall, respectively. These ancillary detectors provide the identification of the evaporated particles in a fusion-evaporation reaction, improving the resolving power of the γ array, and allowing to assign the γ -ray energy transitions to a specific nucleus.

The aim of this work was the investigation of the low-lying non-yrast states, namely 0_2^+ and 2_2^+ , of the neutron-deficient $N=Z$ ^{60}Zn . These excited structures was predicted both by the shell-model and beyond mean-field calculations. Some experimental indications pointing at the presence of a side band, with a different configuration with respect to the ground-state band, existed for this nucleus, that belongs to a region of transitional nuclei showing also the shape-coexistence phenomenon.

The reaction chosen to excite non-yrast states in ^{60}Zn is $^{54}\text{Fe}(^{12}\text{C},\alpha 2n)^{60}\text{Zn}$. The kinematics reconstruction of the velocity of the recoiling nucleus, thanks to the presence of the ancillary detectors EUCLIDES and Neutron Wall, produced Doppler-corrected γ -ray spectra with a resolution of 13 keV at 1 MeV. Accurate energy calibration and time alignment procedures were applied, to prepare the data for the subsequent sort in γ - γ coincidence matrices and spectra, for all the channels of interest.

First, we analyzed the 1α , $1p$ and $1n$ channel, in order to identify the nuclei mainly populated in the fusion-evaporation reaction and the major contaminants. Then, we searched for the ^{60}Zn yrast γ -ray transitions. The corresponding $1\alpha 2n$ -channel matrix had a very poor statistic, due to the low cross section in the production of ^{60}Zn and the low efficiency of Neutron Wall in the detection of neutrons with multiplicity two. We thus attempted to study the $1\alpha 1n$ -gated spectrum. This channel had a better statistic and a similar shape of the $1\alpha 2n$ channel because of the frequent misinterpretation of the scattered neutrons.

However, having ^{60}Zn a tiny relative cross section, the corresponding γ spectra are, whatever gate is applied, much contaminated. The background subtraction is therefore critical to allow the peaks, to emerge from the background and the analysis of the 1α -gated γ - γ matrix finally turned out to be the best choice. By applying different gates, the main peaks of the ground-state band of ^{60}Zn were resolved from the background. By summing the individual gates, the presence of the ground state band has been confirmed

and some accumulations of point were visible at high energy although an identification of their exact energy is still challenging due to the low statistics. Finally, some peaks have been marked and in particular one peak at 2149 keV.

Large-scale shell-model calculations with the *fp* and *fpg* model space, corresponding to the GXPFBR and jj4b effective interactions, respectively, have been performed. The jj4b reproduced well the ground state band and predicted a 2_2^+ in ^{60}Zn at an energy compatible with our experimental data. However, energy density functional calculations are not in agreement with the shell model calculations, predicting a 2_2^+ with an energy below the one of the LLSM.

Eventually, because of the low statistics and the discrepant theoretical predictions, no firm conclusion can be drawn about the intrinsic shape of the ^{60}Zn nucleus, at this level.

To improve the quality of the spectra, in the near future we plan to further clean the data by sorting them with a time condition on the multi-particle events. We expect that such condition will allow to better extract the peaks from the huge background.

In addition, to firmly establish the nature of ^{60}Zn , we proposed a safe Coulomb excitation measurement to derive the transition and the intrinsic quadrupole moment, directly related to the intrinsic shape of the nucleus.

Appendices

Appendix A

γ -ray interaction with matter

Nuclei in a fusion-evaporation reaction are typically populated in highly-excited states. After the particle emission, they de-excite to the ground state via a cascade of γ rays which could be detected by a HPGe array in the case of high-resolution γ -ray spectroscopy. The γ -ray energies are then sorted in coincidence matrix and spectra to construct the level scheme of the nucleus and finally investigate its nuclear structure. In our case the γ -ray spectrometer, GALILEO, consists in a Compton-shielded HPGe array.

The detection of any particle or radiation depends on the production of secondary charged particles inside the absorption medium. These secondary charge carriers are collected to produce an electrical signal [43].

For a semiconductor detector, the incoming γ ray loses energy in the material, ionizing the atoms of the detector and giving rise to a number of electron-hole pairs proportional to its energy. When the electron is displaced from the crystal band, a hole appears in its place. Both the electrons and the holes are free to move and drift to the corresponding electrode giving rise to an electrical signal. The number of produced electron-hole pairs is proportional to the energy of the incident γ ray.

The probability of the interaction of a γ ray with the material is expressed by the attenuation coefficient and depends upon the mass of the material atoms. The attenuation coefficient is a measure of the reduction of the γ -ray intensity, at a particular energy, due to an absorber. It is larger for materials with a higher atomic number, hence, for instance, germanium ($Z=32$) is more efficient than silicon ($Z=14$) for the γ ray interaction.

There is not a unique way for the γ rays to interact with the matter. The interactions are: photoelectric absorption, Compton scattering, pair production and Rayleigh scattering. The attenuation coefficient of each effect, in case of germanium material, is shown in Figure A.1.

In the photoelectric absorption a photon transfers all the energy to the electrons of the material. Photoelectric absorption is favored for low-energy γ rays and contributes to the full energy peak in the γ -ray spectrum.

While in the photoelectric absorption the incident photon is completely absorbed in the detector and disappears, in a Compton scattering process the incident γ ray transfers only a portion of its energy to the material electrons and than could escape

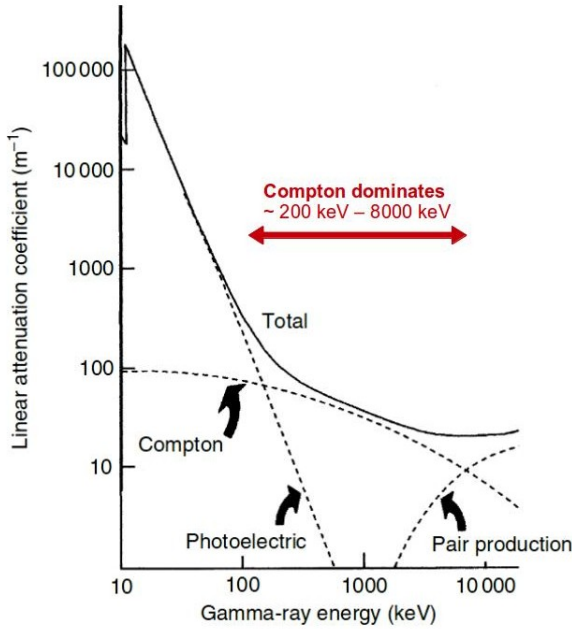


Figure A.1: The linear attenuation coefficient for a γ ray in germanium, as a function of the energy. The relative importance of the three major types of γ -ray interaction is indicated. Photoelectric interactions are dominant at low energy while pair production is more important at higher energy, above the energy threshold. Compton scattering probability is the highest in the mid-energy range between the two other effects. Such range is indeed, the more relevant for high-resolution discrete γ -ray spectroscopy.

the detector. The process is shown in Figure A.2, on the left, and the relation between the energy, before and after the scattering at an angle θ , is:

$$E' = \frac{E}{1 + \frac{E}{m_e c^2} (1 - \cos \theta)}, \quad (\text{A.0.1})$$

where m_e is the electron mass, c the speed of light.

Compton scattering events will produce one or a sequence of recoil electrons carrying only a portion of the energy of the incoming γ -ray. The detector response to Compton interactions exhibits the characteristic Compton continuum extending from zero energy up to the Compton edge, as visible in Figure A.2, on the right. The Compton edge corresponds to the maximum energy transferred, E_t , to the detector. As θ approaches zero, less energy is transferred, while the maximum amount is transferred when θ approaches 180 degrees.

$$E_t(\max) = E \left(1 - \frac{1}{1 + \frac{2E}{m_e c^2}} \right) \quad (\text{A.0.2})$$

In this Appendix, additional LSSM calculations, with respect to those reported in Chapter 5, are presented for the ground states and some excited states of ^{60}Zn and ^{61}Zn .

In case of multiple Compton scattering, the energy appears, in the spectrum, between the Compton edge and the full energy peak (see Figure A.2).

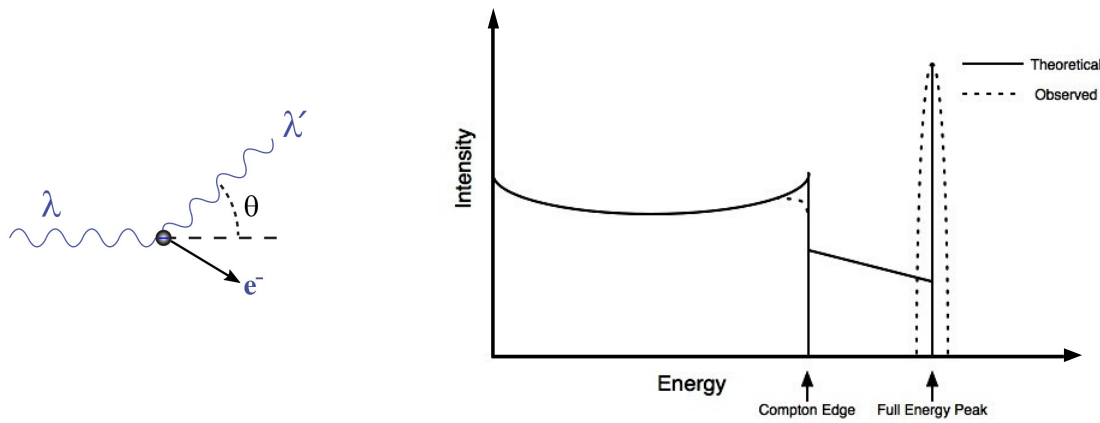


Figure A.2: On the left side, a schematic representation of the Compton scattering process. A photon of wavelength $\lambda = ch/E$ comes from the left, collides with an electron at rest, and then a photon of wavelength $\lambda' = ch/E'$ emerges at an angle θ . The relation between these quantities is given by the expression A.0.1. On the right side, a typical γ -ray spectrum is presented. The full-energy peak corresponds to the absorption of the total energy carried by the photon. When Compton scattering occurs only a part of that energy is released to the detector, starting from a maximum corresponding to the Compton edge. The region between the Compton edge and the full energy peak corresponds to multiple Compton-scattering events.

In the pair-production process, the energy of a photon is converted into an electron-positron pair: $\gamma \rightarrow e^- + e^+$. This process is competitive only at high energy because the photon must exceed the threshold energy, that is the sum of the mass energies for electron and positron, 1.022 MeV.

γ radiations can also interact by the coherent Rayleigh scattering. Rayleigh scattering consists in the absorption and the prompt re-emission of a γ ray with unchanged energy but different direction. Such an interaction can contribute to the attenuation of a γ ray but it does not play a role in the generation of a signal because no energy is transferred to the detector by excitation or ionization.

Appendix B

Shell-model calculation results

In this Appendix, additional LSSM calculations, with respect to those reported in Chapter 5, are presented for the ground states and some excited states of ^{60}Zn and ^{61}Zn .

B.1 ^{60}Zn

B.1.1 fp model space

0_1^+

Orbital	Configuration	Configuration	Configuration	Configuration
$\pi(1f_{7/2})$	8	8	8	8
$\pi(2p_{3/2})$	2	1	2	0
$\pi(1f_{5/2})$	0	1	0	2
$\pi(2p_{1/2})$	0	0	0	0
$\nu(1f_{7/2})$	8	8	8	8
$\nu(2p_{3/2})$	2	1	0	2
$\nu(1f_{5/2})$	0	1	2	0
$\nu(2p_{1/2})$	0	0	0	0
Percentage	25%	4%	4%	4%

Table B.1: Composition of the 0_1^+ ground state in ^{60}Zn from the shell-model calculations in the fp -model space.

2_1^+

Orbital	Configuration	Configuration	Configuration	Configuration
$\pi(1f_{7/2})$	8	8	8	8
$\pi(2p_{3/2})$	2	2	1	2
$\pi(1f_{5/2})$	0	0	0	0
$\pi(2p_{1/2})$	0	0	1	0
$\nu(1f_{7/2})$	8	8	8	8
$\nu(2p_{3/2})$	2	1	2	1
$\nu(1f_{5/2})$	0	0	0	1
$\nu(2p_{1/2})$	0	1	0	0
Percentage	15%	6%	6%	3%

Table B.2: Composition of the 2_1^+ excited state in ^{60}Zn from the shell-model calculations in the fp -model space. The energy predicted for this level is 1048 keV.

 0_2^+

Orbital	Configuration	Configuration	Configuration	Configuration
$\pi(1f_{7/2})$	8	8	8	8
$\pi(2p_{3/2})$	2	0	2	1
$\pi(1f_{5/2})$	0	2	0	0
$\pi(2p_{1/2})$	0	0	0	1
$\nu(1f_{7/2})$	8	8	8	8
$\nu(2p_{3/2})$	2	0	1	2
$\nu(1f_{5/2})$	0	2	0	0
$\nu(2p_{1/2})$	0	0	1	0
Percentage	17%	12%	3%	3%

Table B.3: Composition of the 0_2^+ excited state in ^{60}Zn from the shell-model calculations in the fp -model space. The energy predicted for this level is 2727 keV.

2_2^+

Orbital	Configuration	Configuration	Configuration	Configuration
$\pi(1f_{7/2})$	8	8	7	8
$\pi(2p_{3/2})$	2	2	3	2
$\pi(1f_{5/2})$	0	0	0	0
$\pi(2p_{1/2})$	0	0	0	0
$\nu(1f_{7/2})$	8	7	8	8
$\nu(2p_{3/2})$	2	3	2	1
$\nu(1f_{5/2})$	0	0	0	0
$\nu(2p_{1/2})$	0	0	0	1
Percentage	12%	4%	4%	2%

Table B.4: Composition of the 2_2^+ excited state in ^{60}Zn from the shell-model calculations in the fp -model space. The energy predicted for this level is 2670 keV.

B.2 ^{61}Zn

B.2.1 fp model space

$3/2_1^-$

Orbital	Configuration	Configuration	Configuration	Configuration
$\pi(1f_{7/2})$	8	8	8	8
$\pi(2p_{3/2})$	2	2	1	2
$\pi(1f_{5/2})$	0	0	1	0
$\pi(2p_{1/2})$	0	0	0	0
$\nu(1f_{7/2})$	8	8	8	8
$\nu(2p_{3/2})$	3	1	2	2
$\nu(1f_{5/2})$	0	2	1	0
$\nu(2p_{1/2})$	0	0	1	1
Percentage	27%	4%	4%	3%

Table B.5: Composition of the $3/2_1^+$ ground state in ^{61}Zn from the shell-model calculations in the fp -model space.

B.2.2 fpg model space

$5/2_1^-$

Orbital	Configuration	Configuration	Configuration	Configuration
$\pi(2p_{3/2})$	2	1	0	1
$\pi(1f_{5/2})$	0	0	2	0
$\pi(2p_{1/2})$	0	1	0	1
$\pi(1g_{9/2})$	0	0	0	0
$\nu(2p_{3/2})$	2	2	2	1
$\nu(1f_{5/2})$	1	1	1	1
$\nu(2p_{1/2})$	0	0	0	1
$\nu(1g_{9/2})$	0	0	0	0
Percentage	23%	7%	7%	7%

Table B.6: Composition of the $5/2_1^+$ excited state in ^{61}Zn from the shell-model calculations in the fpg -model space.

Bibliography

- [1] The limits of the nuclear landscape.
J. Erler, N. Birge, M. Kortelainen, W. Nazarewicz, E. Olsen, A. Perhac, and M. Stoitsov.
Nature **486**, 509 (2012)
- [2] Shape coexistence in atomic nuclei.
K. Heyde and J. Wood.
Reviews in Modern Physics **83**, 1467 (2011)
- [3] Nuclei “at the top of their shape”.
L. Fortunato.
Europhysics News **40**, 25 (2009)
- [4] Solutions of the Bohr Hamiltonian, a compendium.
L. Fortunato.
Eur. Phys. J. A **26**, 1 (2005)
- [5] Self-consistent tilted-axis-cranking study of triaxial strongly deformed bands in ^{158}Er at ultrahigh spin.
Y. Shi, J. Dobaczewski, S. Frauendorf, W. Nazarewicz, J. Pei, F. Xu, and N. Nikolov.
<http://www.fuw.edu.pl/dobaczew/tilt-triax-17w/tilt-triax-17w.html> (2012)
- [6] Review of mean-field theory.
D. Lacroix.
International Joliot Curie School (2011)
- [7] Hartree-Fock Calculations with Skyrme’s Interaction. I. Spherical Nuclei.
D. Vautherin and D. Brink.
Phys. Rev. C **5**, 626 (1972)
- [8] Hartree-Fock-Bogolyubov calculations with the *D1* effective interaction on spherical nuclei.
J. Dechargé and D. Gogny.
Phys. Rev. C **21**, 1568 (1980)

- [9] Shape coexistence in neutron-rich Sr isotopes: Coulomb excitation of ^{96}Sr .
E. Clément and A. Gorgen.
INTC-P-216 CERN-INTC (2006)
- [10] Shape evolution in even-even $N \leq 126$, $Z \geq 82$ nuclei.
P. Rahkila.
University of Jyväskylä, Department of Physics Research Report **4**, 111 (2010)
- [11] Observation of a Discrete-Line Superdeformed Band up to $60\hbar$ in ^{152}Dy .
P. J. Twin, B. M. Nyakó, A. H. Nelson, J. Simpson, M. A. Bentley, H. W. Cranmer-Gordon, P. D. Forsyth, D. Howe, A. R. Mokhtar, J. D. Morrison, et al.
Phys. Rev. Lett. **57**, 811 (1986)
- [12] Microscopic study of the high-spin behavior in selected $A \simeq 80$ nuclei.
W. Nazarewicz, J. Dudek, R. Bengtsson, T. Bengtsson, and I. Ragnarsson.
Nucl. Phys. A **435**, 397 (1985)
- [13] Evidence for Collective Oblate Rotation in $N=Z$ ^{68}Se .
S. Fisher, D. Balamuth, P. Hauslanden, C. Lister, M. Carpenter, D. Seweryniak, and J. Schwartz.
Physical Review Letters **84**, 4064 (2000)
- [14] ($^3\text{He},n$) Reaction at 25 Mev.
M. Greenfield, C. Bingham, E. Newman, and M. Saltmarsh.
Physical Review C **6**, 1756 (1972)
- [15] γ -ray transitions in ^{48}Cr and ^{60}Zn .
R. Kamermans, H. Joagsma, J. van der Spek, and U. H.
Physical Review C **10**, 620 (1974)
- [16] Shape transition and oblate-prolate coexistence in $N=Z$ fpg -shell nuclei.
K. Kaneko, M. Hasegawa, and T. Mizusaki.
Physical Review C **70**, 051301 (2004)
- [17] K. S. Krane. *Introductory Nuclear Physics*. John Wiley & Sons (1988)
- [18] GAMMASPHEARE Online Booklet Homepage
<http://nucalf.physics.fsu.edu/riley/gamma/>
- [19] INFN, Laboratori Nazionali di Legnaro, Tandem XTU
<http://www.lnl.infn.it/index.php/en/accelerators-3/tandem-xtu>
- [20] The 16 MV tandem of the Laboratori Nazionali di Legnaro.
C. Signorini.
Revue de Physique Appliquee **12**, 1361 (1977)

- [21] From Ge(Li) detectors to γ -ray tracking arrays - 50 years of gamma spectroscopy with germanium detectors.
 J. Eberth and J. Simpson.
 Progress in Particle and Nuclear Physics **60**, 283 (2008)
- [22] Status of the Gamma-Ray spectrometer GALILEO.
 J. Valiente-Dobón, D. Mengoni, F. Recchia, G. de Angelis, D. Barrientos, D. Bazzacco, M. Bellato, A. Benato, M. Bettini, L. Berti, et al.
 INFN-LNL Ann. Report (2015)
- [23] The first physical campaign of the EUCLIDES Si-ball detector coupled to GALILEO γ -ray spectrometer.
 D. Testov, D. Mengoni, C. Boiano, P. Cocconi, P. John, R. Isocrate, G. de Angelis, D. Bazzacco, A. Boso, F. Calaon, et al.
 INFN-LNL Ann. Report (2015)
- [24] High efficient 4π light charged particle segmented detector Euclides for in-beam gamma spectroscopy at Galileo array.
 D. Testov, D. Mengoni, P. John, G. de Angelis, D. Bazzacco, D. Boiano, A. Boso, F. Calaon, A. Gadea, A. Goasduff, et al.
 INFN-LNL Ann. Report (2017)
- [25] Neutron Wall.
 Johan Nyberg, Gammapool Workshop, Paris (2008).
<http://nsg.physics.uu.se/nwall/>
- [26] The Genesis of NEDA (NEutron Detector Array): Characterizing its Prototypes.
 A. Pipidis, A. Di Nitto, G. Jaworski, T. Hüyük, J. Agramunt, G. de Angelis, M. Erduran, M. Ertürk, A. Gadea, G. La Rana, et al.
 INFN-LNL Ann. Report (2011)
- [27] The EUROBALL Neutron Wall - design and performance tests of neutron detectors.
 O. Skeppstedt, H. Roth, L. Lindström, R. Wadsworth, I. Hibbert, N. Kelsall, D. Jenkins, H. Grawe, M. Górska, M. Moszyński, et al.
 Nuclear Instruments and Methods in Physics Research Section A **421**, 531 (1999)
- [28] Doppler Correction Performance via Complete Kinematic Reconstruction for GALILEO Coupled to EUCLIDES and Neutron Wall.
 P. John, G. Goasduff, A. ang Jaworski, and D. Mengoni.
 INFN-LNL Ann. Report (2016)
- [29] Nuclear Structure Uppsala, Brief Description of the Neutron Wall
<https://nsg.physics.uu.se/nwall/description>

- [30] EUCLIDES: a Highly Efficient 4π Light Charged Particle Segmented Detector for in-beam γ Spectroscopy.
E. Farnea, LNL. (2006)
- [31] Coulomb Energy Differences in $T = 1$ Mirror Rotational Bands in ^{50}Fe and ^{50}Cr .
S. M. Lenzi, N. Mărginean, D. R. Napoli, C. A. Ur, A. P. Zuker, G. de Angelis, A. Algora, M. Axiotis, D. Bazzacco, N. Belcari, et al.
Phys. Rev. Lett. **87**, 122501 (2001)
- [32] B. Blank. Private communication.
- [33] D. Vretenar. Private communication.
- [34] Decay Out of the Doubly Magic Superdeformed Band in the $N = Z$ Nucleus ^{60}Zn .
C. E. Svensson, D. Rudolph, C. Baktash, M. A. Bentley, J. A. Cameron, M. P. Carpenter, M. Devlin, J. Eberth, S. Flibotte, A. Galindo-Uribarri, et al.
Phys. Rev. Lett. **82**, 3400 (1999)
- [35] Comprehensive γ -ray spectroscopy of rotational bands in the $N = Z + 1$ nucleus ^{61}Zn .
L.-L. Andersson, I. Ragnarsson, D. Rudolph, E. K. Johansson, D. A. Torres, C. Andreoiu, M. P. Carpenter, R. J. Charity, C. J. Chiara, J. Ekman, et al.
Phys. Rev. C **79**, 024312 (2009)
- [36] γ -ray spectroscopy of excited states in $^{61}_{30}Zn_{31}$.
L.-L. Andersson, D. Rudolph, J. Ekman, C. Fahlander, E. K. Johansson, R. du Rietz, C. J. Gross, P. A. Hausladen, D. C. Radford, and G. Hammond.
Eur. Phys. J. A **30**, 381 (2006)
- [37] Survey of $E1$ transitions in the mass $A \sim 60$ region.
O. Izotova, D. Rudolph, J. Ekman, C. Fahlander, A. Algora, C. Andreoiu, R. Cardona, C. Chandler, G. de Angelis, E. Farnea, et al.
Phys. Rev. C **69**, 037303 (2004)
- [38] Nuclear magic numbers: New features far from stability.
O. Sorlin and M.-G. Porquet.
Progress in Particle and Nuclear Physics **61**, 602 (2008)
- [39] Evidence for a new nuclear 'magic number' from the level structure of ^{54}Ca .
D. Steppenbeck, S. Takeuchi, N. Aoi, P. Doornenbal, M. Matsushita, H. Wang, H. Baba, N. Fukuda, S. Go, M. Honma, et al.
Nature **502**, 12522 (2013)
- [40] B. A. Brown (Unpublished).

- [41] Nilsson-SU3 self-consistency in heavy $N = Z$ nuclei.
A. P. Zuker, A. Poves, F. Nowacki, and S. M. Lenzi.
Phys. Rev. C **92**, 024320 (2015)
- [42] T.Rodriguez. Private communication.
- [43] G. R. Gilmore. *Practical γ -ray Spectrometry*. John Wiley and Son (2008)